Detection, Identification and localization of road defects using LiDAR data : application to road network state evaluation

Mohammad Ali Zaiter

To cite this version:

Mohammad Ali Zaiter. Detection, Identification and localization of road defects using LiDAR data : application to road network state evaluation. Signal and Image processing. Université du Littoral Côte d'Opale, 2021. English. NNT : 2021DUNK0629 . tel-03971233

HAL Id: tel-03971233
https://theses.hal.science/tel-03971233v1

Submitted on 3 Feb 2023

ulco
Université
Littoral Côte d'Opale

Thèse de Doctorat

Mention Sciences pour l'Ingénieur
Spécialité Génie Informatique, Automatique et Traitement du Signal

présentée à *l'École Doctorale en Sciences Technologie et Santé (ED 585)*

de l'Université du Littoral Côte d'Opale

par

Mohammad Ali ZAITER

pour obtenir le grade de Docteur de l'Université du Littoral Côte d'Opale

Détection, Identification et Localisation des Défauts Routiers à l'Aide de Données LiDAR : Application à l'Évaluation de l'État du Réseau Routier

Soutenue le 19 Mars 2021, après avis des rapporteurs, devant le jury d'examen :

M. Yassine RUICHEK, Professeur, Université de Technologie de Belfort-Montbéliard	**Présidente**
M. Denis POMORSKI, Professeur, Université de Lille	**Rapporteur**
M^{me}. Véronique CHERFAOUI, Professeur, Université de Technologie de Compiègne	**Rapporteur**
M^{me}. Farah CHEHADE, Enseignant Chercheur, Université de Technologie de Troyes	**Examinateur**
M. Jean-Charles NOYER, Professeur, Université du Littoral Côte d'Opale	**Directeur de Thèse**
M. Ghaleb FAOUR, Chargé de Recherche HDR, CNRS Liban	**Directeur de Thèse**
M. Régis LHERBIER, Maître de Conférences, Université du Littoral Côte d'Opale	**Encadrant de Thèse**
M. Oussama BAZZI, Professeur, Université Libanaise	**Encadrant de Thèse**

LISIC
Laboratoire d'Informatique Signal & Image de la Côte d'Opale

CNRS
National Council for Scientific Research

PhD Thesis

Major : Information and Communication Sciences and Technologies
Specialty : Signal and Image Processing

presented to *Doctoral School in Science, Technology and Health (ED 585)*

Université du Littoral Côte d'Opale

by

Mohammad Ali ZAITER

to obtain the Doctor of Philosophy degree from Université du Littoral Côte d'Opale

Detection, Identification and Localization of Road Defects using LiDAR Data : Application to Road Network State Evaluation

Defended on March 19, 2021, after approval of reviewers, in front of examining board :

Mr. Yassine RUICHEK, Professor, Université de Technologie de Belfort-Montbéliard	**President**
Mr. Denis POMORSKI, Professor, Université de Lille	**Reviewer**
Mrs. Véronique CHERFAOUI, Professor, Université de Technologie de Compiègne	**Reviewer**
Mrs. Farah CHEHADE, Associate Professor, Université de Technologie de Troyes	**Examiner**
Mr. Jean-Charles NOYER, Professor, Université du Littoral Côte d'Opale	**Thesis Director**
Mr. Ghaleb FAOUR, Higher Degree Research HDR, CNRS Lebanon	**Thesis Director**
Mr. Régis LHERBIER, Associate Professor, Université du Littoral Côte d'Opale	**Thesis Co-Director**
Mr. Oussama BAZZI, Professor, Lebanese University	**Thesis Co-Director**

Declaration of Authorship

I, Mohammad Ali ZAITER, declare that this thesis titled, "Detection, Identification and Localization of Road Defects using LiDAR Data: Application to Road Network State Evaluation" and the work presented in it are my own. I confirm that:

- This work was done wholly or mainly while in candidature for a research degree at this University.
- Where any part of this thesis has previously been submitted for a degree or any other qualification at this University or any other institution, this has been clearly stated.
- Where I have consulted the published work of others, this is always clearly attributed.
- Where I have quoted from the work of others, the source is always given. With the exception of such quotations, this thesis is entirely my own work.
- I have acknowledged all main sources of help.
- Where the thesis is based on work done by myself jointly with others, I have made clear exactly what was done by others and what I have contributed myself.

Signed:

Date:

“Thanks to my solid academic training, today I can write hundreds of words on virtually any topic without possessing a shred of information, which is how I got a good job in journalism.”

Dave Barry

Acknowledgements

First and foremost, praises and thanks to the God, the almighty, for his showers of blessings throughout my travel and research journey.

Special thanks to the Université du Littoral Côte d'Opale ULCO and the National Council For Scientific Research in Lebanon CNRS-L for supporting this work with a grant scholarship. I am also very thankful to the Laboratoire d'Informatique Signal et Image de la Côte d'Opale LISIC and CNRS-L Remote Sensing Center for providing me the opportunity to carry out my PhD research in good conditions.

I would like to express my deep and sincere gratitude to my thesis directors, Prof. Jean-Charles NOYER and Dr. Ghaleb FAOUR for giving me the opportunity to do research and providing invaluable guidance throughout this research. I would also like to thank my thesis co-directors, Dr. Régis LHERBIER and Prof. Oussama BAZZI, for their valuable advices during my thesis work. It was a great privilege and honor to work under their guidance, and I am also extremely thankful for their efforts and advices.

I would also like to express my special thanks to Prof. Denis POMORSKI and Prof. Véronique CHERFAOUI for their precious time and effort to review my work. Special thanks to Prof. Yassine RUICHEK, Dr. Farah CHEHADE as well for examining my thesis.

Thanks to the entire administrative department, especially Mrs. Gaelle Compiegne, for always helping me with administrative procedures at the lab.

Thanks to Prof. Serge REBOUL and Dr. Georges STIENNE for their kindly gesture and advices.

To my friends and research colleagues, Hussien Mostafa, Dr. Hadi DIB, Dr. Abdallah Dib, Hussien KANSO, Dr. Ghida BADRAN, Dr. Layal FAYAD, Dr. Mohammad KASSEM, Dr. Samah HIJAZI, Dr. Hiba AL ASSAAD, Pamela AL ALAM, Dr. Ahmad DARWICHE, Rawaa AWADA, Hassan MAZYAD, Hamza ISSA, Hassan YASSINE, Yahya ABBASS, Mohammd ATWI, Ibrahim CHERRI, Marc NASSAR, Dr. Ali MANSOUR, Rasha SHAMSEDDINE, Yussef FAOUR and Mirna CHARIF, thank you all for your constant support.

To my parents and life coaches, Issa ZAITER and Ogareet HAJ HASSAN, no words can express my feelings of gratitude. Thank you for being there every moment, showering me with love, support, encouragement, sincere prayers, and care. I am extremely grateful for all the sacrifices you have done for making my future brighter. To my sister Batoul ZAITER and my brother Abbass ZAITER, simply thank you for being you. I am extremely lucky to be your brother.

Final words to my idol and supporter Mr. Mohammad Mahdi HASHEM. Thank you for your patience and for listening to me every single day, to my smallest and simplest problems, to my fears and worries. Thank you for understanding the long silent nights. I owe it all to you . . .

Résumé

Dans les applications liées au transport, la problématique de détection des défauts de la route est non seulement importante pour construire un système efficace d'aide à la conduite mais également contribuer à la maintenance des infrastructures routières dans une logique d'amélioration globale de la sécurité des routes. Cette thèse s'inscrit dans ce cadre, avec comme particularité d'être axée sur un télémètre laser à balayage 3D (LIDAR) permettant de percevoir l'environnement du véhicule et délivrant des mesures de cibles étendues. Afin d'être efficace en termes de précision en localisation et d'identification du défaut, le processus de détection/estimation nécessite une résolution élevée sur la cible, ce qui impose que le LiDAR soit positionné relativement proche de la route avec une orientation choisie afin d'augmenter cette résolution. Cependant, avant toute détection, ce contexte opérationnel conduit à envisager des méthodes d'estimation des paramètres extrinsèques du capteur tenant compte de cette spécificité opérationnelle.

La première partie de cette thèse porte donc sur une nouvelle méthode de calibration extrinsèque d'un capteur LiDAR 3D, appelée « LiDAR/Ground Calibration Method » qui se concentre sur l'estimation du plan de la route. Cette méthode est également efficace dans la configuration expérimentale particulière d'un angle élevé d'inclinaison du LiDAR. Dans cette configuration, la calibration du capteur LiDAR est un problème clé en particulier pour garantir l'efficacité de la détection des objets de taille modeste au sol. La méthode de calibration extrinsèque proposée peut être résumée en différentes étapes : ajustement du modèle géométrique de surface de la route, estimation des paramètres extrinsèques (orientation 3D, altitude) et optimisation des paramètres extrinsèques. Les résultats sur données synthétiques et réelles sont présentés en termes de précision et de robustesse par rapport à la variation de hauteur et à la précision sur l'orientation et la distance, montrant ainsi la stabilité et la pertinence de la méthode de calibration extrinsèque proposée.

La deuxième partie propose deux nouvelles méthodes de détection de défauts routiers, dénommées Feature-Based Defect Detection Method (FBDDM) et Grid-Based Defect Detection Method (GBDDM). La méthode de détection FBDDM, basée sur les propriétés de concavité fournies par un filtre gaussien différentiel du second ordre, permet de détecter plusieurs défauts de route homogènes à chaque élévation laser. Quant à elle, la méthode de détection GBDDM est basée sur deux étapes principales : une étape d'interpolation construite sur une pondération des impacts lidar dépendant de la distance et un découpage de la surface en quadrillage dynamique qui permet de détecter, visualiser et localiser des défauts routiers multiples. Les résultats d'évaluation montrent une très bonne performance de ces méthodes de détection de défauts, en termes d'exactitude et de précision par rapport à d'autres méthodes de détection existantes. Elles montrent également leur efficacité dans la capacité de détection des défauts de type nids-de-poule ou de déformation de chaussée (bosses) en contexte expérimental maîtrisé.

Mots-clés: LiDAR Mobile 3D, Étalonnage Extrinsèque LiDAR, Systèmes de Transport Intelligents, Détection et Localisation des Défauts Routiers, Identification et Visualisation des Défauts Routiers.

Abstract

In transportation applications, the problem of detection of road defects is not only important to build an efficient Advanced Driver-Assistance System, but also to contribute to the maintenance of road infrastructures with the aim of an overall improvement in road safety. This issue is being taken into consideration in this thesis, but the presented works primarily focus on the use of a 3D scanning laser rangefinder (LiDAR) allowing to observe the vehicle's environment and delivering measurements of extended targets. In order to be efficient in terms of localization accuracy and defect identification, the detection/estimation process involves a high resolution on the target, which requires that the LiDAR sensor to be positioned relatively close to the road with a selected orientation in order to increase the coverage resolution. However, before any detection, this operational context leads to consideration of methods for estimating extrinsic parameters of the sensor taking into account of this operational specificity.

The first part of this thesis involves a new method of extrinsic calibration for 3D LiDAR sensor, called LiDAR/Ground Calibration Method, which focuses on the geometrical ground plane-based estimation. This method is also efficient in the challenging experimental configuration of a high tilt angle of the LiDAR sensor. In this configuration, the calibration of the LiDAR sensor is a key problem particularly to ensure the efficiency of the detection of objects with small size on the ground. The proposed extrinsic calibration method can be summarized by the following procedure: fitting geometric road surface model, extrinsic parameters estimation (3D orientation, altitude) and extrinsic parameters optimization. The results are presented on synthetic and real data in terms of precision and robustness against variations of height and accuracy on orientation and distance, showing the stability and relevance of the proposed extrinsic calibration method.

The second part proposes two novel road defect detection methods, called Feature-Based Defect Detection Method (FBDDM) and Grid-Based Defect Detection Method (GBDDM). The FBDDM detection method, based on concavity properties provided by a second-order differential Gaussian filter, allows the detection and identification of several homogeneous road defects at each laser elevation. However, the GBDDM detection method is based on two main steps: a weighted interpolation step built on inverse distance of the LiDAR impacts and a surface splitting in terms of dynamic grid which makes it possible to detect, visualize and localize multiple road defects. The evaluation results show a very good performance of these defect detection methods, in terms of accuracy and precision against existing detection methods. They also prove their effectiveness in detecting pothole defect or pavement deformation (hump) in a controlled experimental context.

Keywords: 3D Mobile LiDAR, LiDAR Extrinsic Calibration, Intelligent Transportation Systems, Road Defect Detection and Localization, Road Defect Identification and Visualization.

Contents

List of Figures

List of Tables

List of Abbreviations

ULCO	Université du Littoral Côte d'Opale
CNRS-L	National Council of Scientific Research in Lebanon
LISIC	Laboratoire d'Informatique Signal et Image de la Côte d'Opale
WHO	World Health Organization
UN	United Nations
LRF	Laser Range Finder
LiDAR	Light Detection and Ranging
ADAS	Advanced Driver Assistance Systems
DOF	Degree of Freedom
RADAR	Radio Detection and Ranging
SLAM	Simultaneous Localization and Mapping
DARPA	Defense Advanced Research Projects Agency
FOV	Field of View
SNR	Signal to Noise Ratio
HDL-64E	High Definition LiDAR 64 Emitters
VLP-16	Velodyne LiDAR Puck 16
RANSAC	Random Sample Consensus
IMU	Inertial Measurement Unit
GPS	Global Positioning System
SVM	Support Vector Machine
LRMS	Laser Rut Measurement System
LCDS	Laser Crack Detection System
DFT	Discrete Fourier Transform
KITTI-ROAD	Karlsruhe Institute of Technology and Toyota Technological Institute at Chicago Road
NDHM	Neighboring Difference Histogram Method
GA	Genetic Algorithm
NN	Neural Network
DSRC	Dedicated Short Range Communications
.pcap	Packet Capture
LGCM	LiDAR/Ground Calibration Method
opt-LGCM	Optimized LiDAR/Ground Calibration Method
LSCA	Least Squares Conic Algorithm
PCA	Peak Constraints Algorithm
FBDDM	Feature-Based Defect Detection Method
IDGA	Instantaneous Differential Gaussian Algorithm
GBDDM	Grid-Based Defect Detection Method
IDW	Inverse Distance Weighted
GSA	Grid Splitting Algorithm

TP	True Positives
FP	False Positives
TN	True Negative
FN	False Negative

List of Symbols

ρ	Range Distance	m
α	Azimuth Angle	°
β	Elevation Angle	°
x	Abscissa Distance	m
y	Ordinate Distance	m
z	Altitude Distance	m
ϕ_x	Pitch Angle	°
θ_y	Roll Angle	°
ψ_z	Yaw Angle	°
h	Height Distance	m
d	Euclidean Distance	m
D	Euclidean Distance	m
H	Horizontal Distance	m
V	Vertical Distance	m
$\sigma_{\alpha_i/\alpha_j}$	Difference Azimuth Angle Standard Deviation	°
σ_{x_i/x_j}	Difference Abscissa Distance Standard Deviation	m
σ_{y_i/y_j}	Difference Ordinate Distance Standard Deviation	m
σ_{ρ_i/ρ_j}	Difference Range Distance Standard Deviation	m
σ_d	Euclidean Distance Standard Deviation	m

Chapter 1

Introduction

1.1 Context

The state of road network knowledge in a country is an important issue in order to be able to deploy a rational policy of road maintenance, rehabilitation and traffic improvement. As we know, some traffic accidents are the result of the presence of disabilities or small obstacles on the roads, and one of the major problems that the population suffers from on a daily lives. Although, road traffic injuries represents a major global health problem of human safety. As a key facts, the World Health Organization (WHO) report on the Global status of road traffic safety, reflecting information from worldwide countries, indicates that the total number of road traffic deaths has plateaued at 1.15 million person in 2000. Then it increases 0.1 million to reach 1.25 million road traffic deaths in 2015 [1], [2], and 1.35 million deaths in 2018 [3]. Especially in low-middle-income countries as Africa and South-East Asia, record 95% of the world's fatalities occur on the road [4], and more than half road traffic deaths are among vulnerable road users: motorcyclists, cyclists, and pedestrians, where most of deaths and disabilities are for individuals aged 5-29 years [5]–[7]. In addition, the estimation of road traffic injuries consumption reach 3% of the gross national products of world governments, which have a serious impact on national economies [3], [4]. Therefore, the United Nations (UN) road safety collaboration has developed a global plan that proposes an 2030 agenda for sustainable development to set an ambitious target of halving the global number of deaths and injuries from road traffic crashes by 2020 [8], [9].

This thesis topic falls within this framework since it proposes to provide a geometrical and topological model of the route and to extract semantic information about the roads. In addition, these works will focus on the characterization of road surface and the presence of potentially dangerous areas, first, through a **calibration of the geometrical environment information**, followed by **detection and localization of the road defects**. It will also be important to visualize and locate the geometrical information of each defect obtained on the road.

This work is a part of the general framework of multi-sensor perception systems, more particularly focusing on the above different characteristics, that will be obtained from a telemetric information of a multi-lasers rangefinder (Light Detection and Ranging LiDAR, Laser Range Finder LRF) mounted on a vehicle. In transport applications, the development of Advanced Driver Assistance Systems (ADAS) has been the subject of much work for the past twenty years [10]. In transportation systems context, the objective is to monitor the vehicle environment in order to inform the driver, at each moment, about the potentially hazardous situations. Multi-object detection methods in data from a scanning laser rangefinder on board a moving vehicle have been proposed. Even though, these methods retain some limitations inherent in the physical nature of the measurement signal, this laser sensor has many advantages for ADAS: day/night vision, low accuracy, high frequency of measurement, directive laser shots, wide field of perception. The major drawback of a single-layer laser rangefinder is its sensitivity to pitching movements, linked to its directivity: the distances measured can be disturbed and give rise to undesirable measurements of the scene, designated by the more general term of " clutter ". The development of multi-layer rangefinders, that is to say working on several measurement planes, has made it possible to minimize these disturbances inherent in the physical nature of the measurement. Although, having the particularity of delivering precise relative positioning information unlike sensors of the video camera type, laser rangefinders are distinguished by the relative poverty of the information received on the scene (directly linked to the angular resolution of the sensor).

Therefore, it is necessary to develop solutions informing the driver by a prior information about the road defects. This information is important to obtain a statistical road defects data in order to avoid the risky accidents and to take a right decision for road enhancement in a spatial road network. Our hypothesis precisely works on an extrinsic calibration method for the LiDAR sensor based on the geometrical plane model estimation, which serves the two methods of road defects detection: feature-based and grid-based.

1.2 Thesis Aims and Objectives

In transportation applications, many articles use LiDAR to detect and track objects of interest (pedestrians, vehicles, etc...) from 3D measurements. The LiDAR sensor is also used to detect the road, often in addition to camera sensors. In these applications, the idea is to have a thorough view of the driver's environment over the widest possible horizon. Therefore, the aim of this thesis involves a LiDAR sensor with a low angle of inclination (horizontally oriented sensor) to study and analyze the road defects: holes, humps or any homogeneous out-layers. Which contribute in solving the car accidents problem that are caused by spatial dangerous areas in the road network. This study includes several scientific objectives: road defects' detection, visualization and localization.

1.3 Thesis Key Points

The key points of the thesis problem are shown in Figure 1.1, and are listed below:

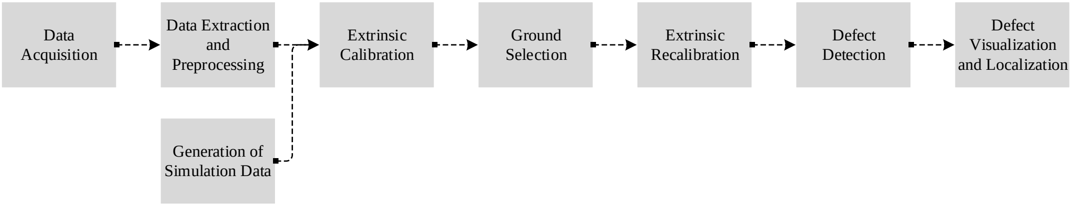

FIGURE 1.1: Thesis Block Diagram

1. Generation of simulation data on LiDAR sensor data for different orientations and altitudes.
2. Optimization of the LiDAR altitude and orientation using the synthetic data, before analyzing the coverage of LiDAR distribution points over the ground, to be suitable for the practical application and to ensure the possibility of road defect detection.
3. Data acquisition using LiDAR sensor mounted on a moving vehicle.
4. Data extraction (Range, Azimuth, Elevation, Reflectivity, and Time) from the .pcap format file. Then data preprocessing and PointCloud player presentation.
5. 3D Extrinsic LiDAR/Ground calibration method using 3D geometrical plane-based estimation.
6. Ground selection PointCloud method using differential Gaussian filter, to eliminate: the obstacles that exist on the road, and the objects that surround the road.
7. Extrinsic re-calibration for the road PointCloud to enhance the calibration process.
8. Defect Detection feature-based method.
9. Defect visualization and localization using grid-based method.

1.4 Proposed Contributions

In the context of this study (road defects detection), the LiDAR sensor is rotated toward the ground in order to increase the points' density covering the defects by the multi elevation laser. This causes a complicated modification in the ground 3D view scene with respect to the LiDAR frame. Therefore, extrinsic calibration was adopted in order to transform the LiDAR frame into a global reference frame, thus modifying the ground impact points transformation into an understandable view scene.

1.4.1 Calibration Method Novelty

The perspective of our framework is to propose a calibration method (and road plane estimation) that works under difficult experimental conditions (high angle of inclination). Indeed, we aim at developing a calibration method that allows to determine precisely the road plane in a very close vicinity of the vehicle. The idea in the long term is to detect road defects when driving on the road network. Although developed with this in mind (i.e. with a high degree of accuracy in determining the road plane), our method is general enough to be applicable in any wider operational context.

In order to attain the above key objective, this thesis addresses a new flexible extrinsic calibration method, published in [11], [12]. The proposed calibration method can be summarized by the following two-fold contributions: (1) ground plane model estimation and (2) rotation transformation matrix estimation from world ground reference to LiDAR sensor frame. The 3D Euler's angles (sensor orientation) and the height (sensor altitude above the ground) are two essential extrinsic parameters required to calibrate the full 3D LiDAR sensors, in order to improve the capability of road defect detection as will be explained in section 4.2.1. In addition, the problem is modeled by 4-DOF (degree of freedom) transformation: 3-DOF rotation and 1-DOF height, instead of 6-DOF transformation: 3-DOF rotation and 3-DOF translation. This modeling advantage provides the simplicity in the optimization process of the extrinsic parameters.

As compared to a previous plane-based methods [13], [14], the developed approach can be generalized to all types of scanning laser rangefinders and presents an optimized estimation of all extrinsic calibration parameters (angles, height). This global method can be implemented on different cylindrical LiDAR sensors (low-cost 3D and full 3D) with various range accuracy. In addition, the proposed technique outperforms in high orientation scenarios, which is a very interesting and challenging task that aims to increase the points' density coverage.

1.4.2 Road Defect Detection Methods Novelty

Moving to main thesis subject, two novel road defect detection methods are proposed, called Feature-Based Defect Detection Method and Grid-Based Defect Detection Method. The Feature-Based Defect Detection Method, based on the concavity feature delivered by second order of Differential Gaussian Filter. First, this method works on each single elevation laser individually, to detect multi road defects (pothole,hump) with homogeneous patterns and small sizes properties. This method is very sensitive to concavity feature, but it requires enough LiDAR coverage resolution on the target.

On the other hand, the Grid-Based Defect Detection Method includes two-fold contributions: (1) improved Inverse Distance Weighted interpolation method, based on the altitude distribution in a spatial grid to generate altitude georeferenced image, and (2) Grid Splitting Algorithm, provides dynamic grid size to increase the georeferenced image resolution. This method works simultaneously on all elevation lasers, it is sensitive to altitude distribution feature, and it requires high LiDAR coverage resolution to detect, visualize and localize the multi homogeneous road defects in a high resolution georeferenced image. The evaluation results show a compromised performance and impressive efficiency of our proposed defect detection methods, in terms of accuracy, precision and recall against other defect detection methods, proving the detection ability of potholes and humps defects using real data.

1.5 Report Structure

Later, after this chapter, this report introduces the following chapters:

- **Chapter 2** presents the state of the art of the thesis, which includes the difference between 2D and 3D sensors, 3D LiDAR definition, comparison between 3D LiDAR with other 3D sensors, LiDAR calibration definition and LiDAR calibration related work. In addition, it presents also the literature review of road defect detection methods based on LiDAR, Camera and Accelerometer sensors.
- **Chapter 3** presents the characteristics of Velodyne VLP-16 LiDAR sensor features, the data extraction and preprocessing operations.
- **Chapter 4** presents the geometrical impact modeling of the LiDAR sensor on the ground, and the proposed extrinsic LiDAR/Ground Calibration Method. In addition, it shows the extrinsic calibration experimental results using simulation and real data.
- **Chapter 5** presents the ground selection process, the proposed Feature-Based Defect Detection Method and Grid-Based Defect Detection Method. In addition, it shows the evaluation results of the proposed road defect detection methods, compared against other methods using real data.

Chapter 2

State of The Art

2.1 Overview

In this chapter, the organized surveys and a literature review for the thesis subject are provided. The review will start with general topic of 3D intelligent sensors evolution and will cover the emergence of laser scanner sensor compared with other 3D sensors, followed by 3D LiDAR definition and highlighting 3D LiDAR sensor among 2D LiDAR sensor, then it presents the applications of LiDAR sensor in several different fields, focusing on the importance of LiDAR sensor calibration process and the related work in this field. Finally, introduce different detection methods in the field of object detection application, followed by various road defect detection systems based on different sensors.

2.1.1 3D Intelligent Sensing Systems Evolution

With the rapid evolution of intelligent systems, these have become the focus of attention in previous years to date, and its development has begun to intensely reshape our lives. In the transportation application of roads network, the aim is to detect the surrounding obstacles of the driver (pedestrians, holes, cracks, vehicles, etc...). This process is the first step of a Driver Assistance System that warns him in case of environmental potential hazardous conditions using 3D smart sensors [15]–[18].

3D sensing systems is one of the interesting research field for this task, including localization [19]–[21], segmentation [22]–[24], recognition [25] and tracking [26]. More than that, 3D data provides more features and information of the surrounding than a 2D data, which allows a high performance and accuracy in data processing [27].

2.1.2 Laser Technology vs 3D Sensors Systems

The applications start using laser remote sensing since the 1970s. It's a popular technology, that has been developed in both the civil and military fields. We can for example cite its use in several fields of activity:

- information transfer: reading, recording, printing, holography, ...

- medical community: ophthalmology, dermatology, dentistry, ...
- police applications: cinemometer (speed control), forensics, ...
- military field: anti-missile weapons, aiming aid, ...

We focus in the following on laser rangefinders that are used in the fields of interest *i.e.* surveillance and automation.

Moving to road networks maintenance and transportation applications [28], the responsibility imposes itself in detecting and locating the road distortion (cracking, patching, potholes, rutting, shoving...). The literature review in [29] presents different automated detection experiments and extensive research conducted on pavement adversity in recent years. The work shows the importance and the incredible progress of 3D sensors compared with the other sensors, especially the laser profiler that is characterized by its high precision measurement capability, high spatial resolution and acquisition flexibility. In addition, in their survey on road and lane detection [30], the authors confirmed that the stereo imaging cannot provide the same reliability and range accuracy that laser rangefinder can.

Among several types of 3D sensors as like as stereo camera, time-of-flight camera, structure light camera and 3D laser scanner, the 3D laser scanner sensor provides the best measurement results according to [31]. In this article, the authors study the possibility of replacing a laser scanner by a stereo camera, and conclude that this approach has unsatisfactory performance when the surface has very low texture. Moreover, stereo camera provides data with lower precision in long range as compared with laser scanner, and it is vulnerable to the variation of weather conditions, but it is still used as an assistive lightweight system in autonomous vehicle for obstacle detection [32]. Although, Radio Detection and Ranging RADAR is reported in literature as an efficient system for object detection in several studies [33], [34]. However, due to their low mechanism scanning speed, they are semi-efficient for obstacle detection in road networks especially in real-time implementation [35].

2.2 Light Detection and Ranging sensor

At a glance on LiDAR sensor [36], which stands for Light Detection and Ranging, is a digital technique of remote sensing instrument, that uses light in the form of a pulsed laser to measure the surrounding environment ranges. Therefore, LiDAR sensors are attractive for environment perception because, unlike cameras, these sensors readily provide the depth information about the environment.

There exist two ways to obtain 3D telemetric data by using a LiDAR sensor: either a 2D LiDAR sensor coupled with a specific mechanism or a full 3D LiDAR. The system based on a 2D LiDAR scanner consists of a single laser beam in rotation and scanning the environment in 2D. To obtain the third

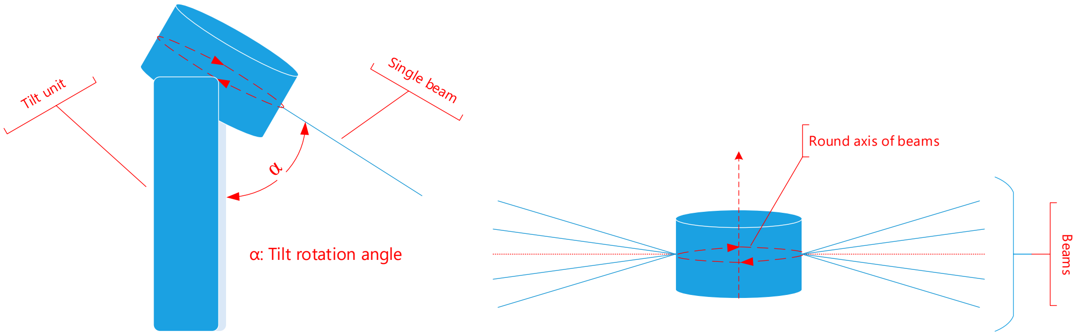

(a) (b)

FIGURE 2.1: (a) 2D LiDAR with tilt unit, (b) 3D LiDAR with various elevation beams

dimension, this LiDAR can be, for example, fitted on a tilt unit as shown in Figure 2.1a. However, the 3D LiDAR scanner consists of multi-lasers beams, oriented in different elevation and using an integrated rotational mechanism to produce various azimuth angles, in order to scan the environment in 3D as shown in Figure 2.1b.

2.2.1 LiDAR Sensor Applications

LiDAR sensor is a multi-laser scanning system that is a very interesting and efficient sensor which provides dense and accurate range measurement with high sampling rate, high angular and coverage resolution, long range distance, and generate 3D point cloud data of the surrounding area. A wide variety of promising applications, which rely on LiDAR sensors, are developed in different fields: intelligent transportation systems, mobile robotics and connected vehicles. Thus, LiDAR is a fundamental sensor contributing for indoor and outdoor applications [37] especially in autonomous mobile systems [38], [39]. Therefore, it can efficiently be used for many tasks in different applications such as civil engineering [40], environmental protection [41], planning [42], [43], autonomous vehicles and robots [44]–[46], object detection and recognition [47]–[49], scene understanding [50], Simultaneous Localization and Mapping (SLAM) [51]–[55], 3D reconstruction [56]–[60], and visual navigation [61]–[64]. Almost all of these applications appear in world challenges like Defense Advanced Research Projects Agency (DARPA) Urban and Grand Challenge [65]–[70], and support the development of Advanced Driver Assistance Systems (ADAS) [71]–[74].

2.2.2 3D LiDAR Features

Every 3D laser scanner has its specific features, which depend on the company developer. But in general rotated laser scanners have common features are expressed below (see Figure 2.2).

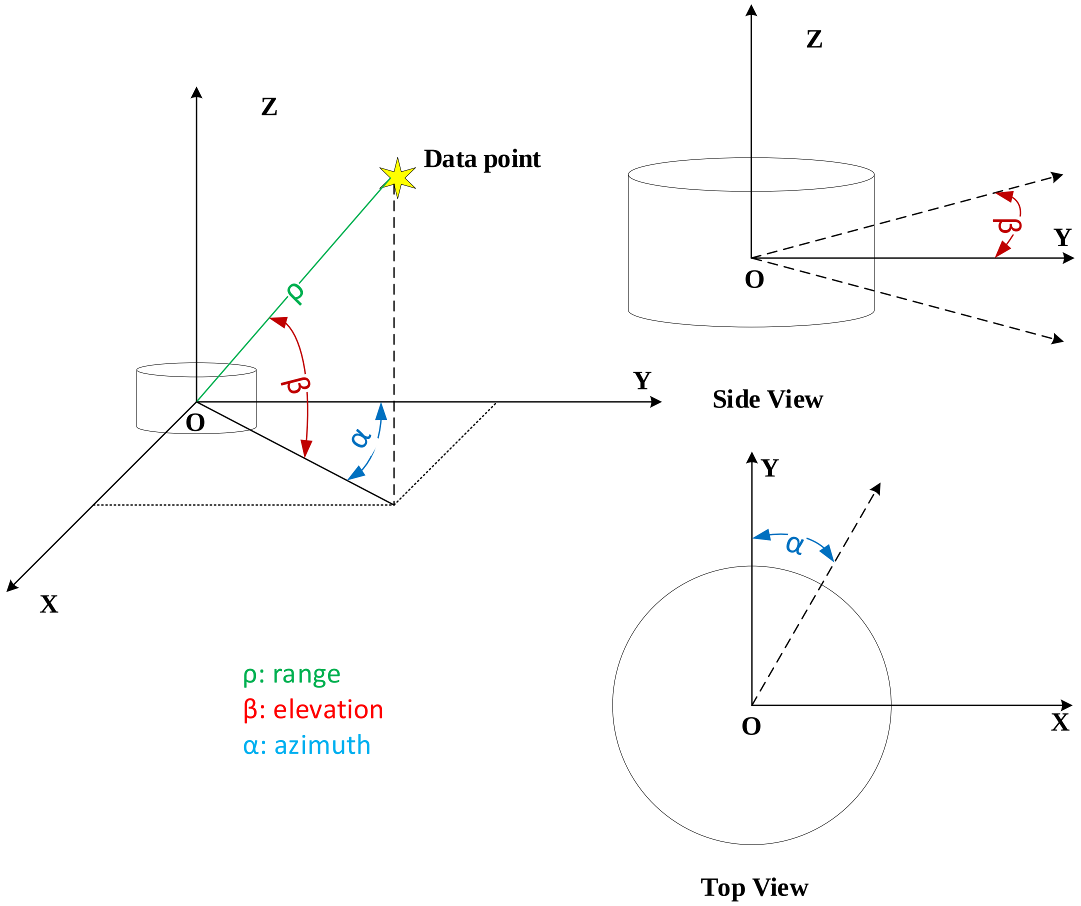

FIGURE 2.2: LiDAR polar coordinate features

2.2.2.1 Polar Coordinate Features

- **Range** ρ defines the distance from the origin O of the LiDAR frame to the reflected point on the target. Each LiDAR sensor has specific maximum range, which depend on the power of the emitted signal and the receiver sensitivity.
- **Azimuth** α defines the horizontal angle (in clockwise direction) between Y-axis and the line passing through the LiDAR frame origin O and the projection of the reflected target on XOY-plane.
- **Elevation** β defines the vertical angle (in clockwise direction) between XOY-plane and the line passing through the LiDAR frame origin O and the reflected target.

2.2.2.2 Other Usable Features

- **Timestamp** represents the acquisition time of each reflected point from the counter o'clock (timer) of the LiDAR sensor.
- **Intensity** represents the received power of the signal reflected by the surface of the target signal. This quantity depends on the surface type, as shown in Figure 2.3.

- **Range accuracy** σ_ρ describes the standard deviation of range error.
- **Azimuth accuracy** σ_α describes the standard deviation of azimuth error, often given negligible by the constructor.
- **Elevation accuracy** σ_β describes the standard deviation of elevation error, often given negligible by the constructor.
- **Horizontal FOV** represents the angular coverage by the LiDAR sensor on the azimuth coverage field.
- **Vertical FOV** represents the angular coverage by the LiDAR sensor on the elevation coverage field.
- **Azimuth angular resolution** defines the periodic angle on XOY-plane between each firing sequence.
- **Elevation angular resolution** defines the periodic angle on YOZ-plane between each laser.
- **Rotating frequency** expresses the number of rotating cycles per second.
- **Channels** expresses the number of lasers in LiDAR sensor.
- **Data rate** expresses the number of collecting points per second, where it is constant. This feature is obtained as follow:

$$Data\ Rate = \frac{Channels \times Horizontal\ FOV}{Azimuth\ angular\ resolution} \times Rotating\ frequency \tag{2.1}$$

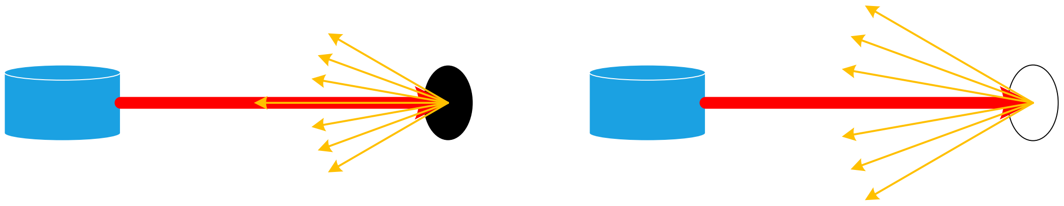

Black, absorbent diffuse reflector

White, reflective diffuse reflector

Retro-Reflector covered with semi transparent white suface

Retro-Reflector without any coverage

FIGURE 2.3: Reflector types

2.2.3 Principle of Operation

As sonars and radars, LiDAR sensor works on the principle of time-of-flight measurement. A laser diode emits an infrared laser pulse (typically manufactured about 905nm wavelength) which is acclimated by a transmitter lens as shown in Figure 2.4a. The emitted laser beam hits a target and a part of the reflected light hits a photo-diode after passing through a receiver lens as shown in Figure 2.4b.

A precise clock is used to measure the time between transmitted and received signal which in turn is used to compute the target distance from the device [75], as expressed in Equation 2.2. The intensity of the received signal is also used to define target characteristics such as reflectivity as shown in Figure 2.3, that represents the type of the reflector: absorbent diffuse reflector (black), reflective diffuse reflector (white), retro-reflector covered with semi transparent white surface and retro-reflector without any coverage. The magnitude of the reflectivity is directly correlated to the transmitted signal power, received signal power, range, and surface incident angle [76], [77].

$$D = \frac{1}{2} \times C \times (T_{receiver} - T_{transmitter}) = C \times t \tag{2.2}$$

Where:

- D is the distance between the sensor and the target.
- C is the speed of light.
- $T_{transmitter}$ is the start time of the transmitted signal.
- $T_{reciever}$ is the end time of the received signal.
- t is the relative time measurement.

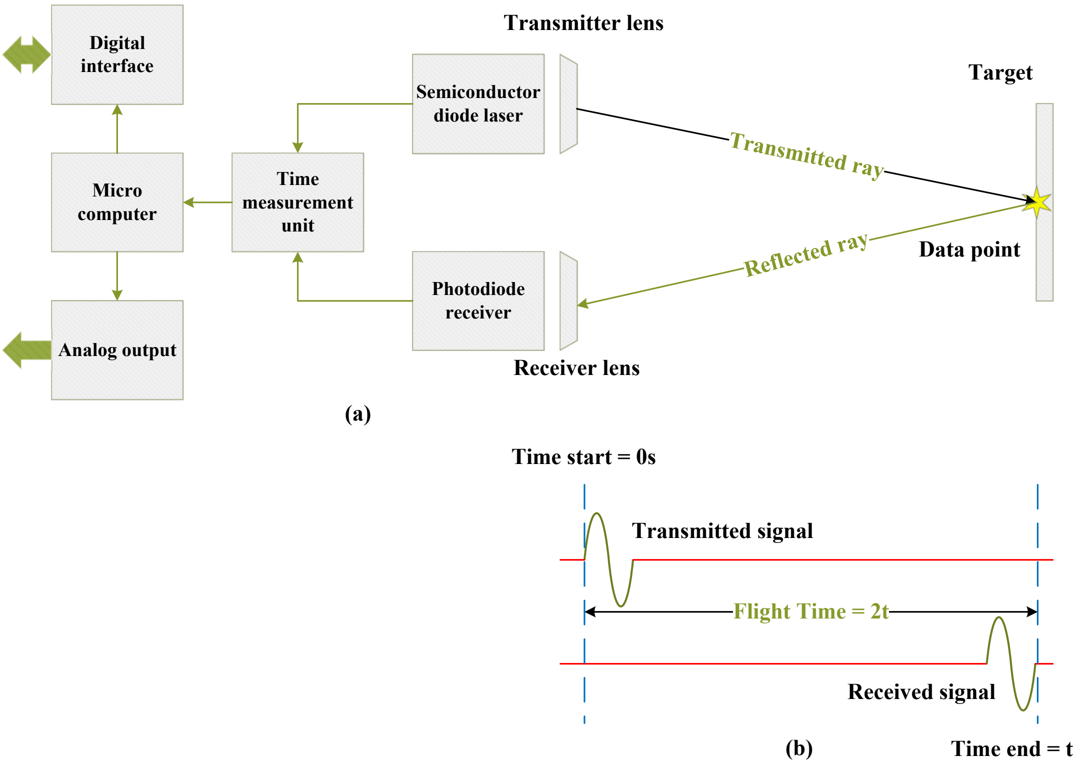

(a)

(b)

FIGURE 2.4: (a) Principle of a single-shot laser rangefinder, (b) Determination of time

The precision of the measurement is given by the standard deviation in [78]:

$$\sigma_D = \frac{t_{rise\ pulse}}{2.36 \times SNR} \tag{2.3}$$

Where:

- $t_{rise\ pulse}$ is the rise time of the laser pulse.
- SNR is the signal to noise ratio which depends in particular on the distance between the target and the rangefinder.

It should be noted that the distance between the sensor and the object can be determined, taking in consideration the:

- Angle of reflection with when the laser beam is received.
- Phase shift of the laser signal.
- Modulation frequency of the emitted signal.

The important characteristics of these sensors in the context of surveillance and detection are:

- The accuracy of the measurement.
- The horizontal and vertical angular aperture.
- The sensitivity, *i.e.* the ability to detect the obstacle in different climatic environments (rain, fog, smoke).
- The reliability, *i.e.* the ability to repeat information (robustness to roll, pitch and yaw)

This type of sensor nevertheless has some faults including:

- Sensitivity to the reflection properties of objects.
- Problems due to the refraction of light at crossing objects, clouds, etc...

2.2.4 LiDAR Usage Advantages and Disadvantages

Moreover, LiDAR sensor has several benefits other than 3D sensors [79]:

1. Quick acquisition and fast processing with high accuracy.
2. High sample density on the surface data collective, based on the angular resolution and number of lasers.
3. Additional data like intensity and precise time of acquisition along with the polar coordinates (range, azimuth, elevation).
4. Work on day and night due to the active illumination sensor. It is not affected by darkness and light, sun inclination and presence/absence of shades.

5. Integration compatibility with other data sources, which allow the fusion with other sensors (Camera, IMU, GPS).
6. Flexible with slightly bad weather scenarios.
7. Minimum human dependence, *i.e.* it works on automatic processes in most applications.
8. Cheaper cost in many applications in order to achieve high accuracy and density of data, compared with RADAR systems.

On the other hand, LiDAR sensor has some drawbacks:

1. Sparse measurement for far ranges.
2. There are no strict international protocols that guide the collection and analysis of the data.
3. Unreliable in several conditions: water depth and turbulent breaking waves.
4. The laser beams may affect human eye in case the beam is powerful.

2.2.5 LiDAR Calibration Process

In the context of problematic objective case study, the LiDAR sensor is rotated toward the ground in order to increase the points' density covering the defects by the multi elevation laser. This technical operation enhances the defect resolution and improves the possibility of **road defect detection process**. But, this causes a complicated modification in the ground 3D view scene with respect to the LiDAR frame. Therefore, a **calibration process** needs to be adopted in order to transform the LiDAR frame into a global reference frame, thus modifying the ground impact points transformation into an understandable view scene. So, the next literature will introduce the related work concerning the calibration and road defect detection methods.

LiDAR calibration is the first step that is necessary to maintain the environment measurement model. Calibration is the process of configuring the LiDAR's environment measurements to provide a result for a sample within an acceptable range. As for the other sensors, the calibration process of multi-beam LiDAR needs two steps: intrinsic and extrinsic calibration. The intrinsic calibration is the relationship between the sensor and the environment, which is applied in order to find the suitable model fitting and to estimate the intrinsic parameters of this model including the measurement errors. While the extrinsic calibration, which is important to create a worldwide frame, aims at merging common frames coming from different other sensors and to know the LiDAR position in that wide frame.

2.2.5.1 Intrinsic Calibration

The intrinsic calibration process considers the configuration of each individual beam inside the unit by modeling the process of beam creation and environment measurements. The goal is to estimate the sensor-environment relationship in terms of internal parameters, like the distance offset $D_\circ$, horizontal offset $H_\circ$, vertical offset $V_\circ$, and the additive errors $\varepsilon_\alpha, \varepsilon_\beta$ on the azimuth and elevation α, β respectively, as shown in Figure 2.5.

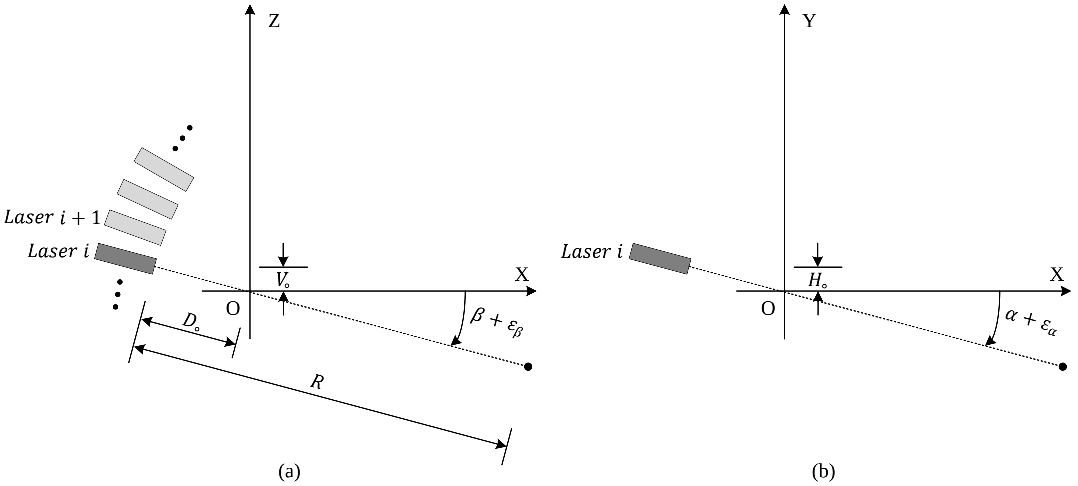

(a) (b)

FIGURE 2.5: (a) Scanner parameters in vertical plane, (b) Scanner parameters in horizontal plane

2.2.5.2 Extrinsic Calibration

The extrinsic calibration process aims to determine the relationship between the LiDAR frame and other reference frame. The transformation between both frames is often composed of one rotation $\overrightarrow{R}(\psi_z, \theta_y, \phi_x)$ and one translation $\overrightarrow{T}(X_\circ, Y_\circ, Z_\circ)$ transformations as shown in Figure 2.6. Indeed, it is necessary to estimate the 6-degree of freedom extrinsic parameters ψ_z, θ_y, ϕ_x, $X_\circ, Y_\circ, Z_\circ$ in order to transform the LiDAR frame to the reference frame.

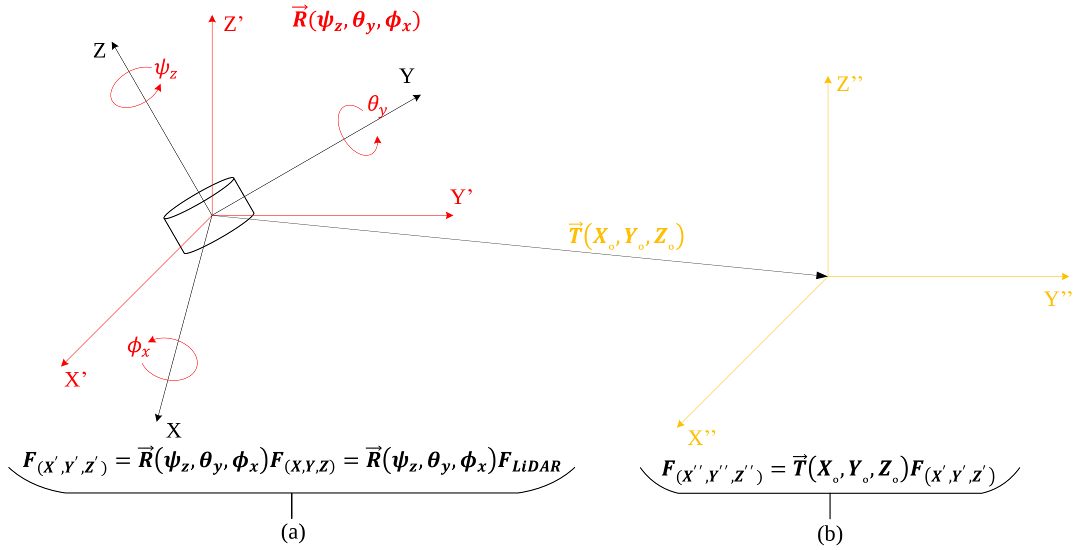

FIGURE 2.6: (a) 3D orientation of LiDAR frame, (b) 3D Translation of LiDAR frame

2.2.5.3 Related Works

Numerous authors investigated intrinsic and extrinsic calibration methods in LiDAR sensors. An intrinsic calibration method is presented in [80]. The calibration process is based on an optimization method, where the calibration pattern is a wide planar wall on a flat surface scanned using Velodyne HDL-64E. In addition, a static calibration method is presented in [81], to derive an optimal solution for the laser's intrinsic calibration parameters by a planar feature-based least squares in advantage of minimal constrained network. A study in [82] shows a correlation between the internal operating temperature of the LiDAR and the Laser scanner ranging error (intrinsic parameter). The calibration process considers a planar calibration approach to estimate the internal parameters for Velodyne VLP-16.

On the other hand, an extrinsic calibration method is presented in [83]. In this method, a flat plane is used for the calibration and an algorithm based on the inequality of two symmetric rays in azimuth with respect to the origin is proposed. This inequality is due to the shift angle of the center line. Another extrinsic calibration method is presented in [84], where the authors work on a 2D laser scanner and on the rotating platform to extract the rotation axis and radius using point-plane constraint. The Levenberg-Marquardt optimization method is applied in the two above extrinsic calibration methods to optimize the non-linear least squares function problem.

An extrinsic calibration method for a low-cost 3D LiDAR (based on a rotating 2D LiDAR) is proposed in [13] using an iterative maximization of 3D plane parameters (flatness and visible area). These parameters are extracted by Random Sample Consensus (RANSAC) method, which is a time consuming method. The authors use a fixed 2D LiDAR that requires multi-scan frames to provide a single 3D point cloud frame, by which the yaw angle is not considered in the calibration. An extrinsic calibration method is proposed in [14], using a similar low-cost 3D LiDAR where each extracted plane is calibrated separately in order to improve the estimation of extrinsic parameters without using extra hardware.

In [85], a numerical algorithm is presented to compute both of the intrinsic and extrinsic parameters by minimizing the systematic errors due to the geometric calibration factors. Another approach is introduced in [86], which computes the intrinsic and extrinsic parameters of LiDAR sensor (Velodyne HDL-64E) by unsupervised calibration for each of multi-laser beams. An optimization function seeking to minimize the point-to-plane iterated closest point is then proposed.

2.3 LiDAR-Based Object Detection Process in Transportation Systems

The fundamental support technology behind advanced driver assistance systems ADAS is object detection, that enables cars to detect driving lanes or perform pedestrian and vehicle detection to improve road safety. Several methods implemented for object detection are useful in multiple applications such as video surveillance, image retrieval and telemetric LiDAR systems. Each method is based on a specific scientific approach (feature-based, model-based, grid-based, histogram-based, etc...), and this is what distinguishes it from others. The next subsections will present a brief explanation for numerous applications in the context of object detection field using different sensors: Camera, GPS, 2D LiDAR and 3D LiDAR.

2.3.1 Road/Road Boundary and Obstacle Detection Approaches

Some of the interesting challenges in autonomous vehicle application are road, road boundary and obstacle detection, with several approaches developed in this field. In [87], the authors present two previous approaches to detect the breaking points A, B, C, D, E, F, G, H using LiDAR sensor as shown in Figure 2.7, where the major detection term refers to the altitude and the inclination angle of the LiDAR's laser beams. The principle of breaking points detection depends directly on the smooth change of the range points or the distance between the points. The segments are then obtained from the breaking points to identify or classify whether these segments are: logical roads, physical roads, obstacles, blind spot or road boundaries. For clarification, the logical road is a part of the road where the vehicle can pass through it as the segment $[EF]$, while the physical roads are parts of the road that the vehicle can not pass through as the segments $[AB]$ and $[GH]$. The blind spot is a hidden zone that cannot be covered by the LiDAR laser beam as the part between the two points B and C.

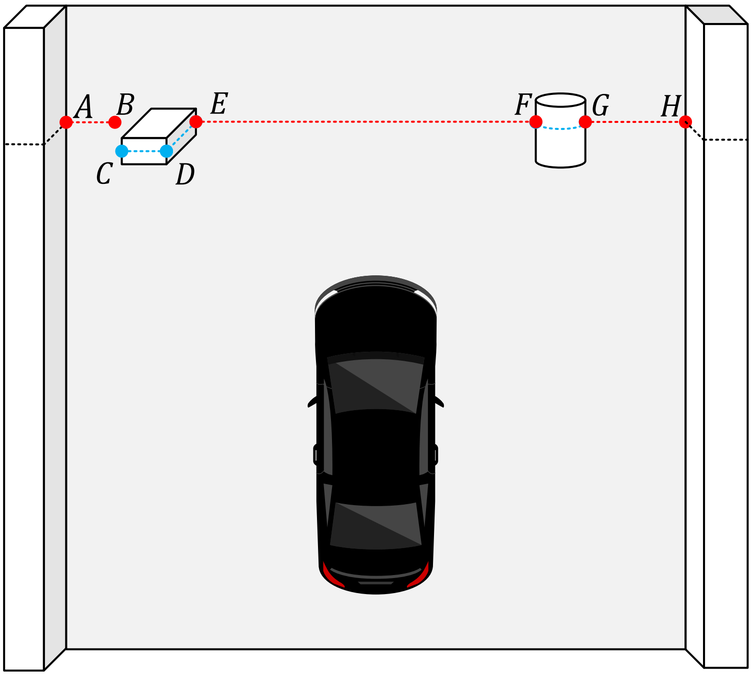

FIGURE 2.7: Road breaking points and laser beams propagation with some obstacles

According to the LiDAR laser beams shown in Figure 2.8, in the first approach [88], if the measured distance between the two consecutive points P_1, P_2 is greater than a constant threshold d_{th} as expressed in Equation 2.4, and the tangent of the passing line through the two points P_1, P_2 is greater than a constant threshold tan_{th} as expressed in Equation 2.5, then the two points P_1, P_2 are supposed to be breaking points.

$$\sqrt{(x_i - x_{i+1})^2 + (y_i - y_{i+1})^2} \geq d_{th} \tag{2.4}$$

$$\left| \tan^{-1}\left(\frac{x_i - x_{i+1}}{y_i - y_{i+1}}\right) \right| \geq tan_{th} \tag{2.5}$$

However, in the second approach [35], if the difference between the range ρ_{i+2} of point P_3 and the range ρ_p is greater than a constant threshold ρ_{th} as expressed in Equation 2.7, then the points P_3, P_2 are supposed to be breaking points. Where the value ρ_p is a measured range depend on the ranges of the two previous consecutive points P_1, P_2 and the azimuth angular resolution α as expressed in Equation 2.6.

$$\rho_p = \frac{\rho_i \rho_{i+1}}{2\rho_i \cos\alpha - \rho_{i+1}} \tag{2.6}$$

$$\left| \rho_{i+2} - \rho_p \right| \geq \rho_{th} \tag{2.7}$$

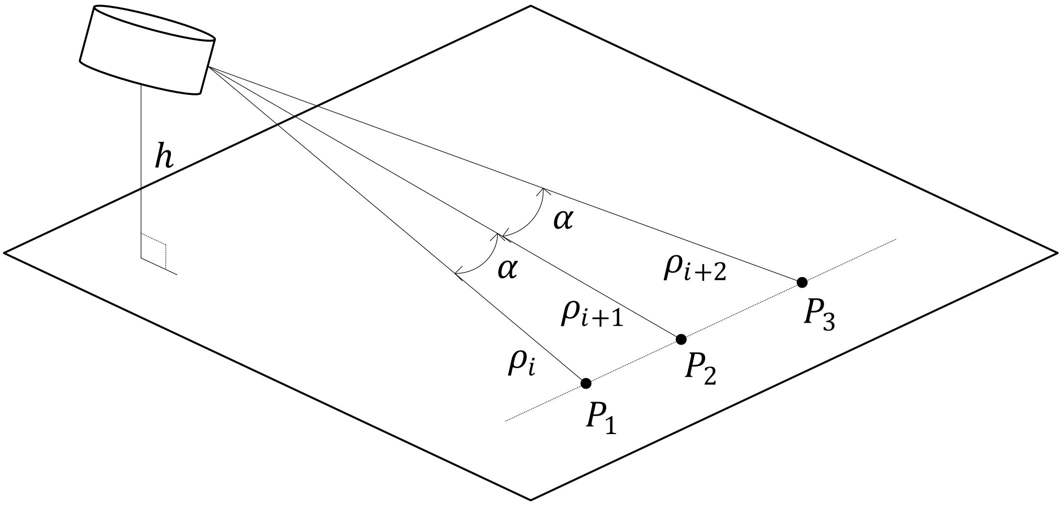

FIGURE 2.8: LiDAR sensor aligned with a downwards-looking angle

Some detection and localization applications in autonomous mobile robotic systems needs a fusion of multi-sensors in order to get better precision and accuracy. In [89] the authors propose a road detection approach based on the depth feature of the 3D LiDAR and 2D imaging. The approach is built up of four stages as depicted in Figure 2.9. The main goal of this article is to explain how to generate a reconstructed image (in 2 dimensions) by projecting 3D LiDAR points to 2D image based on height distribution of the neighboring region of each point. Then morphological operations are applied to detect the edges of the image.

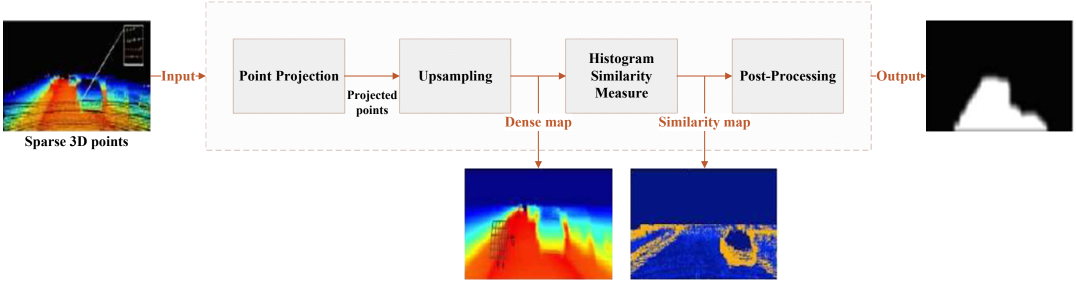

FIGURE 2.9: Four main stages for road detection approach [89]

Machine Learning [90] takes into account all the suitable factors, thus called as features, in order to get the best evaluated model that classifies or recognizes the input object by its appropriate features. In [91], the author proposes a sequential method for road and road edge detection including five steps as shown in Figure 2.10.

In this article, a number of candidate points are selected as an input of a Support-Vector-Machine (SVM) classifier in order to extract the suitable features and to classify these points as belonging to the road or not. Then, a false alarm mitigation is used to detect the road segments. This framework

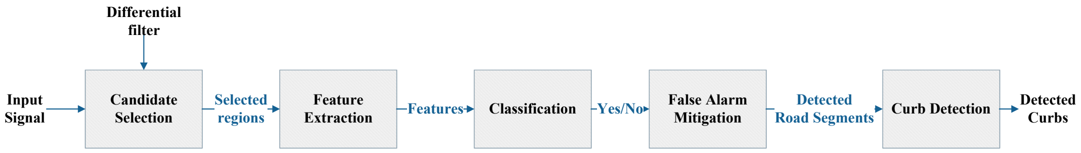

FIGURE 2.10: Flowchart of road/road-edge detection algorithm [91]

has been validated through the DARPA urban Challenge scenarios to show its efficiency and robustness.

2.3.2 Lines Extraction Algorithms for Multi-Vehicle Tracking

In [92], the authors introduce a survey including six line extraction algorithms: Split-and-Merge [93], Line-Regression [94], Incremental [95], RANSAC [96], Hough-Transform [97] and Expectation-Maximization [98]. The algorithms are compared on 2D points using laser rangefinder. In terms of speed and correctness, the authors prove that the Split-and-Merge and Incremental algorithms are more efficient among the other algorithms.

While in [99], [100], the authors propose a new lines extraction algorithm, called Geometric Invariant algorithm, which is efficient in terms of number of extracted and rebuilt segments (as comparison, the Split-and-Merge algorithm extracts 50% more segments in order to describe the same scene). This algorithm is based on parameterized geometric feature (Polar points) that provides more efficiency as compared to other point-based algorithms (Cartesian points). A statistical test based on Mahalanobis distance is applied at the end of the algorithm in order to merge the segments [101], which increases the efficiency of this method of segmentation. The Geometric Invariant algorithm is also used in a vehicles tracking model-based approach in [102], applied on a real data collected from IBEO LD automative scanning laser telemeter, mounted on a moving ego-vehicle whose velocity is estimated using a GPS sensor.

2.4 Road Defect Detection Systems

Ground defect detection is one of the interesting fields in autonomous driving vehicles and robotics applications. Till now, these types of applications are mostly vision-based in our current era, which witnesses many developments in that field. The interesting challenge is to develop ground defect detection methods based on the LiDAR sensor that has advantage against the camera and accelerometer sensors. In the next subsections, a detailed explanation review on road defect detection approaches based on LiDAR sensor, and a brief description of other related approaches based on Camera and Accelerometer sensors are presented.

2.4.1 LiDAR-Based Defect Detection Approaches

A first study in [103] describes two road surface anomalies detection systems using two high resolution and very low accuracy laser profiler mounted on a moving vehicle as shown in Figure 2.11, where X-axis (transverse) resolution is equal to $1mm$ and Z-axis (depth) accuracy is equal to $0.5mm$.

(a) The laser profilers mounted on the vehicle's back

(b) The laser profilers hardware

FIGURE 2.11: Laser profiler system [104]

The first one is Laser Rut Measurement System (LRMS), that detects and characterizes the pavement rutting in four steps: filtering low frequencies and linear approximation of the laser profile, then search for the rut support points and finally measurement of the rut characteristics, as expressed in Equations 2.8 and 2.9 and shown in Figure 2.12.

$$Rut\ Depth = \sqrt{(x_B - x_T)^2 + (z_B - z_T)^2} \tag{2.8}$$

$$Rut\ Width = \sqrt{(x_R - x_L)^2 + (z_R - z_L)^2} \tag{2.9}$$

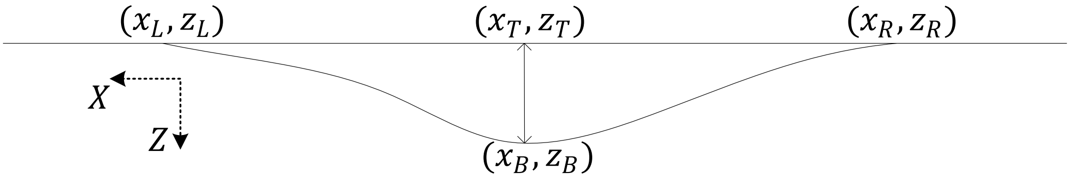

FIGURE 2.12: Manual rut

The second one, detailed in [104], [105], is a Laser Crack Detection System (LCDS) which was developed in order to generate a crack map from several 3D profiler scans. The algorithm was implemented in two major steps.

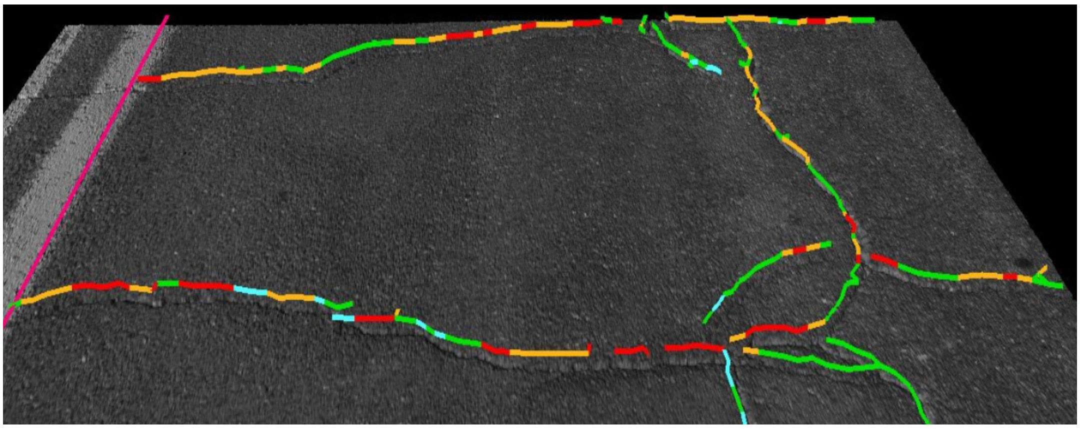

FIGURE 2.13: Road crack map

The aim of first step is to find the candidate cracks points in each individual road profile. It works for each $3cm$ segment of the 3D road profile, each segment is overlapped at the central point of an another neighbor segment. The candidate hole is detected in each segment by searching for the minimal elevation point and the two maximal elevation points, where the hole depth is measured as the difference between the minimum elevation point and the average of the two maximum elevation points, and the hole width is measured as the distance between the two maximum elevation points. If the hole depth is beyond a minimum threshold, and the hole width is less than a maximum threshold, then it is considered as a potential candidate crack. The depth threshold was set to filter the high frequencies of the points' elevation signal. At the end, the first step shows a series of candidate crack points from various profile scans.

While, the aim of the second step is to validate the candidate crack points in order to eliminate the spurious points, and to produce a crack map. The process in this step is executed to find the neighborhood point of each potential crack point. If the neighbor point is closer than a maximum threshold distance, then the two crack points are connected by a line segment as shown in Figure 2.13. Finally, the remaining unconnected candidate crack points are eliminated.

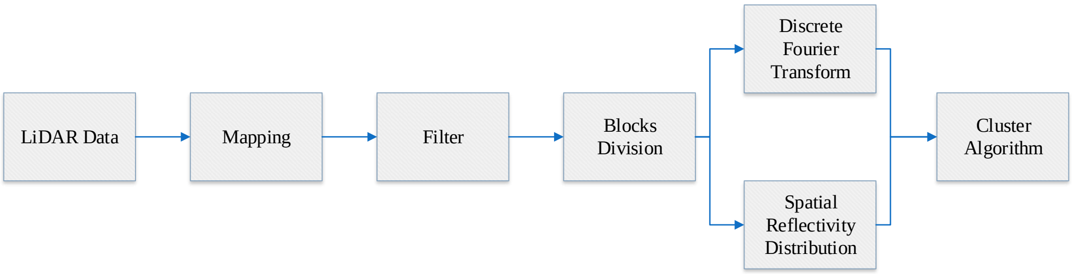

FIGURE 2.14: Diagram for automatic defect detection method [106]

An automatic defect detection method study in [106] shows that the LiDAR reflectivity (intensity) is an important property that supports ground surface evaluation. It starts by mapping the 3D point cloud on the horizontal XY-plane, ignoring the altitude Z coordinate and exchanging it by the laser reflectivity, then a filtering operation is applied in order to remove the noisy points, followed by a block division operations on the map. The main principle of this method is to cluster the ground blocks to one of these three essential classes: asphalt, painting and cracks. A hierarchical clustering algorithm is utilized on each block, depending on the intensity histogram and the 2D Discrete Fourier Transform (DFT) intensity spectral features as shown in Figure 2.14. Through the above analysis, the authors highlight the identification role of the **intensity histogram** feature that shows a clear difference between the three classes.

Another efficient histogram-based detection method was proposed in [107] to detect the obstacles, holes and water hazards. This method is evaluated on the KITTI-ROAD data-set [108] and has obtained a promising performance result on a **large size object** existence compared with [109], [110].

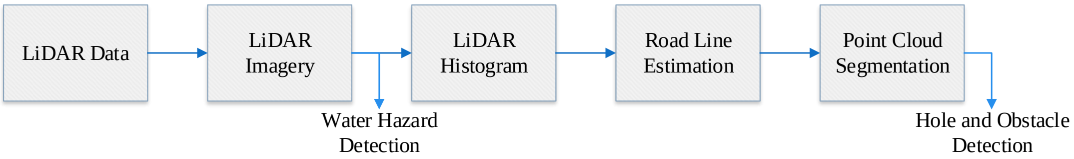

FIGURE 2.15: Diagram for obstacle and water hazard detection method [107]

Referring to Figure 2.15, the method begins by transforming the 3D point cloud to 2D image according to the spherical coordinate azimuth and elevation α, β respectively, and the range ρ represented by the pixel intensity in order to obtain a **depth image**. The water hazard spot is represented by black color pixels in the depth image due to laser pulse miss back bouncing to the receiver, because of specular reflection and absorption between laser and water. Then a histogram study is applied on each row line in the depth image, followed by road line estimation and road segmentation using RANSAC algorithm, taking into consideration a tolerance margin due to the non flatness of the road surface.

Normally, the measured ranges from the LiDAR sensor to ground plane have nearly the same values on each individual horizontal line. But when an obstacle exists on the road, the obstacle reflected ranges are shorter than the road line ranges. On the contrary side, the hole reflected ranges are longer than the road line ranges because of the object altitude when its above or below the road plane as shown in Figure 2.16.

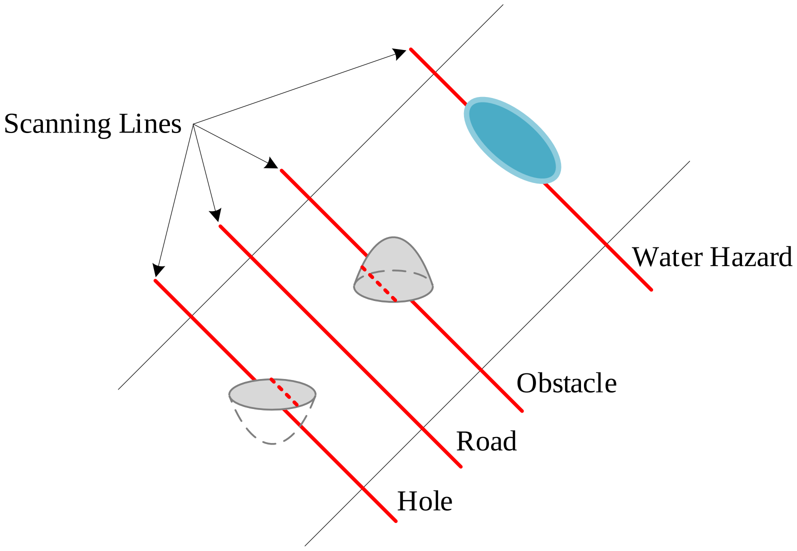

FIGURE 2.16: The effect of laser scanning line on obstacle, hole and water hazard spot

Whereas in [111], the authors work on a simple speed hump detection method as shown in Figure 2.17, starting with acquisition of low cost LiDAR datapoints, then removing the noise using median filter, followed by comparing the difference of each consecutive neighboring sets, in order to mark the points as speed hump if the difference varies between two constant thresholds. Finally, the authors cascade their system with camera to enhance the results of speed hump detection.

FIGURE 2.17: Diagram for speed hump detection method

2.4.2 Vision-Based Defect Detection Approaches

A segmentation pavement distress thresholding algorithm from background images was proposed in [112], based on Neighboring Difference Histogram Method (NDHM) using a weighted statistical numerical value difference for each cracking pixel with their surrounding pixels. Therefore, the neighboring differential statistical numerical value was selected as a feature in order to identify the target region as potholes using nonlinear Support Vector Machine (SVM) classifier. Experimental results show a high recognition accuracy. However, the polluted potholes and environmental conditions such as sunlight and visibility are encountered as detection difficulties.

In [113], an adaptive method was proposed for pavement distress detection and classification based on Genetic Algorithm (GA) and entropy theory [114].

The process aims to choose the optimal threshold segmentation by an objective function based on the captured pavement images and maximized by information theory. A vertical and horizontal distress measures are computed, by accumulating the difference between the numbers of distressed tiles in an adjacent columns and rows respectively. The vertical and horizontal distress measures with the total number of distress tiles were fed to a three layer feed-forward Neural Network (NN) classifier to identify the type of pavement distress (pothole, crack). The experimental results of the threshold segmentation technique based on GA show a better performance among the Otsu segmentation method [115].

In addition, a proposed method [116] for automated potholes detection in asphalt pavement images presents a segmentation algorithm that depends on a histogram shape-based threshold to segment the images into defect and non-defect region. According to the geometric properties of the defect region, the potential potholes shapes are extracted using morphological thinning operations [117] and elliptical regression [118]. Afterwards, the potential pothole shape is compared to the texture of the non-defect surrounding pavement in order to identify the interest region as a potential defect. Experimental results show that an accurate technique was developed to detect the potholes from pavement images.

An improved pavement videos recognition method is proposed in [119] which is a continuation for the previous work in [116]. The method incrementally updates the texture signature for intact pavement regions, and uses a kernel-based vision system to track detected potholes taking in consideration the texture and shape of the object [120], [121]. Hence, the approach obtained an effective pothole detection in the appearance of a global pavement surface design.

Furthermore, a general framework that provides a centralized system which detects potholes on roads and assists the driver to avoid them was proposed in [122]. A laser line stripper sensor attached to the vehicle [123] is used to send out a plane of light that intersects with objects which in turn is viewed by a camera. The camera has a band pass filter to suppress background illumination and stands out the projected laser line in the resulting image. Then the line in the image is transformed into cartesian coordinates by a triangulation operation. When a potholes is detected, an inter-vehicle protocol such as Dedicated Short-Range Communications (DSRC) channel broadcasts a notification message containing its GPS location [124], to warn immediately the other nearby vehicles. This process increases the accuracy of the system by eliminating the delay at the server end.

In [125], the authors proposed a K-means clustering-based algorithm for potholes detection. The algorithm is implemented on the region of interest segmentation, which uses Hough transformation technique [126] to detect lines and curves in a capture image. The experimental results show a sufficient performance.

A robust method supported by heuristically derived decision logic for automated detection and assessment of potholes, cracks and patches from real life video clips highways is presented in [127]. This approach uses various image processing methods: segmentation, median filtering, weighted mean based adaptive thresholding, morphological operation, connected component labeling and chain coding techniques [128]–[132]. At the end of the proposed method, the extracted information can be used for determining maintenance levels of the roads, in order to take the suitable actions for repairing and rehabilitation. In terms of robustness and efficiency, the experimental results show the defect detection ability in an effective and accurate process.

Moreover, a technique based on an laser image for pavement distress detection was proposed in [133]. The process includes a three layer feed-forward Neural Network [134], fed with four computed numerical features: vertical distress measure, horizontal distress measure, depth index and total number of distress tiles, in order to identify pothole severity and to classify the crack type. Finally, the experimental results demonstrate that the proposed model works well for potholes and cracks detection.

2.4.3 Accelerometer-Based Defect Detection Approaches

A data acquisition hardware that was used to develop a vibration-based system for preliminary evaluation of pavement conditions is proposed in [135]. The vibration-based system senses the ground conditions based on mechanical responses of the testing vehicles, where the cracks and surface rutting impose impacting force on the vehicle. The pavement surface conditions can be estimated from the recorded responses of the testing vehicle when driving on the pavement. This system has the advantage of being cost-effective, having small storage requirement and amenable for automatic real-time data processing. However, it does not provides a complete details on distress characteristics as the video-based system. In addition, the video-based systems has the advantage of collecting a prior information about the pavement distress before crossing it.

Another vibration-based system is proposed in [136], where public transportation system based on network sensor BusNet is used to monitor the road surface condition, by adding an acceleration sensor boards to the system. BusNet is a network sensor initially designed to monitor environmental pollution using sensors mounted on a public transportation buses. The collected acceleration readings are transmitted over the BusNet to the central main station collection point. The process based on preliminary results, is still in process for collection of more data for developing an analytical model.

An investigated application of mobile sensing to detect and report the surface conditions of roads was proposed in [137]. The authors developed pothole patrol system gathering data from three axis acceleration sensor, and GPS devices deployed on embedded computers in the vehicle. They identified potholes and other several road surface anomalies from the accelerometer data, using a machine-learning approach. Also, the authors uploaded the detection results to a central server via opportunistic WiFi modulation provided by participating open WiFi access points, or using an available cellular data service. The vibration-based method may provides false positive and false negative results due to the manhole existence that can be detected as potholes, and potholes position at the middle of the road that cannot be detected using accelerometer because of no contact with any of the vehicle's wheels.

2.5 Conclusion

This chapter presents an explanation on the 3D LiDAR sensor and its features, and the advantage of LiDAR sensors among the other sensors. In addition, the literature review is introduced on the general application of LiDAR sensor, and highlights the related work of LiDAR calibration methods and defect detection methods using different senors as LiDAR, camera and accelerometer. The addressed popular plane-based extrinsic calibration methods in [13], [14] are modeled on the concept of 6-DOF. Whereas, our proposed extrinsic plane-based calibration method LiDAR/Ground Calibration Method is modeled on concept of 4-DOF, which indicates the simplicity of our proposed model, but it's not realistic to compare the evaluation results due to the difference of the modeling concepts between the 6-DOF and 4-DOF. Moreover, the most important defect detection method is depth's histogram-based [107], which records the first rank using benchmark evaluation results.

Chapter 3

LiDAR Measurement Modeling

3.1 Introduction

After presenting some of the background works related to this thesis processes in chapter 2, this chapter will explain in details the technical and specifications of the LIDAR model used to understand and describe the application setups, which are summarized in the first two blocks of the thesis diagram *i.e.* data acquisition, followed by data extraction and preprocessing as shown in Figure 1.1. Basically, the experimental configuration of the LiDAR sensor is an important initialization step to reach the main final goal, which imposes itself technically to attain a good setups, so that the data is ready to be processed.

3.2 Velodyne VLP-16 Sensor

FIGURE 3.1: LiDAR VLP-16 3D PointCloud System

From now on, we will consider the Velodyne VLP-16 LiDAR as shown in Figure 3.1, which is the telemeter used for the experimental data acquisition part of our works. Unlike many other LiDARs used in this kind of applications, the VLP-16 has its own internal processor and network interface as shown in Figure 3.2.

This sensor contains 16 vertical firing planes (emitter/receiver pairs) and is able to acquire up to two returns per one laser shot in dual mode. It spins around its vertical axis and provides an horizontal FOV of 360°. The vertical FOV is equal to $[-15°, 15°]$ with 2° spacing between each pair of adjoining

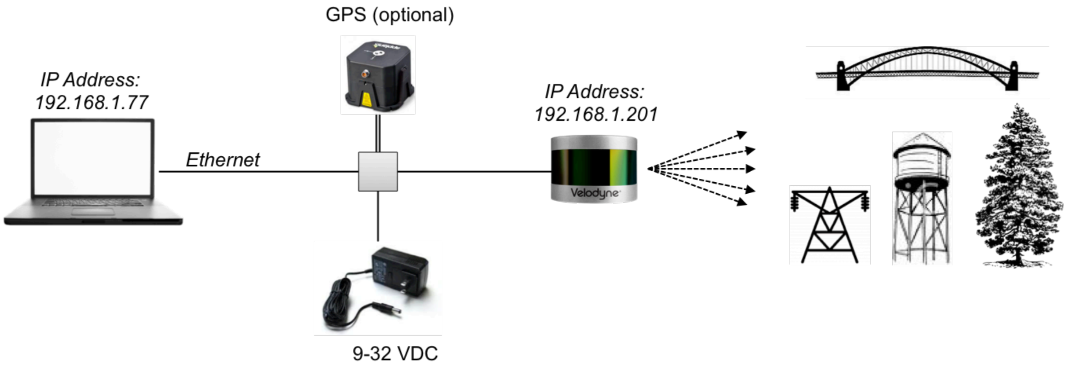

FIGURE 3.2: LiDAR VLP-16 3D PointCloud System [138]

firing planes (**elevation angular resolution**). A relevant usable return can be between $1m$ (**minimum range**) and $100m$ (**maximum Range**), and up to 300000 points per second can be measured (**data rate**). The azimuth angular resolution is a free selection variable choice $0.1°, 0.2°, 0.4°$, and it is respectively correlated to the rotating frequency $20Hz, 10Hz, 5Hz$. The received intensity value is enrolled between 0 and 255 (**reflectivity**). This sensor is also characterized by a range measurement accuracy of $3cm$ (for more details about Velodyne VLP-16 LiDAR sensor products [138]).

3.3 Data Extraction

As mentioned in the previous section, the data from the packet capture file *.pcap* are extracted depending on the flags ($0 \times FFEE$, see Appendix A.2) in successive way (point by point). Every point is characterized by its features (range, azimuth, elevation, reflectivity or intensity, and time), and the Cartesian coordinates (x, y, z) are computed by the 3D conversion from polar coordinates ρ, α, β to Cartesian coordinates as it will be described in Chapter 4. Finally, the data of each point will be stocked in memory as shown in Table 3.1.

There exists a second fast recommended way by using VeloView software, where this software supports a service to export the 3D point cloud data in to Excel *.csv* files. Each file represents one scanning frame, however the frames must be concatenated then separated due to the point cloud interference or overlap problem between each two successive frames.

TABLE 3.1: PointCloud features

	Range	**Azimuth**	**Elevation**	**Intensity**	**Time**	**X**	**Y**	**Z**
Point 1	ρ_1	α_1	β_1	I_1	t_1	x_1	y_1	z_1
Point 2	ρ_2	α_2	β_2	I_2	t_2	x_2	y_2	z_2
$\vdots$	$\vdots$	$\vdots$	$\vdots$	$\vdots$	$\vdots$	$\vdots$	$\vdots$	$\vdots$
Point n	ρ_n	α_n	β_n	I_n	t_n	x_n	y_n	z_n

3.4 Data Preprocessing

In Data Preprocessing block, a developed algorithm aims to solve the non-periodic azimuth angular resolution problem in each LiDAR frame. The algorithms is composed in two steps: frames separation and points associations. Therefore, in the next subsections the preprocessing parts are explained in details.

3.4.1 Frames Separation

In this first step, the PointCloud data must be separated into individual frames from all points in the above Table 3.1, since this table delivers all the frames in successive and sequential order. Each scanning frame represents a complete cycle around the z-axis of 360°. Since the azimuth angular resolution is set to 0.2°, that means each scanning frame will start with azimuth angle between $[0°, 0.2°]$ and end with azimuth angle between $[359.8°, 360°]$ (see Figure 3.3) due to the angular shift error of the motor rotating frequency problem.

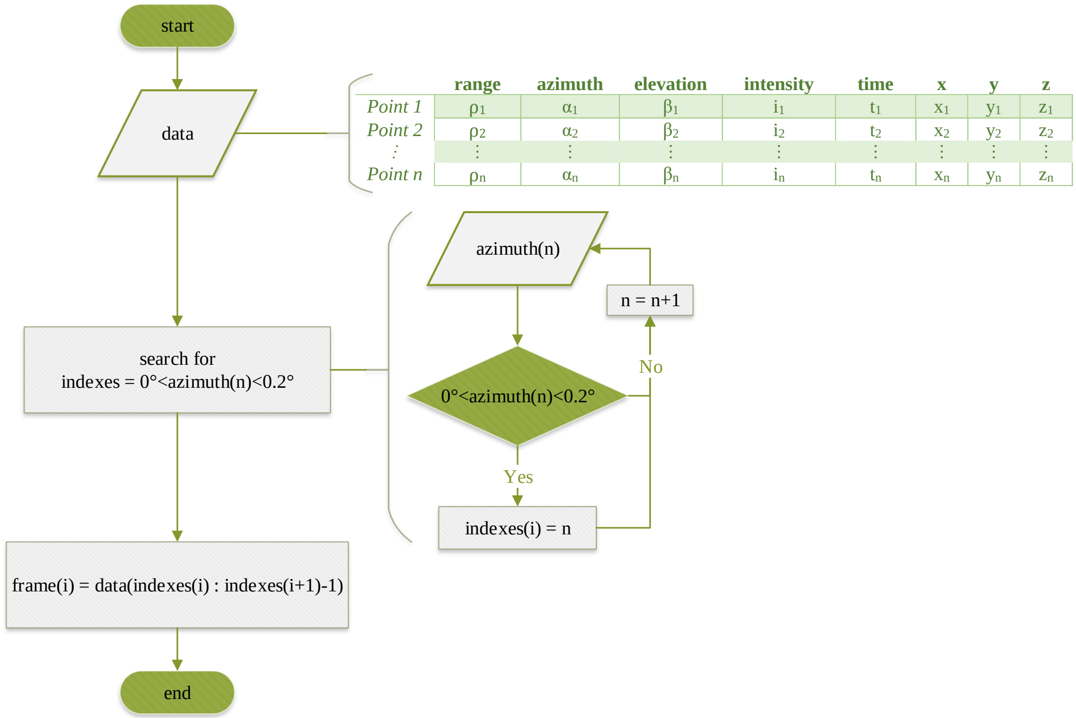

FIGURE 3.3: Data preprocessing flowchart

Indeed, the asynchronous start of recording, the LiDAR begins, in first frame, to collect data during a cycle in progress, i.e. from an angle bigger than 0.2°. The same problem exists for the last frame that stops scanning at an angle less than 359.8°. Which means that the first and last frames are incomplete scanning frames as shown in Figure 3.4. Therefore, the first and the last frame should be eliminated.

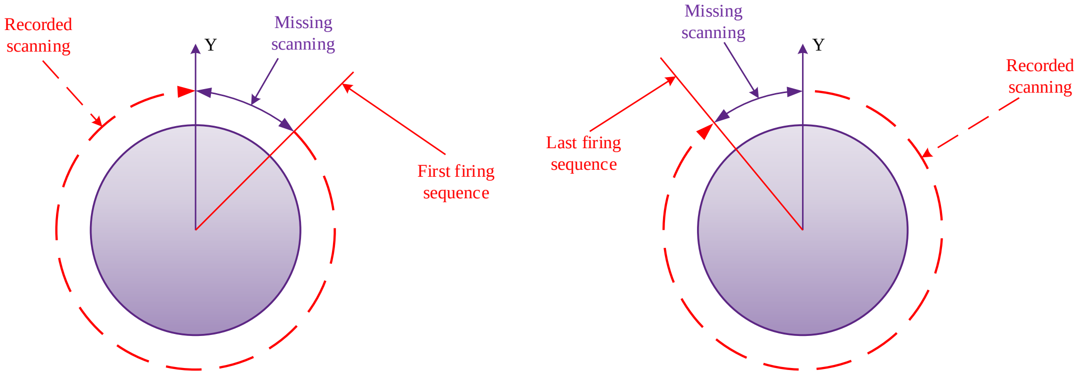

First Scanning Frame **Last Scanning Frame**

FIGURE 3.4: First and last scanning frames

3.4.2 Points Association

In the second step, the preprocessing will focus on the azimuth feature, to provide an arithmetic sequence with the azimuth angular resolution, which will earn an advantage by using it in orderly algorithms. As for the elevation, it is ready and regular, especially for close ranges, because it has constant angular resolution.

After frames separation step, each frame is composed of different number of points because there is no arithmetic sequential angular resolution for azimuth, due to the rotation nature of sensor motor (drifted angular resolution) and may be to the non-periodic firing timestamp. Therefore, we implement an algorithm with periodic azimuth angular resolution 0.2°, by associating the points features to the nearest new azimuth if the difference is less than half the angular resolution as shown in Figure 3.5. Otherwise, the algorithm adds a zero padding points with zero point features to the new azimuth (see Table 3.2).

TABLE 3.2: Zero padding point in a point cloud frame

	Range	**Azimuth**	**Elevation**	**Intensity**	**Time**	**X**	**Y**	**Z**
Point 1	ρ_1	α_1	β_1	I_1	t_1	x_1	y_1	z_1
Point 2	ρ_2	α_2	β_2	I_2	t_2	x_2	y_2	z_2
⋮	⋮	⋮	⋮	⋮	⋮	⋮	⋮	⋮
Zero padding	0	α_5	β_5	0	0	0	0	0
⋮	⋮	⋮	⋮	⋮	⋮	⋮	⋮	⋮
Point 2800	ρ_{28800}	α_{28800}	β_{28800}	I_{28800}	t_{28800}	x_{28800}	y_{28800}	z_{28800}

The aim of this algorithm is to modify the frames for a specific angular resolution with constant number of points 28800 $points/frame$ as expressed in Equation 3.1.

$$\begin{aligned} frame\ points\ number &= \frac{360^\circ \times Channels}{Azimuth\ angular\ resolution} \\ &= \frac{360^\circ \times 16}{0.2^\circ} = 28800\ points/frame \end{aligned} \tag{3.1}$$

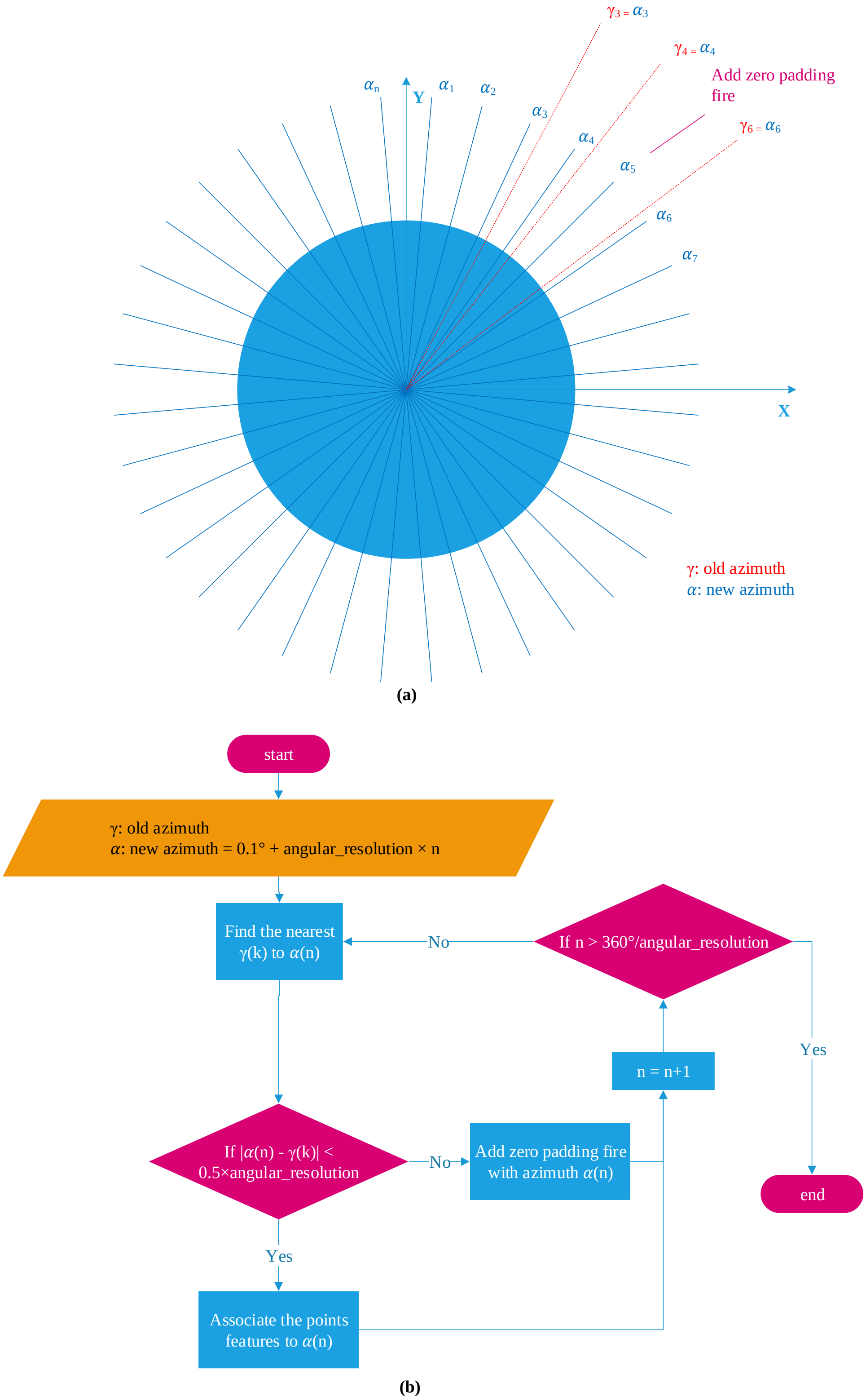

FIGURE 3.5: (a) Top view for old and new azimuth association, (b) Azimuth association algorithm Flowchart

3.4.3 Experimental Results

3.4.3.1 Experimental Configuration

This thesis topic integrates LiDAR telemetry techniques for road network evaluation. The perception system, based on one LiDAR sensor (Velodyne VLP-16), is mounted on a moving vehicle or on a fixed stand, directed toward the ground by a high inclination angle as shown in Figure 3.6.

(a) VLP-16 LiDAR mounted on a vehicle (b) VLP-16 LiDAR mounted on a fixed stand

FIGURE 3.6: VLP-16 system

VLP-16 LiDAR sensor has several interesting properties for our application, mainly:

- 360° azimuth angular field of view.
- 30° elevation angular field of view.
- 0.2° azimuth angular resolution.
- Good accuracy of measurement ($\pm 3cm$).
- Relatively low cost.

A software, supplied by the manufacturer and named VeloView [139] is used for data acquisition in order to record, view and store the telemetric data in a packet capture *.pcap* file. Then, Wireshark software [140] permits to read the data from the .pcap file in hexadecimal format, and Matlab software [141] is used to extract the data from the *.pcap* file (Appendix A.2) and to process them.

3.4.3.2 Results

It is necessary to estimate the additive error in the data, that emerged after using the preprocessing step. The evaluation is composed by two cases, each case represents a new associated standard azimuth, sampled with azimuth angular resolution 0.2° while conserving the same number of azimuth angles in both cases. In the first standard case, the new associated azimuths α_{std1} is equal to $[0°, 359.8°]$. While in the second standard case, the new associated azimuths α_{std2} start from half the azimuth angular resolution and covers the range $[0.1°, 359.9°]$. In these two cases, the error induced by our preprocessing is computed below, and a conclusion is given on the interest of this step.

The error parameters of each preprocessing method are evaluated by using the old azimuth α_{old} and the new standard associated azimuths $\alpha_{std1}, \alpha_{std2}$, the old transverse x_{old} and the new associated transverses x_{std1}, x_{std2}, and the old longitude y_{old} and the new associated longitudes y_{std1}, y_{std2}, for all of a 50 sample frames' points in a given sequence, and are expressed in the equations below:

- The standard deviation $\sigma_{\alpha_{old}/\alpha_i}$ of the azimuth error, between the old azimuth α_{old} with respect to the first and second standard associated azimuths $\alpha_{std1}, \alpha_{std2}$.

  $$\sigma_{\alpha_{old}/\alpha_i} = \sqrt{\frac{1}{N}\sum((\alpha_{old} - \alpha_i) - (\overline{\alpha_{old} - \alpha_i}))^2} \tag{3.2}$$

  Where $i = \{std1, std2\}$ and N is the number of impact points.

- The standard deviation σ_{x_{old}/x_i} of the transverse error, between the old transverse x_{old} with respect to the new associated transverses x_{std1}, x_{std2}.

  $$\sigma_{x_{old}/x_i} = \sqrt{\frac{1}{N}\sum((x_{old} - x_i) - (\overline{x_{old} - x_i}))^2} \tag{3.3}$$

- The standard deviation σ_{y_{old}/y_i} of the longitude error, between the old longitude y_{old} with respect to the new associated longitudes y_{std1}, y_{std2}.

  $$\sigma_{y_{old}/y_i} = \sqrt{\frac{1}{N}\sum((y_{old} - y_i) - (\overline{y_{old} - y_i}))^2} \tag{3.4}$$

- The average associated points represents the percentage of the association points number M with respect to the total number N of impact points.

  $$Average\ associated\ points = \frac{M}{N} \times 100\% \tag{3.5}$$

Table 3.3 shows the standard deviations above on four different acquisitions. The first two acquisitions are downloaded from the Velodyne website [138] where the LiDAR sensor setup is with no orientation, while the second two acquisitions are recorded in the lab corridor and outdoor road by our LiDAR sensor where it is setup with a high orientation angle.

TABLE 3.3: Preprocessing azimuth association errors for four different acquisitions

Acquisition name	Frames number	$\sigma_{\alpha_{old}/\alpha_{std1}}$	$\sigma_{x_{old}/x_{std1}}$	$\sigma_{y_{old}/y_{std1}}$	Average associated points	$\sigma_{\alpha_{old}/\alpha_{std2}}$	$\sigma_{x_{old}/x_{std2}}$	$\sigma_{y_{old}/y_{std2}}$	Average associated points
Country Fair	50	0.0686°	0.0168	0.0134	98.57%	0.0649°	0.0160	0.0127	98.85%
Monterey Highway	50	0.0685°	0.0178	0.0201	98.68%	0.0643°	0.0166	0.0189	99.06%
ULCO Corridor	50	0.0696°	0.0013	0.0010	99.38%	0.0681°	0.0013	0.0010	99.27%
ULCO Outdoor	50	0.0696°	0.0015	0.0067	99.17%	0.0677°	0.0015	0.0067	99.11%

3.4.4 Results Discussion

The obtained azimuth errors $\sigma_{\alpha_{old}/\alpha_{std1}}, \sigma_{\alpha_{old}/\alpha_{std2}}$ in the two standard cases are very small and close to each other. In addition, the azimuth error's $\sigma_{\alpha_{old}/\alpha_i}$ effect on the transverse and longitude errors $\sigma_{x_{old}/x_i}, \sigma_{y_{old}/y_i}$ of our acquisition is widely smaller than the effect of Velodyne acquisitions, due to the orientation of our LiDAR sensor which leads to a decrease of the ranges of the impact points. After the analysis of Table 3.3 results, the second azimuth standard α_{std2} tends to be selected for two reasons. The first reason, is that the second azimuth standard error $\sigma_{\alpha_{old}/\alpha_{std2}}$ is slightly smaller than the first azimuth standard error $\sigma_{\alpha_{old}/\alpha_{std1}}$. The second reason, is that the second azimuth standard α_{std2} doesn't includes $0°, 90°, 180°, 270°, 360°$, which avoids the undetermined mathematical problem conditions in the next calibration and detection processes (for example $\tan \alpha_{std1}$ where $\alpha_{std1} = 90°$, is an undetermined case).

3.5 Conclusion

To summarize it up, the familiarity with an instrument sensor is an important initialization step to avoid several technical problems that may face it in any scientific subject. Therefore, this chapter addresses a brief explanation about Velodyne VLP-16 LiDAR features, an easy ways for data extraction from the LiDAR sensor export file, and a data preprocessing procedure in order to solve the problem of azimuth angular resolution from non-periodic into arithmetic sequence order, using frames separation and points association for a recommended standard, which provides a suitable prepared data for points selection at a specific azimuth that used later in Chapter 4.

Chapter 4

Extrinsic Calibration Method

4.1 Introduction

After introducing the preprocessing block, which expresses an arithmetic sequential order for the azimuth feature, this sequential order generates a periodic angular resolution. So that, we can benefit from this process to select a number of points at a specific azimuth as used later in the calibration process (section 4.3.3).

In general, calibration block part is an important process block in most applications using sensors. This calibration process has to be launched in a first time before the beginning of the processing, in order to deliver suitable data usable for the successive steps. In our system, the internal parameters of the LiDAR are supposed to be known and given by the manufacturer, so no intrinsic calibration is necessary, especially that the study environment region is the road, which is characterized by a close range values due to the downward orientation of the LiDAR sensor. Therefore, the calibration step considers only an extrinsic calibration method, that is explained in details in the next sections of this chapter.

4.2 LiDAR/Ground Geometrical Impact Modeling

In order to test our methods using 3D telemetric data and to study their robustness in presence of noise, it is necessary to form a plane-based model. The model is generated depending on the features of multi-laser rangefinder or 3D LiDAR sensor, where the environment impact points can be modeled as an intersection between the LiDAR laser beams and the environmental surrounding surfaces. In this work, the LiDAR sensor must be oriented toward the ground in order to study the road defects. Therefore, the LiDAR laser beams are represented as straight lines and the ground surface as a flat plane in a 3D frame.

Depending on the application situation, two concepts can represent the geometrical reflection model between the LiDAR sensor and the ground surface as shown in Figure 4.1:

- Practical orientation concept: the LiDAR laser beams (d) are supposed to be rotated and the ground's real plane (P_{re}) is a fixed horizontal plane as shown in Figure 4.1b.

- Scientific orientation concept: the LiDAR laser beams (d) are supposed to be fixed and the virtual horizontal ground surface (P_H) must be rotated by the LiDAR's inverse orientation in the practical concept, to get the real oblique ground plane (P_{re}) in LiDAR frame as shown in Figure 4.1c.

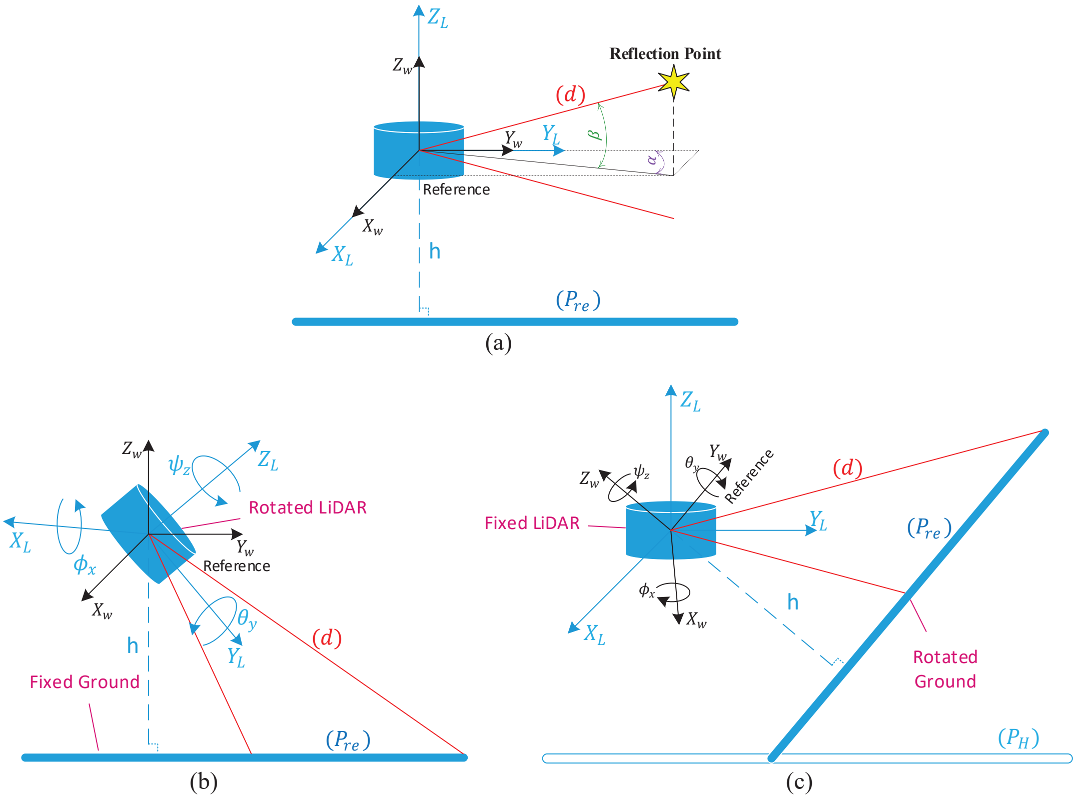

FIGURE 4.1: (a) No orientation, (b) Practical orientation concept, (c) Scientific orientation concept

4.2.1 Extrinsic Parameters vs Practical Concept

The research goal depends on the four extrinsic parameters (altitude and orientation angles), where the orientation parameter is the strongest influence factor on the ground points distribution process as shown in Figures 4.2a and 4.2b. The proposed calibration method must satisfy two contradictory conditions in relation to the final research objectives:

- Goal: plane-based extrinsic calibration, that needs large sparsity area to improve the plane estimation, which requires high altitude and low orientation angles.

- Constraint: the stated finality of road surface object detection, that needs high density points to improve the capability of detecting defect coverage points, which requires low altitude and high orientation angles.

Therefore, a trade-off is needed in order to optimize the extrinsic parameters (altitude and orientation angles), providing the suitable coverage points distribution over the ground.

Four geometric view patterns are summarized in three cases depending on the variation of pitch angle ϕ_x with respect to the LiDAR's vertical field of view "$vFOV$" as shown in Figure 4.2: (1) circles patterns (Figure 4.2c), (2) combination of ellipses, parabola and hyperbolas patterns (Figure 4.2d) and (3) hyperbolas patterns (Figure 4.2e).

The main objective of this thesis is road defect detection, which requires high coverage resolution. Therefore, the study case in this problem focuses on the hyperbolas case as shown in Figure 4.2e, in order to increase the points density on the ground.

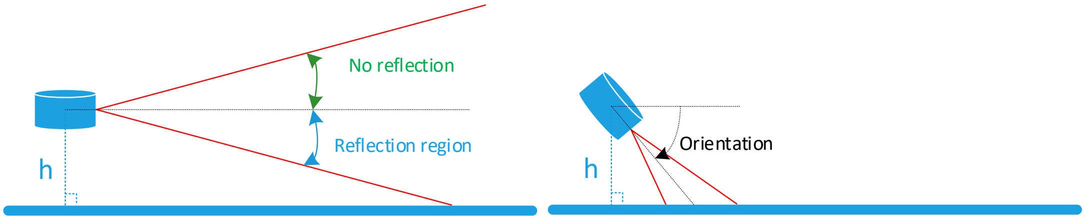

(a) No orientation (b) LiDAR orientation

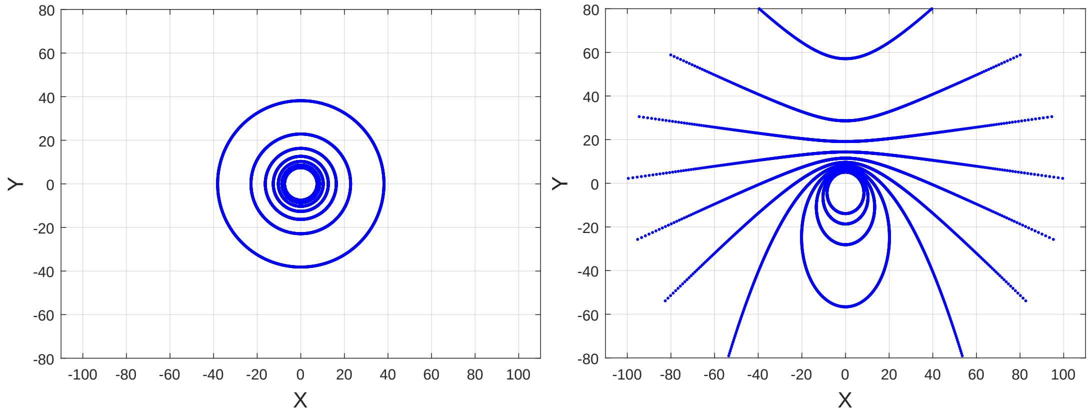

(c) No rotation $\phi_x = 0^\circ$ (d) $\phi_x < \frac{1}{2}vFOV$

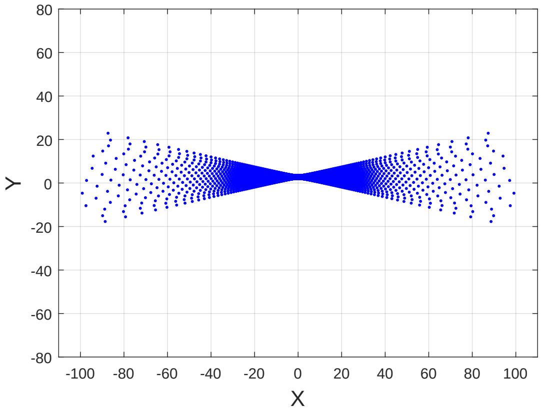

(e) $\phi_x > \frac{1}{2}vFOV$

FIGURE 4.2: Large sparsity area vs high density points

4.2.2 LiDAR Laser Beams and Oblique Ground Surface Intersection

In the following part, the scientific orientation concept was chosen to model the reflections of the laser beams (d) on the real oblique ground surface (P_{re}). Therefore, the LiDAR is supposed to be fixed and the parametric equations of the fixed straight lines (d) in LiDAR frame are given by:

$$(d) : \left\{ \begin{array}{l} \begin{bmatrix} x \\ y \\ z \end{bmatrix} = \begin{bmatrix} t \cdot \tan\alpha \\ t \\ t \cdot \sqrt{1+\tan^2\alpha} \cdot \tan\beta \end{bmatrix} \text{ for } \begin{cases} 0^\circ < \alpha < 90^\circ \text{ } or \\ 270^\circ < \alpha < 360^\circ \\ -15^\circ < \beta < 15^\circ \\ t \geq 0 \end{cases} \\ \begin{bmatrix} x \\ y \\ z \end{bmatrix} = \begin{bmatrix} t \cdot \tan\alpha \\ t \\ -t \cdot \sqrt{1+\tan^2\alpha} \cdot \tan\beta \end{bmatrix} \text{ for } \begin{cases} 90^\circ < \alpha < 270^\circ \\ -15^\circ < \beta < 15^\circ \\ t \leq 0 \end{cases} \end{array} \right. \tag{4.1}$$

Where α and β describe the azimuth and the elevation angles of each laser beam and t is the parameter of the parametric representation.

The virtual horizontal ground plane (P_H) must be rotated by the 3D Euler's angles ψ_z, θ_y, ϕ_x, so that the equation of the rotated real ground plane (P_{re}) is expressed as a function of the horizontal ground plane (P_H) with height h and rotational matrix $R_{z,y,x}(\psi_z, \theta_y, \phi_x)$.This transformation is expressed as:

$$P_{re} = R_{z,y,x}(\psi_z, \theta_y, \phi_x) P_H \tag{4.2}$$

The parametric and Cartesian equations of the horizontal ground plane (P_H) are expressed as follows:

$$(P_H) : \begin{cases} \begin{bmatrix} x \\ y \\ z \end{bmatrix} = \begin{bmatrix} t + aw \\ t + bw \\ -h \end{bmatrix} \text{ parametric equation } \quad \forall a, b \in \mathbb{R} \\ z + h = 0 \text{ Cartesian equation} \end{cases} \tag{4.3}$$

The rotational matrix $R_{z,y,x}(\psi_z, \theta_y, \phi_x)$ [142] is expressed as:

$$\begin{aligned} R_{z,y,x}(\psi_z, \theta_y, \phi_x) &= R_z(\psi_z) R_y(\theta_y) R_x(\phi_x) \\ &= \begin{bmatrix} \cos\psi_z \cos\theta_y & \begin{matrix} \cos\psi_z \sin\theta_y \sin\phi_x \\ -\sin\psi_z \cos\phi_x \end{matrix} & \begin{matrix} \cos\psi_z \sin\theta_y \cos\phi_x \\ +\sin\psi_z \sin\phi_x \end{matrix} \\ \sin\psi_z \cos\theta_y & \begin{matrix} \sin\psi_z \sin\theta_y \sin\phi_x \\ +\cos\psi_z \cos\phi_x \end{matrix} & \begin{matrix} \sin\psi_z \sin\theta_y \cos\phi_x \\ -\cos\psi_z \sin\phi_x \end{matrix} \\ -\sin\theta_y & \cos\theta_y \sin\phi_x & \cos\theta_y \cos\phi_x \end{bmatrix} \end{aligned} \tag{4.4}$$

Therefore, the Cartesian coordinates of the real points cloud c_{re} obtained from the intersection between the fixed straight lines (d) and the rotated real plane

(P_{re}) are expressed as:

$$(c_{re}) : \begin{cases} \begin{bmatrix} x \\ y \\ z \end{bmatrix} = \begin{bmatrix} t \cdot \tan\alpha \\ t \\ t \cdot \sqrt{1+\tan^2\alpha} \cdot \tan\beta \end{bmatrix} \text{ for } \begin{cases} 0^\circ < \alpha < 90^\circ \ or \\ 270^\circ < \alpha < 360^\circ \\ -15^\circ < \beta < 15^\circ \\ t \geq 0 \end{cases} \\ \forall t = \frac{(ul'-u'l)hk''+(u'k-uk')hl''+(lk'-l'k)hu''}{(k'l''-l'k'')\tan\alpha+(lk''-kl'')+(l'k-lk')\sqrt{1+\tan\alpha^2}\tan\beta} \\ \begin{bmatrix} x \\ y \\ z \end{bmatrix} = \begin{bmatrix} t \cdot \tan\alpha \\ t \\ -t \cdot \sqrt{1+\tan^2\alpha} \cdot \tan\beta \end{bmatrix} \text{ for } \begin{cases} 90^\circ < \alpha < 270^\circ \\ -15^\circ < \beta < 15^\circ \\ t \leq 0 \end{cases} \\ \forall t = \frac{(ul'-u'l)hk''+(u'k-uk')hl''+(lk'-l'k)hu''}{(k'l''-l'k'')\tan\alpha+(lk''-kl'')-(l'k-lk')\sqrt{1+\tan\alpha^2}\tan\beta} \end{cases} \tag{4.5}$$

Where:

$$\left.\begin{aligned} k &= \cos\psi_z\cos\theta_y + \cos\psi_z\sin\theta_y\sin\phi_x - \sin\psi_z\cos\phi_x \\ l &= a\cos\psi_z\cos\theta_y + b\cos\psi_z\sin\theta_y\sin\phi_x - b\sin\psi_z\cos\phi_x \\ u &= \cos\psi_z\sin\theta_y\cos\phi_x + \sin\psi_z\sin\phi_x \\ k' &= \sin\psi_z\cos\theta_y + \sin\psi_z\sin\theta_y\sin\phi_x + \cos\psi_z\cos\phi_x \\ l' &= a\sin\psi_z\cos\theta_y + b\sin\psi_z\sin\theta_y\sin\phi_x + b\cos\psi_z\cos\phi_x \\ u' &= \sin\psi_z\sin\theta_y\cos\phi_x + \cos\psi_z\sin\phi_x \\ k'' &= -\sin\theta_y + \cos\theta_y\sin\phi_x \\ l'' &= -a\sin\theta_y + b\cos\theta_y\sin\phi_x \\ u'' &= \cos\theta_y\cos\phi_x \end{aligned}\right\} \forall a,b \in \mathbb{R} \tag{4.6}$$

4.2.3 Error Modeling in Polar and Cartesian Coordinates

In this section, the systematic and random errors $w_\rho, w_\alpha, w_\beta$ were taken in consideration as a source of error [85], [143], to represent the modeling of the additive white Gaussian noise for each polar coordinates ρ, α, β of the real points cloud c_{re} in Equation 4.7, where $\rho_w, \alpha_w, \beta_w$ are the real measurements of the range ρ, azimuth α and elevation β respectively for each reflecting point.

$$(c_w) : \begin{bmatrix} \rho_w \\ \alpha_w \\ \beta_w \end{bmatrix} = \begin{bmatrix} \rho + w_\rho \\ \alpha + w_\alpha \\ \beta + w_\beta \end{bmatrix} \tag{4.7}$$

The 3D transformation from polar coordinates $\rho_w, \alpha_w, \beta_w$ to Cartesian coordinates x_w, y_w, z_w of the ground noisy points cloud c_w is given by:

$$(c_w) : \begin{bmatrix} x_w \\ y_w \\ z_w \end{bmatrix} = \begin{bmatrix} \rho_w\cos\beta_w\sin\alpha_w \\ \rho_w\cos\beta_w\cos\alpha_w \\ \rho_w\sin\beta_w \end{bmatrix} \tag{4.8}$$

Then the standard deviation of the error can be derived from polar to Cartesian parameters in Equation 4.9, assuming that $\sigma_{x_w}, \sigma_{y_w}, \sigma_{z_w}, \sigma_{\rho_w}, \sigma_{\alpha_w}, \sigma_{\beta_w}$ are respectively the standard deviations of the added noise on $x_w, y_w, z_w, \rho_w, \alpha_w, \beta_w$. The terms of the standard deviations $\sigma_{\rho_w}, \sigma_{\alpha_w}, \sigma_{\beta_w}$ with a power higher than two can be neglected in this derivation to obtain this approximation:

$$\begin{bmatrix} \sigma^2_{x_w} \\ \sigma^2_{y_w} \\ \sigma^2_{z_w} \end{bmatrix} \simeq \begin{bmatrix} \sigma^2_{\rho_w} \cos^2\beta_w \sin^2\alpha_w + \rho^2_w(\sigma^2_{\beta_w} \sin^2\beta_w \sin^2\alpha_w + \sigma^2_{\alpha_w} \cos^2\beta_w \cos^2\alpha_w) \\ \sigma^2_{\rho_w} \cos^2\beta_w \cos^2\alpha_w + \rho^2_w(\sigma^2_{\beta_w} \sin^2\beta_w \cos^2\alpha_w + \sigma^2_{\alpha_w} \cos^2\beta_w \sin^2\alpha_w) \\ \sigma^2_{\rho_w} \sin^2\beta_w + \rho^2_w \sigma^2_{\beta_w} \cos^2\beta_w \end{bmatrix} \tag{4.9}$$

Remark: Glennie et al. [82] have shown in particular that the error of a scanning LiDAR sensor is mainly manifested over range. In this type of sensor, angles are not directly measured, but the error is mainly related to the reproducibility of the measurement for a given angle. The hypothesis of neglecting the scanning angle error is a very common assumption in the field of LiDAR detection: it is part of the manufacturers' specifications and is commonly used in the literature. This is particularly related to the very small influence of the angle reproducibility errors on the range measurement of the object of interest.

In this study, we then focus on the range error σ_{ρ_w} and neglect the azimuth and elevation errors $\sigma_{\alpha_w}, \sigma_{\beta_w}$ respectively in the simulation data as given by the constructor. The transformation in Equation 4.9 is then simplified as:

$$\begin{bmatrix} \sigma_{x_w} \\ \sigma_{y_w} \\ \sigma_{z_w} \end{bmatrix} = \begin{bmatrix} \sigma_{\rho_w} \cos\beta_w \sin\alpha_w \\ \sigma_{\rho_w} \cos\beta_w \cos\alpha_w \\ \sigma_{\rho_w} \sin\beta_w \end{bmatrix} \tag{4.10}$$

4.3 Extrinsic LiDAR/Ground Calibration Method

In multi-sensor applications, data acquired from the different sensors must be fused in one common reference frame. In this application, the calibration of LiDAR frame scans is necessary to merge them in one world reference frame, in order to increase the points density coverage on the ground, which facilitates the road defect detection. Therefore, the extrinsic calibration aims to model the relationship between the LiDAR frame and the world reference frame.

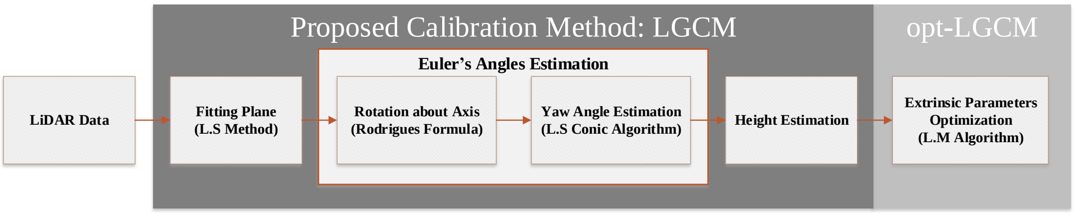

FIGURE 4.3: The proposed extrinsic calibration method block diagram

Thus, we propose a new method called LiDAR/Ground Calibration Method (LGCM) presented in Figure 4.3. The method includes the following procedures: fitting the ground plane by Least Squares estimator, rotation about axis by Rodrigues formula and Least Squares Conic Algorithm for Euler's angles estimation, and then height estimation. The proposed method is supplemented by Levenberg-Marquardt optimization algorithm as (opt-LGCM).

The main role of LGCM procedure is to estimate the extrinsic parameters: the Euler's rotational angles ψ_z, θ_y, ϕ_x and the height h. The opt-LGCM is initialized by the estimated extrinsic parameters to optimize them. Finally, the distributed ground noisy points c_w along the real plane (P_{re}) are rotated along the horizontal plane (P_H) by the optimized extrinsic parameters in the frame of fixed LiDAR.

The proposed method consists mainly in two steps. A first, totally unsupervised step, which consists in estimating a first value of the steering angles. This first estimate is then used as a basis for the optimization step which will seek the best orientation parameters. The proposed method is therefore totally unsupervised and does not require *a priori* knowledge of the orientation of the sensor by a pan/tilt unit for example [144].

4.3.1 Fitting Plane

The first step aims to fit an estimated plane (P_{est}) with the rotated ground noisy points c_w. The Least Squares estimator is used to obtain the normal vector of the plane (P_{est}).

The equation of the estimated plane (P_{est}) in the LiDAR frame is expressed by:

$$f(x,y) = z = Ax + By + D + w \tag{4.11}$$

Where A,B, and D are the plane parameters, and w is an additive white Gaussian noise with standard deviation σ_w.

Therefore, Equation 4.11 of the estimated plane (P_{est}) can be written in linear form as:

$$Z = H\Theta + w \tag{4.12}$$

Where:

$$Z = \begin{bmatrix} z(0) & \cdots & z(N-1) \end{bmatrix}^T$$

$$H = \begin{bmatrix} x(0) & y(0) & 1 \\ \vdots & \vdots & \vdots \\ x(N-1) & y(N-1) & 1 \end{bmatrix}$$

$$\Theta = \begin{bmatrix} A & B & D \end{bmatrix}^T$$

$w = \begin{bmatrix} w(0) & \cdots & w(N-1) \end{bmatrix}^T$ where N is the number of reflected points.

The solution of Least Squares estimator for this linear model [145] is expressed as:

$$\hat{\Theta}_{LS} = (H^T H)^{-1} H^T Z \tag{4.13}$$

4.3.2 Rotation about Axis

Rodrigues formula is an efficient rotation transformation that computes the rotation matrix R_{rod}, which rotates a vector into another vector in 3D frame around a fixed axis vector $\overrightarrow{Axis}$ by rotational angle η [146]. Therefore, after having estimated the parameter vector of the oblique estimated plane (P_{est}) in the previous section 4.3.1, the next step is to compute the rotational matrix R_{rod} from the normal vector $\overrightarrow{n}_1$ of the oblique estimated plane (P_{est}) to the normal vector $\overrightarrow{n}_2$ of the horizontal plane (P_H) that is parallel to $X_L Y_L$-plane with height $-h$ (*cf*. Figure 4.1c). The objective of this step is to use Rodrigues formula in order to estimate the first two Euler's angles pitch $\hat{\phi}_x$, roll $\hat{\theta}_y$, and the first partial yaw angle $\hat{\Psi}_{z1}$ -due to the incomplete calibration in yaw rotation, which is solved by the next step- from Rodrigues Matrix R_{rod}.

Assuming that $\overrightarrow{n}_1$, $\overrightarrow{n}_2$ and $\overrightarrow{Axis}$ are expressed as:

$\overrightarrow{n}_1(-\hat{A}, -\hat{B}, 1)$

$\overrightarrow{n}_2(0, 0, 1)$

$\overrightarrow{Axis}(m, n, p) = \frac{\overrightarrow{n}_1 \times \overrightarrow{n}_2}{\|\overrightarrow{n}_1 \times \overrightarrow{n}_2\|}$

The Rodrigues rotation formula R_{rod} can be then written as:

$$R_{rod} = I_3 + \sin\eta K + (1 - \cos\eta K^2) \tag{4.14}$$

Where:

$$I_3 = \begin{bmatrix} 1 & 0 & 0 \\ 0 & 1 & 0 \\ 0 & 0 & 1 \end{bmatrix}$$

$$K = \begin{bmatrix} 0 & -p & n \\ p & 0 & -m \\ -n & m & 0 \end{bmatrix}$$

$\sin\eta = \frac{\|\overrightarrow{n}_1 \times \overrightarrow{n}_2\|}{\|\overrightarrow{n}_1\| \cdot \|\overrightarrow{n}_2\|}$

$\cos\eta = \frac{\overrightarrow{n}_1 \cdot \overrightarrow{n}_2}{\|\overrightarrow{n}_1\| \cdot \|\overrightarrow{n}_2\|}$

Now, by using Equation 4.15 below:

$$R_{rod} = R_{x,y,z}(\hat{\Psi}_{z1}, \hat{\theta}_y, \hat{\phi}_x) = R_x(\hat{\Psi}_{z1}) R_y(\hat{\theta}_y) R_z(\hat{\phi}_x) \tag{4.15}$$

Then, the Rodrigues matrix R_{rod} provides the computation of $\hat{\Psi}_{z1}$, $\hat{\theta}_y$, and $\hat{\phi}_x$ as expressed in the equations below:

$$\hat{\Psi}_{z1} = \arctan\left((R_{rod})_{21}/(R_{rod})_{11}\right) \tag{4.16}$$

$$\hat{\theta}_y = \arcsin(-(R_{rod})_{31}) \tag{4.17}$$

$$\hat{\phi}_x = \arctan\left((R_{rod})_{32}/(R_{rod})_{33}\right) \tag{4.18}$$

Where ij represents the matrix element index of $(R_{rod})_{ij}$. As a graphical result, the ground noisy points c_w are rotated by Rodrigues matrix R_{rod} to the distributed points c_{H1} along the horizontal plane (P_H) by Equation 4.19 as shown in Figure 4.4.

$$c_{H1} = R_{rod} c_w \tag{4.19}$$

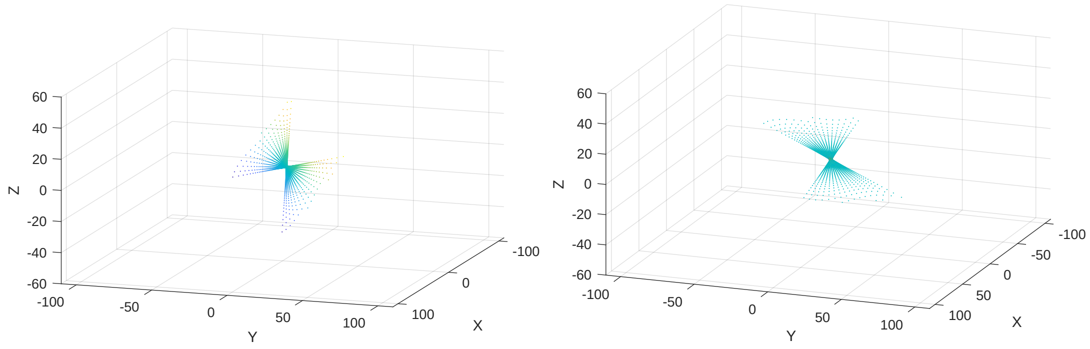

(a) (b)

FIGURE 4.4: (a) distributed ground noisy points c_w about the real plane (P_{re}), (b) distributed points c_{H1} along the horizontal plane (P_H)

4.3.3 Yaw Angle Estimation

After rotating the noisy points c_w to the horizontal points c_{H1}, the second partial yaw angle $\hat{\Psi}_{z2}$ is estimated by an efficient Algorithm 1 that we proposes in Figure 4.5 to rotate the points c_{H1} to c_{H2} about z-axis. This algorithm is called Least Squares Conic Algorithm LSCA which takes an advantage of the center S characteristic of the geometrical impact patterns (hyperbolas, parabolas, circles) formed by the points c_{H1} as shown in Figure 4.5. The aim of this part is to compute yaw angle $\hat{\psi}_z$ from the partial angles $\hat{\Psi}_{z1}$ and $\hat{\Psi}_{z2}$ as shown in Equation 4.20.

Algorithm 1: Least Squares Conic Algorithm

```
Input: $x$,$y$,$z$,$\alpha$,$\beta$ of the distributed points $c_{H1}$
Output: $\hat{\Psi}_{z2}$
Fit the lines $(l)$ and $(l')$ that pass through the points at each $\zeta = 10°$ consecutive azimuth by Least Squares estimator.
    The solution of Least Squares estimator for linear model:
    $\hat{\Theta}_{LS} = (H^T H)^{-1} H^T Y$ where $Y = \begin{bmatrix} y(0) \\ \vdots \\ y(N-1) \end{bmatrix}$, $H = \begin{bmatrix} x(0) & 1 \\ \vdots & \vdots \\ x(N-1) & 1 \end{bmatrix}$,
    $\hat{\Theta}_{LS} = \begin{bmatrix} \hat{m} \\ \hat{b} \end{bmatrix}$
Compute the coordinates of the intersection points $S$ of each two symmetric lines of $(l)$ and $(l')$.
    Assume that:
    $(l) : y = \hat{m}_1 x + \hat{b}_1$
    $(l') : y = \hat{m}_2 x + \hat{b}_2$
    Therefore, the intersection points $S$ of the straight lines $(l)$ and $(l')$ are computed as follows:
    $x_S = \frac{\hat{b}_2 - \hat{b}_1}{\hat{m}_1 - \hat{m}_2}$,$y_S = \hat{m}_1 \frac{\hat{b}_2 - \hat{b}_1}{\hat{m}_1 - \hat{m}_2} + \hat{b}_1$
Fit a line $(v)$ that passes through the intersection points $S$ and the origin $O$ by Least Squares estimator.
    The solution of Least Squares estimator:
    $\hat{\Theta}_{LS} = (H^T H)^{-1} H^T Y$ where $Y = \begin{bmatrix} y(0) \\ \vdots \\ y(N-1) \end{bmatrix}$, $H = \begin{bmatrix} x(0) \\ \vdots \\ x(N-1) \end{bmatrix}$,
    $\hat{\Theta}_{LS} = \begin{bmatrix} \hat{m} \end{bmatrix}$
Finally, compute the angle $\hat{\Psi}_{z2}$ formed by the fitting line $(v)$ and $y$-axis:
    $\hat{\Psi}_{z2} = \arctan \hat{m} - 90°$ if $\hat{m} > 0$
    $\hat{\Psi}_{z2} = \arctan \hat{m} + 90°$ if $\hat{m} < 0$
```

Therefore, the third Euler's angle of rotation (yaw angle) $\hat{\psi}_z$ is computed as follows:

$$\hat{\psi}_z = \hat{\Psi}_{z1} - \hat{\Psi}_{z2} \tag{4.20}$$

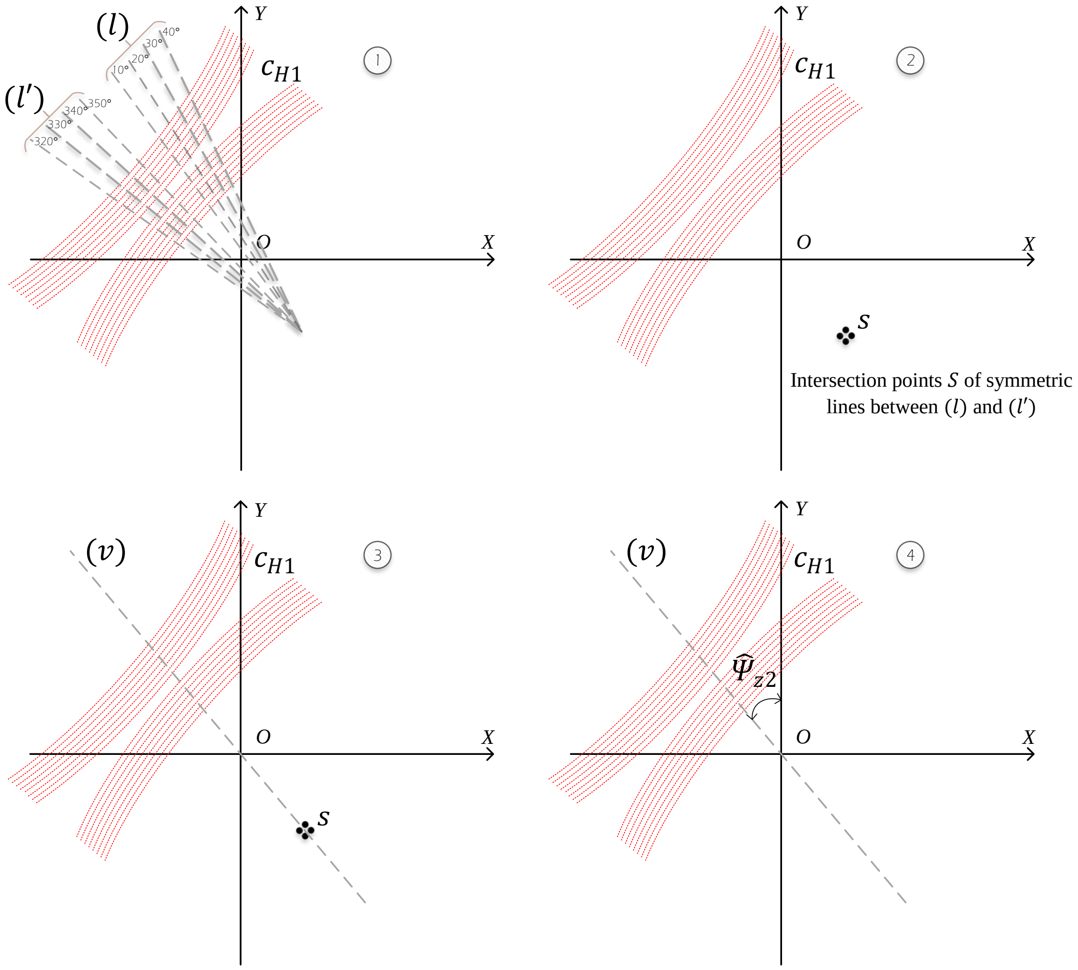

FIGURE 4.5: (1) fitting the lines passing through the points of each $\zeta = 10°$ consecutive azimuth, (2) intersection points S of each symmetric lines between (l) and (l'), (3) fitting line (v) that passes through the points S and the origin O, (4) angle $\hat{\Psi}_{z2}$ formed by line (v) and y-axis

Finally, the points c_{H1} are rotated to points c_{H2} by an angle $-\hat{\Psi}_{z2}$ around z-axis as shown in Figure 4.6.

$$c_{H2} = R_z(-\hat{\Psi}_{z2})c_{H1} \tag{4.21}$$

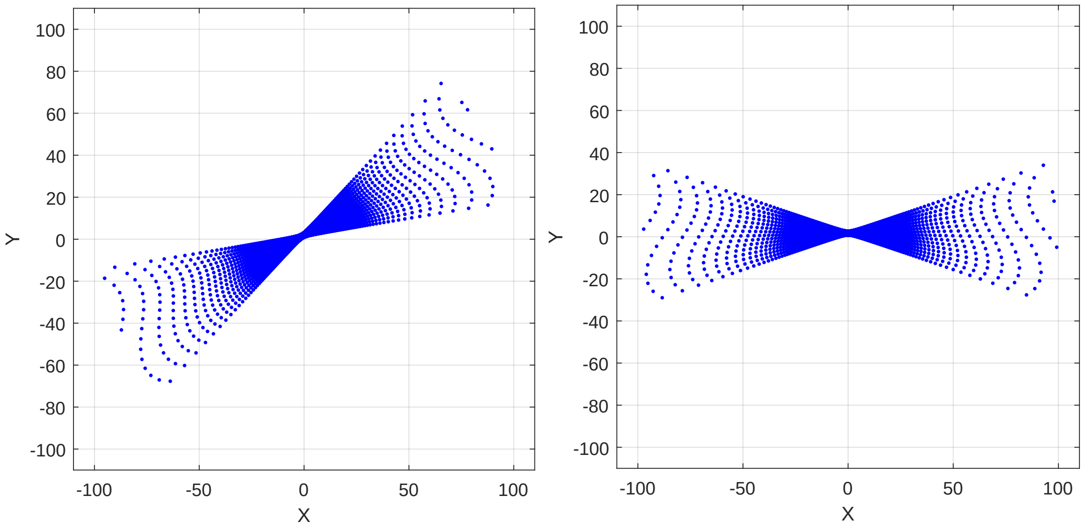

(a) (b)

FIGURE 4.6: (a) points c_{H1} before LSCA, (b) points c_{H2} after LSCA rotated by $\hat{\Psi}_{z2}$ about z-axis

4.3.4 Height Estimation

At the end of LGCM approach, a suitable way to estimate the height is to compute the altitude mean of the points c_{H2}, due to the ground geometrical model used in this paper. Therefore, the estimated height is then expressed as:

$$\hat{h} = \frac{1}{N}\sum_{i=0}^{N-1} z_i \text{ where } N \text{ is the number of calibrated points} \tag{4.22}$$

4.3.5 Extrinsic Parameters Optimization

The role of optimized LiDAR/Ground Calibration Method opt-LGCM is to optimize the extrinsic parameters $\psi_z, \theta_y, \phi_x, h$ in order to obtain an optimized plane represents the ground. Therefore, Levenberg-Marquardt algorithm is an optimization algorithm, which combines both Gradient-Descent and Gauss-Newton methods [147]. In addition, it is a very efficient technique to find the minima and it performs well on most non-linear functions. The Levenberg-Marquardt algorithm is initialized by the estimated extrinsic parameters $\hat{\psi}_z, \hat{\theta}_y, \hat{\phi}_x, \hat{h}$ to obtain the optimized extrinsic parameters $\hat{\psi}''_z, \hat{\theta}''_y, \hat{\phi}''_x, \hat{h}_{opt}$, in order to minimize the mean square error mse that represents the square difference between the position of noisy points c_w and the optimized position of points c_{opt} in Equation 4.24. The optimized points c_{opt} represent the intersection between all the LiDAR beams (d) and the optimized plane (P_{opt})

which is the rotation of the horizontal plane (P_H) by the new optimized Euler's angles $\hat{\psi}''_z, \hat{\theta}''_y, \hat{\phi}''_x$ and the optimized height $\hat{h}_{opt}$ in Equation 4.25. In other words, the importance of the above procedure is to get the optimized height $\hat{h}_{opt}$ and the optimized Euler's angles $\hat{\psi}''_z, \hat{\theta}''_y, \hat{\phi}''_x$ that rotate, in the inverse ordering orientation, the horizontal plane (P_H), to fit the noisy points c_w that are distributed along the oblique real plane (P_{re}) with minimum mse on the position.

$$(\hat{\psi}''_z, \hat{\theta}''_y, \hat{\phi}''_x, \hat{h}_{opt}) = \underset{(\psi_z, \theta_y, \phi_x, h)}{\arg\min}\, mse \tag{4.23}$$

Where the non-linear function mse is expressed by:

$$mse = \frac{1}{m}\sum_{i=1}^{m}\left((x_{c_{opt}} - x_{c_w})^2 + (y_{c_{opt}} - y_{c_w})^2 + (z_{c_{opt}} - z_{c_w})^2 \right) \tag{4.24}$$

The optimized points c_{opt} represent the intersection between the straight lines (d) and the rotated optimized plane (P_{opt}), where the plane (P_{opt}) is the rotation of the fixed ground horizontal plane (P_H) of height $\hat{h}_{opt}$ by $-\hat{\psi}''_z, -\hat{\theta}''_y, -\hat{\phi}''_x$ based on $R_{x,y,z}$ rotation matrix as shown in Equation 4.25:

$$P_{opt} = R_{x,y,z}(-\hat{\psi}''_z, -\hat{\theta}''_y, -\hat{\phi}''_x) P_H \tag{4.25}$$

Where the rotation matrix $R_{x,y,z}$ is the reverse of $R_{z,y,x}$.

$$\begin{aligned} R_{x,y,z}(-\hat{\psi}''_z, -\hat{\theta}''_y, -\hat{\phi}''_x) &= R_x(-\hat{\phi}''_x) R_y(-\hat{\theta}''_y) R_z(-\hat{\psi}''_x) \\ &= \begin{bmatrix} \cos\hat{\psi}''_x \cos\hat{\theta}''_y & \sin\hat{\psi}''_x \cos\hat{\theta}''_y & -\sin\hat{\theta}''_y \\ \begin{matrix}\cos\hat{\psi}''_x \sin\hat{\theta}''_y \sin\hat{\phi}''_x \\ -\sin\hat{\psi}''_x \cos\hat{\phi}''_x\end{matrix} & \begin{matrix}\sin\hat{\psi}''_x \sin\hat{\theta}''_y \sin\hat{\phi}''_x \\ +\cos\hat{\psi}''_x \cos\hat{\phi}''_x\end{matrix} & \cos\hat{\theta}''_y \sin\hat{\phi}''_x \\ \begin{matrix}\cos\hat{\psi}''_x \sin\hat{\theta}''_y \cos\hat{\phi}''_x \\ +\sin\hat{\psi}''_x \sin\hat{\phi}''_x\end{matrix} & \begin{matrix}\sin\hat{\psi}''_x \sin\hat{\theta}''_y \cos\hat{\phi}''_x \\ -\cos\hat{\psi}''_x \sin\hat{\phi}''_x\end{matrix} & \cos\hat{\theta}''_y \cos\hat{\phi}''_x \end{bmatrix} \end{aligned} \tag{4.26}$$

Finally, the Cartesian coordinates of rotated optimized points cloud c_{opt} in the reverse orientation sense are estimated by $\hat{\psi}''_z, \hat{\theta}''_y, \hat{\phi}''_x, \hat{h}_{opt}$ as expressed below:

$$(c_{opt}) : \begin{cases} \begin{bmatrix} x \\ y \\ z \end{bmatrix} = \begin{bmatrix} t \cdot \tan\alpha \\ t \\ t \cdot \sqrt{1 + \tan^2\alpha} \cdot \tan\beta \end{bmatrix} \text{ for } \begin{cases} 0^\circ < \alpha < 90^\circ \; or \\ 270^\circ < \alpha < 360^\circ \\ -15^\circ < \beta < 15^\circ \\ t \geq 0 \end{cases} \\ \forall t = \frac{(ul' - u'l)\hat{h}_{opt}k'' + (u'k - uk')\hat{h}_{opt}l'' + (lk' - l'k)\hat{h}_{opt}u''}{(k'l'' - l'k'')\tan\alpha + (lk'' - kl'') + (l'k - lk')\sqrt{1 + \tan\alpha^2}\tan\beta} \\ \begin{bmatrix} x \\ y \\ z \end{bmatrix} = \begin{bmatrix} t \cdot \tan\alpha \\ t \\ -t \cdot \sqrt{1 + \tan^2\alpha} \cdot \tan\beta \end{bmatrix} \text{ for } \begin{cases} 90^\circ < \alpha < 270^\circ \\ -15^\circ < \beta < 15^\circ \\ t \leq 0 \end{cases} \\ \forall t = \frac{(ul' - u'l)\hat{h}_{opt}k'' + (u'k - uk')\hat{h}_{opt}l'' + (lk' - l'k)\hat{h}_{opt}u''}{(k'l'' - l'k'')\tan\alpha + (lk'' - kl'') - (l'k - lk')\sqrt{1 + \tan\alpha^2}\tan\beta} \end{cases} \tag{4.27}$$

Where:

$$\left.\begin{aligned}
k &= \cos\hat{\psi}''_z \cos\hat{\theta}''_y + \sin\hat{\psi}''_z \cos\hat{\theta}''_y \\
l &= a\cos\hat{\psi}''_z \cos\hat{\theta}''_y + b\sin\hat{\psi}''_z \cos\hat{\theta}''_y \\
u &= -\sin\hat{\theta}''_y \\
k' &= -\sin\hat{\psi}''_z \cos\hat{\phi}''_x + \cos\hat{\psi}''_z \sin\hat{\theta}''_y \sin\hat{\phi}''_x + \cos\hat{\psi}''_z \cos\hat{\phi}''_x + \sin\hat{\psi}''_z \sin\hat{\theta}''_y \sin\hat{\phi}''_x \\
l' &= -a\sin\hat{\psi}''_z \cos\hat{\phi}''_x + a\cos\hat{\psi}''_z \sin\hat{\theta}''_y \sin\hat{\phi}''_x + b\cos\hat{\psi}''_z \cos\hat{\phi}''_x + b\sin\hat{\psi}''_z \sin\hat{\theta}''_y \sin\hat{\phi}''_x \\
u' &= \cos\hat{\theta}''_y \sin\hat{\phi}''_x \\
k'' &= \sin\hat{\psi}''_z \sin\hat{\phi}''_x + \cos\hat{\psi}''_z \sin\hat{\theta}''_y \cos\hat{\phi}''_x - \cos\hat{\psi}''_z \sin\hat{\phi}''_x + \sin\hat{\psi}''_z \sin\hat{\theta}''_y \cos\hat{\phi}''_x \\
l'' &= a\sin\hat{\psi}''_z \sin\hat{\phi}''_x + a\cos\hat{\psi}''_z \sin\hat{\theta}''_y \cos\hat{\phi}''_x - b\cos\hat{\psi}''_z \sin\hat{\phi}''_x + b\sin\hat{\psi}''_z \sin\hat{\theta}''_y \cos\hat{\phi}''_x \\
u'' &= \cos\hat{\theta}''_y \cos\hat{\phi}''_x
\end{aligned}\right\} \forall a, b \in \mathbb{R} \qquad (4.28)$$

4.4 Experimental Results

In this section, the proposed calibration method LGCM is applied on two types of data: simulation data obtained by the modeling as mentioned in the sections 4.2.2 and 4.2.3, and real data acquisition from the Velodyne VLP-16 LiDAR. The most important features of Velodyne VLP-16 LiDAR are shown in Table 4.1.

TABLE 4.1: VLP-16 Features

Features	VLP-16
Laser beams	16
Horizontal FOV	360°
Vertical FOV	$-15° \rightarrow +15°$
Azimuth angular resolution	0.1° - 0.2° - 0.4°
Elevation angular resolution	2°
Range accuracy σ_ρ	$3cm$

The extrinsic calibration results are presented in terms of precision and robustness. According to our application, the precision shows the stability of the method with respect to the variation of: pitch angle ϕ_x toward the ground, and height h above the ground. While the robustness shows the method strength with respect to the variation of range accuracy σ_ρ of the measurements.

Therefore, the evaluation parameters of the results will focus on the point cloud features of the real points c_{re} on the real plane (P_{re}), noisy points c_w distributed along the real plane (P_{re}), estimated points c_{est} on the estimated plane (P_{est}) obtained by LGCM and the optimized points c_{opt} on the optimized plane (P_{opt}) obtained by opt-LGCM as described below:

- The real height h, estimated height $\hat{h}$ and the optimized height $\hat{h}_{opt}$.
- The standard deviation $\sigma_{d_{w/i}}$ of the noisy points c_w orthogonal Euclidean distance with respect to the real plane (P_{re}), the estimated plane (P_{est})

and the optimized plane (P_{opt}).

$$\sigma_{d_{w/i}} = \sqrt{\frac{1}{N}\sum(d_{w/i} - \overline{d_{w/i}})^2} \tag{4.29}$$

$$d_{w/i} = \frac{|A_i x_w + B_i y_w + C_i z_w + D_i|}{\sqrt{A_i^2 + B_i^2 + C_i^2}} \tag{4.30}$$

Where x_w, y_w, z_w are the Cartesian coordinates of the noisy points c_w, A_i, B_i, C_i, D_i are the coefficient parameters of the planes, $i = \{re, est, opt\}$ and N is the number of impact points.

- The standard deviation $\sigma_{\rho_{re}/\rho_i}$ of the real points c_{re} range difference with respect to the noisy points c_w, the estimated points c_{est} and the optimized points c_{opt}.

$$\sigma_{\rho_{re}/\rho_i} = \sqrt{\frac{1}{N}\sum((\rho_{re} - \rho_i) - (\overline{\rho_{re} - \rho_i}))^2} \tag{4.31}$$

Where $i = \{w, est, opt\}$ and N is the number of impact points.

- The standard deviation σ_{ρ_w/ρ_i} of the noisy points c_w range difference with respect to the real points c_{re}, the estimated points c_{est} and the optimized points c_{opt}.

$$\sigma_{\rho_w/\rho_i} = \sqrt{\frac{1}{N}\sum((\rho_w - \rho_i) - (\overline{\rho_w - \rho_i}))^2} \tag{4.32}$$

Where $i = \{re, est, opt\}$ and N is the number of impact points.

- The gain in performance PF_i that describes the range accuracy enhancement obtained from the Levenberg-Marquardt optimization algorithm which is defined as:

$$PF_i = \sigma_{\rho_w/\rho_i} - \sigma_{\rho_w/\rho_{re}} \tag{4.33}$$

Where $\sigma_{\rho_w/\rho_{re}}$ is the LiDAR range accuracy and $i = \{est, opt\}$.

4.4.1 Simulation Data Results

Using the simulation data, the setups used to validate the proposed calibration method are separated in two categories:

- In terms of precision, the real height $h = 2m$, roll angle $\theta_y = 2°$, yaw angle $\psi_z = 2°$ and LiDAR range accuracy $\sigma_{\rho_w/\rho_{re}} = 0.03m$, with respect to the variation of pitch angle $\phi_x = [-70°, 70°]$.
- In terms of precision, the pitch angle $\phi_x = 45°$, roll angle $\theta_y = 2°$, yaw angle $\psi_z = 2°$ and LiDAR range accuracy $\sigma_{\rho_w/\rho_{re}} = 0.03m$, with respect to the variation of height $h = [0.5m, 4.8m]$.

- In terms of robustness, the real height $h = 2m$, pitch angle $\phi_x = 45^\circ$, roll angle $\theta_y = 2^\circ$ and yaw angle $\psi_z = 2^\circ$, with respect to the variation of $\sigma_{\rho_w/\rho_{re}} = [0, 0.095m]$.

4.4.1.1 Standard Deviation $\sigma_{d_{w/i}}$ in Terms of Precision and Robustness

Referring to Figure 4.7a, the increasing of standard deviation $\sigma_{d_{w/i}}$ along the planes is due to the orientation effect of the LiDAR by the pitch angle ϕ_x on $\sigma_{d_{w/i}}$. So as pitch angle ϕ_x tends to 90°, the standard deviation $\sigma_{d_{w/i}}$ tends to the LiDAR range accuracy $\sigma_{\rho_w/\rho_{re}}$. Where in Figure 4.7c, the increasing of the standard deviation $\sigma_{d_{w/i}}$ is due to increasing of LiDAR range accuracy $\sigma_{\rho_w/\rho_{re}}$. Moreover, Equation 4.34 describes the relation of $\sigma_{d_{w/i}}$ with ϕ_x and $\sigma_{\rho_w/\rho_{re}}$ which proves the increasing of $\sigma_{d_{w/i}}$. While, Figure 4.7b shows that there is no correlation effect between the height h and the standard deviation $\sigma_{d_{w/i}}$.

$$\sigma_{d_{w/i}} = \sin\left(\phi_x + \varphi_k\right)\sigma_{\rho_w/\rho_{re}} \tag{4.34}$$

Where φ_k is the elevation angle of each VLP-16 LiDAR laser, and $k = \{1, 2, ..., 16\}$ represents the laser index.

In Figures 4.7d,4.7e and 4.7f, we can see that the standard deviation $\sigma_{d_{w/opt}}$ is closer to the the standard deviation $\sigma_{d_{w/re}}$ than the standard deviation $\sigma_{d_{w/est}}$. This shows that the optimized plane (P_{opt}) is better fit to the real plane (P_{re}) than the estimated plane (P_{est}).

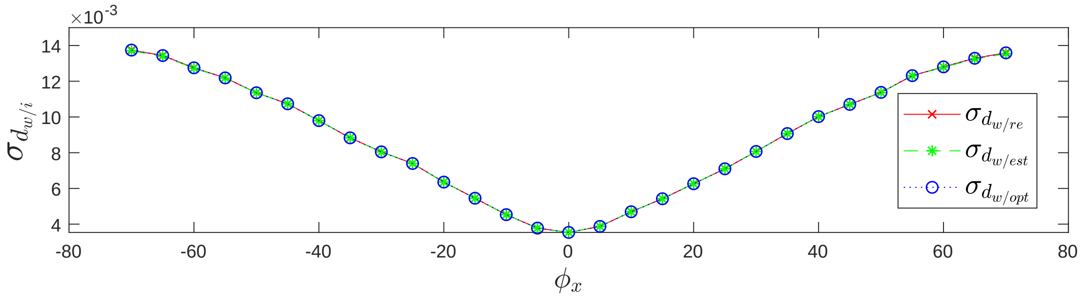

(a) variation of $\sigma_{d_{w/i}}$ with respect to ϕ_x

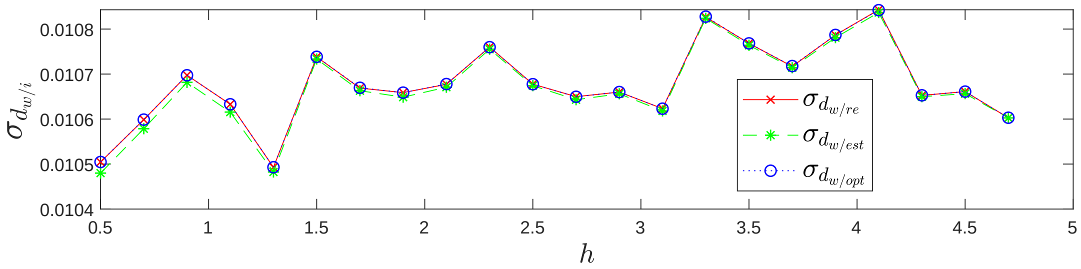

(b) variation of $\sigma_{d_{w/i}}$ with respect to h

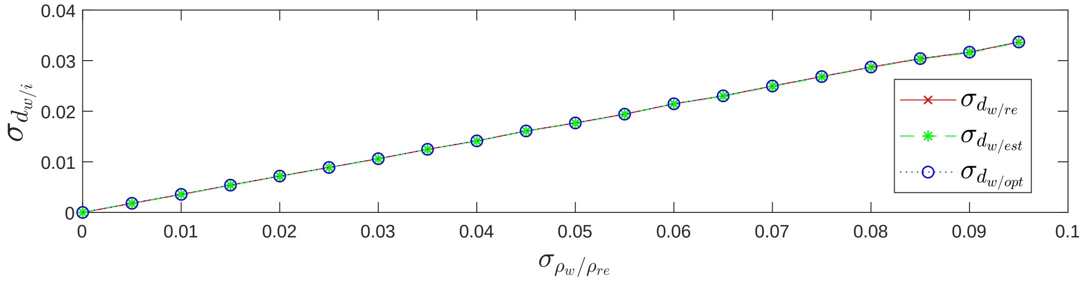

(c) variation of $\sigma_{d_{w/i}}$ with respect to $\sigma_{\rho_w/\rho_{re}}$

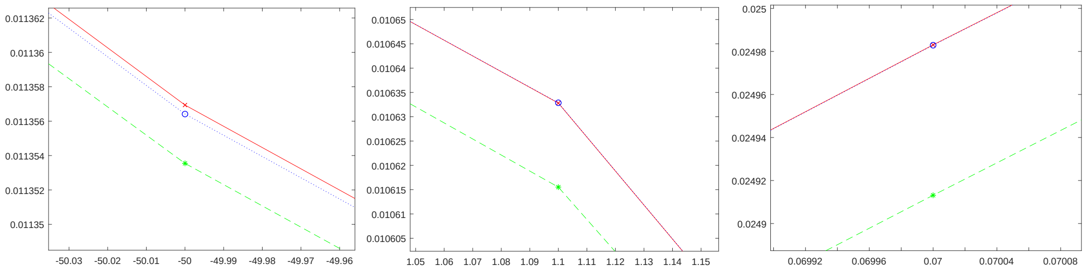

(d) zoom in (a) at $\phi_x = -50°$ (e) zoom in (b) at $h = 1.1$ (f) zoom in (c) at $\sigma_{\rho_w/\rho_{re}} = 0.07$

FIGURE 4.7: The variation of $\sigma_{d_{w/i}}$ in terms of precision and robustness

4.4.1.2 Standard Deviation $\sigma_{\rho_{re}/\rho_i}$ and σ_{ρ_w/ρ_i} in Terms of Precision and Robustness

In terms of precision and robustness, Figures 4.8a, 4.8c, 4.9a and 4.9c show the increasing behavior of the range standard deviations $\sigma_{\rho_{re}/\rho_{est}}$ and $\sigma_{\rho_w/\rho_{est}}$ after the LGCM calibration, due to:

- the increase of pitch angle ϕ_x in positive and negative sides, which decreases the sparsity of impact points on the ground. This leads to decrease the precision of plane fitting estimation.
- the increase of LiDAR range accuracy $\sigma_{\rho_w/\rho_{re}}$, that decreases the precision of plane fitting estimation.

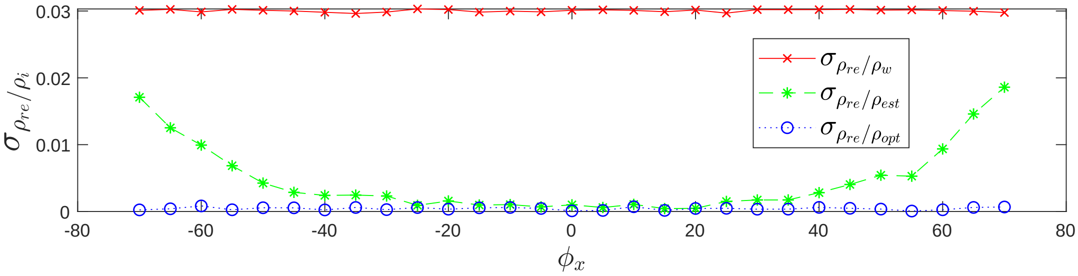

(a) variation of $\sigma_{\rho_{re}/\rho_i}$ with respect to ϕ_x

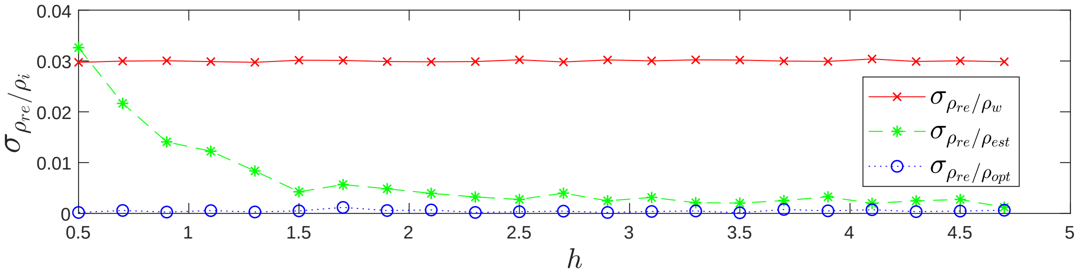

(b) variation of $\sigma_{\rho_{re}/\rho_i}$ with respect to h

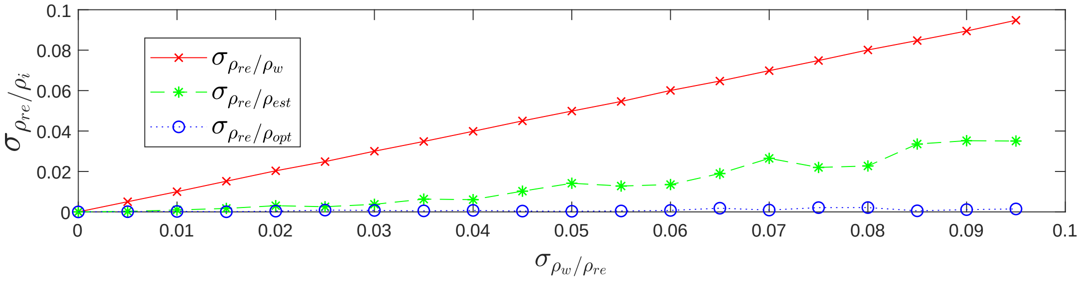

(c) variation of $\sigma_{\rho_{re}/\rho_i}$ with respect to $\sigma_{\rho_w/\rho_{re}}$

FIGURE 4.8: The variation of $\sigma_{\rho_{re}/\rho_i}$ in terms of precision and robustness

Vice versa, Figures 4.8b and 4.9b show the decreasing of the range standard deviations $\sigma_{\rho_{re}/\rho_{est}}$ and $\sigma_{\rho_w/\rho_{est}}$ after the LGCM calibration, due to increasing of height h that increases the sparsity of impact points on the ground, which leads to increase the precision of plane fitting estimation.

The standard deviation $\sigma_{\rho_{re}/\rho_{opt}}$ is lower than the standard deviation $\sigma_{\rho_{re}/\rho_{est}}$ as shown in Figures 4.8a, 4.8b and 4.8c, which indicate how the optimized

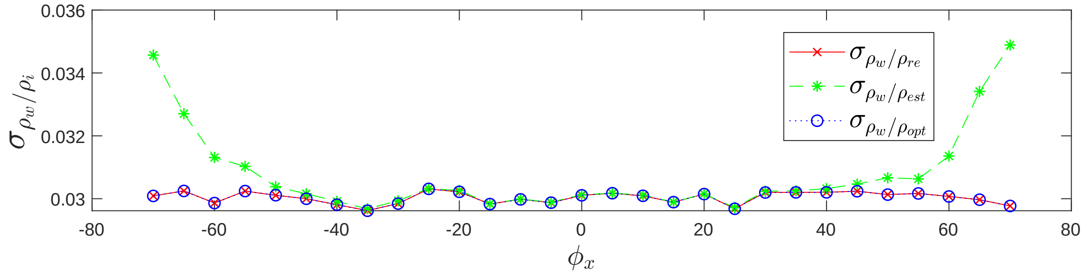

(a) variation of σ_{ρ_w/ρ_i} with respect to ϕ_x

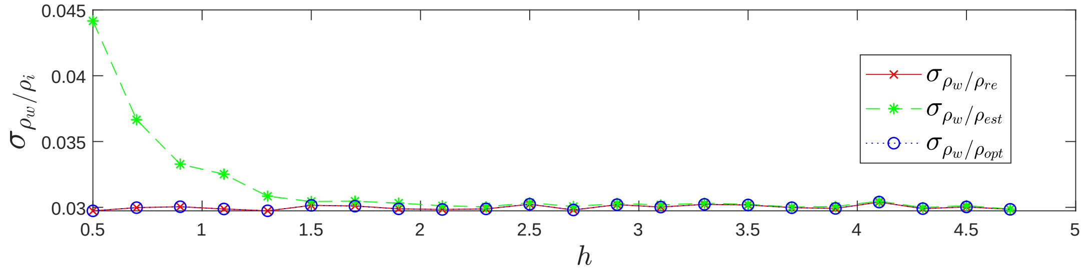

(b) variation of σ_{ρ_w/ρ_i} with respect to h

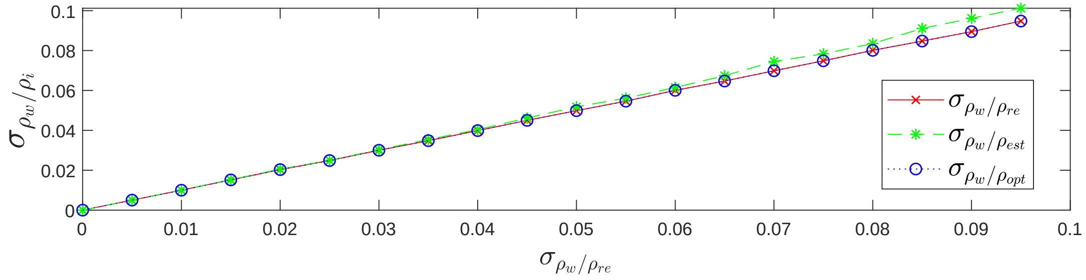

(c) variation of σ_{ρ_w/ρ_i} with respect to $\sigma_{\rho_w/\rho_{re}}$

FIGURE 4.9: The variation of σ_{ρ_w/ρ_i} in terms of precision and robustness

points c_{opt} are closer to the real points c_{re} than the estimated points c_{est}. On the other hand, the standard deviation $\sigma_{\rho_w/\rho_{opt}}$ is very close to LiDAR range accuracy $\sigma_{\rho_w/\rho_{re}}$ than for the standard deviation $\sigma_{\rho_w/\rho_{est}}$ as shown in Figures 4.9a, 4.9b and 4.9c, which indicate the similarity of the noisy points c_w range distribution along the real plane (P_{re}) and the optimized plane (P_{opt}).

The negligibility of standard deviation $\sigma_{\rho_{re}/\rho_{opt}}$ in Figures 4.8a, 4.8b and 4.8c, and the coincidence of standard deviations $\sigma_{\rho_w/\rho_{opt}}$ and $\sigma_{\rho_w/\rho_{re}}$ in Figures 4.9a, 4.9b and 4.9c, proves the similarity of the real plane (P_{re}) and the optimized plane (P_{opt}) other than the estimated plane (P_{est}).

4.4.1.3 Height Estimation in Terms of Precision and Robustness

In terms of precision and robustness, Figure 4.10 highlights the recovering of the height parameter and how the optimized height $\hat{h}_{opt}$ is closer to the real height h than the estimated height $\hat{h}$, which presents the height optimization importance and the strength of the Levenberg-Marquardt optimization algorithm.

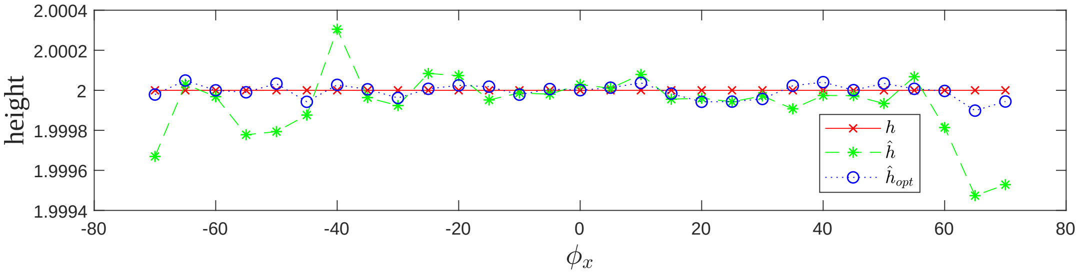

(a) variation of height with respect to ϕ_x

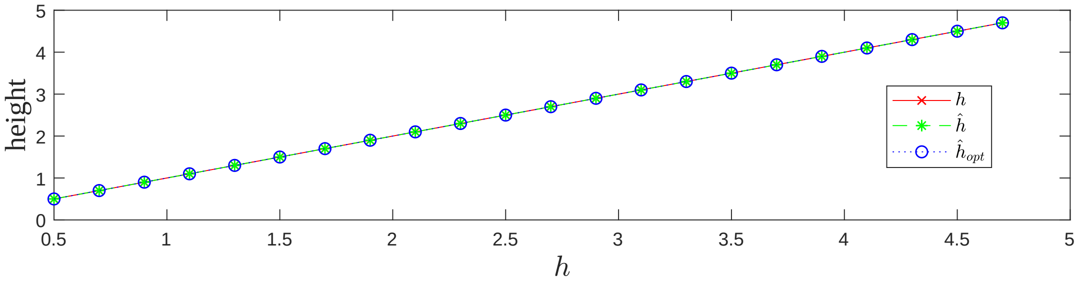

(b) variation of height with respect to h

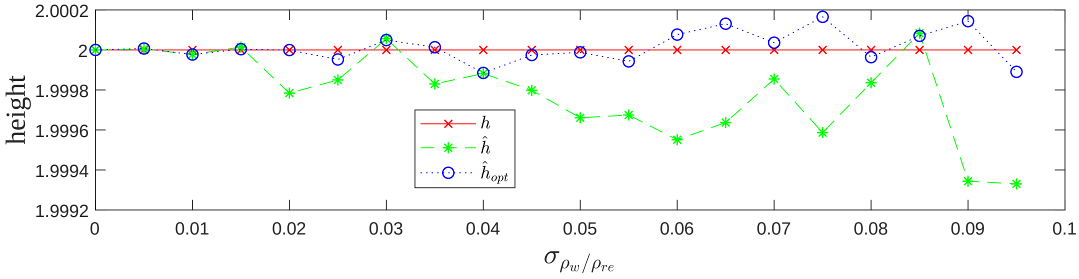

(c) variation of height with respect to $\sigma_{\rho_w/\rho_{re}}$

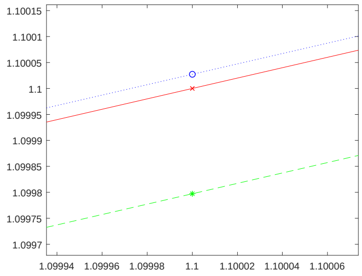

(d) zoom in (b) at $h = 1.1$

FIGURE 4.10: Height recovering in terms of precision and robustness

4.4.1.4 Performance Gain PF_i in Terms of Precision and Robustness

Figure 4.11 shows the gain in performance of the optimized plane points c_{opt} against the estimated plane points c_{est} distributed by the noisy points c_w compared to the LiDAR range accuracy $\sigma_{\rho_w/\rho_{re}}$ as expressed in Equation 4.33, with respect to the variation of pitch angle ϕ_x, height h and LiDAR range accuracy $\sigma_{\rho_w/\rho_{re}}$. Moreover, the negligible of the method performance PF_{opt} after the optimization means that the standard deviation $\sigma_{\rho_w/\rho_{opt}}$ after optimization is closer than the standard deviation $\sigma_{\rho_w/\rho_{est}}$ before optimization to the LiDAR range accuracy $\sigma_{\rho_w/\rho_{re}}$. In addition, it presents the recovering of noisy points c_w range distribution along the real plane (P_{re}) after the optimization algorithm, taking in advantage of maintaining the standard deviation $\sigma_{\rho_w/\rho_{opt}}$ value as negligible. The gain feature PF_i proves again the better fit between the optimized plane (P_{opt}) and the real plane (P_{re}) rather than the estimated plane (P_{est}).

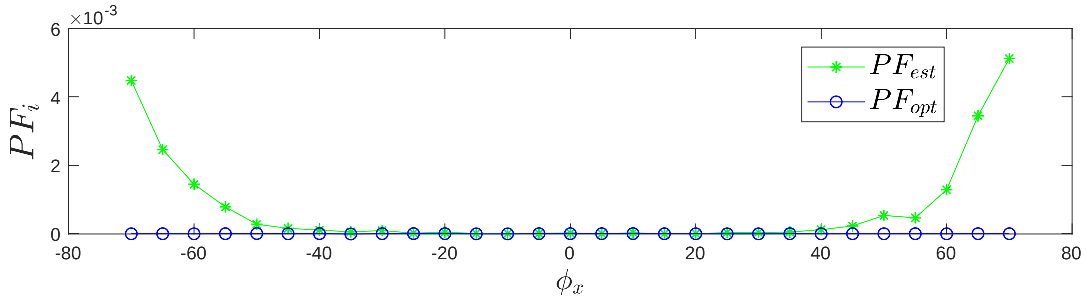

(a) variation of PF_i with respect to ϕ_x

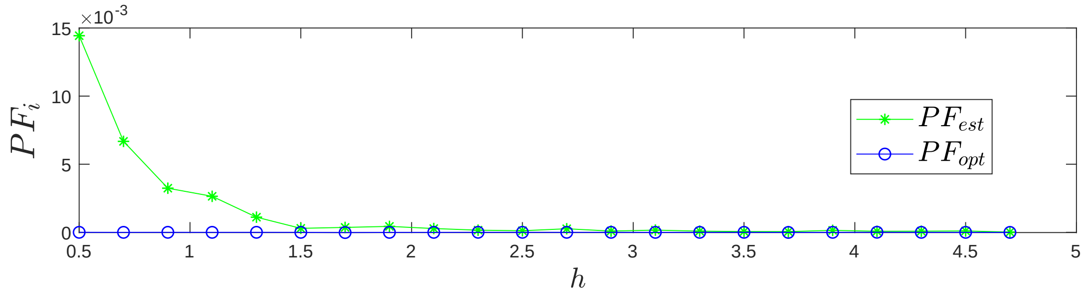

(b) variation of PF_i with respect to h

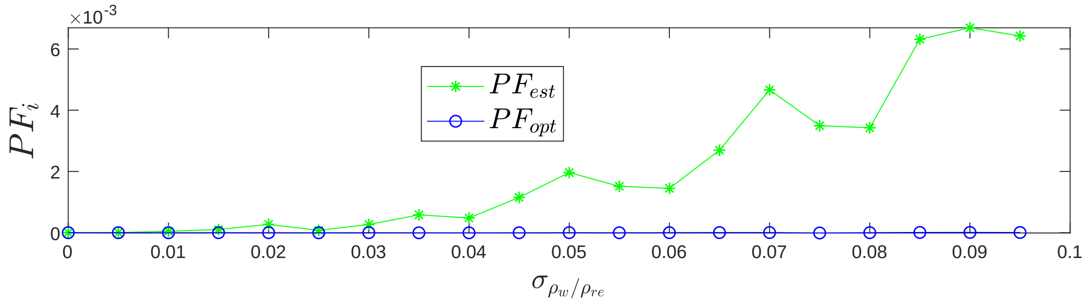

(c) variation of PF_i with respect to $\sigma_{\rho_w/\rho_{re}}$

FIGURE 4.11: The variation of PF_i in terms of precision and robustness

4.4.2 Real Data Results

The 3D point cloud acquisitions are obtained using a multi-lasers rangefinder VLP-16 LiDAR mounted on a vehicle. In order to obtain a telemetric information about the ground surface and to achieve the application goal, the VLP-16 LiDAR is rotated toward the ground direction with a pitch angle $\phi_x \simeq 70^\circ$ and is at a height $h \simeq 1.05m$ above the ground surface. The real setup is shown in Figure 3.6a.

The proposed method is applied to two different acquisitions:

- Acquisition 1: the vehicle is at rest on the road.
- Acquisition 2: the vehicle is moving at a slow speed on the road.

Standard Deviation σ_{ρ_w/ρ_i} per LiDAR Frames

In the absence of real plane (P_{re}) when using real data, the results focus on the range distribution of the noisy points c_w along the estimated plane (P_{est}) and the optimized plane (P_{opt}). It is clear that the standard deviations $\sigma_{\rho_w/\rho_{opt}}$ curve is lower than the $\sigma_{\rho_w/\rho_{est}}$ in the two acquisitions as shown in Figure 4.12. The optimization algorithm is thus proved to be more efficient for real data as well in decreasing the range distribution of the noisy points c_w along the fitting planes.

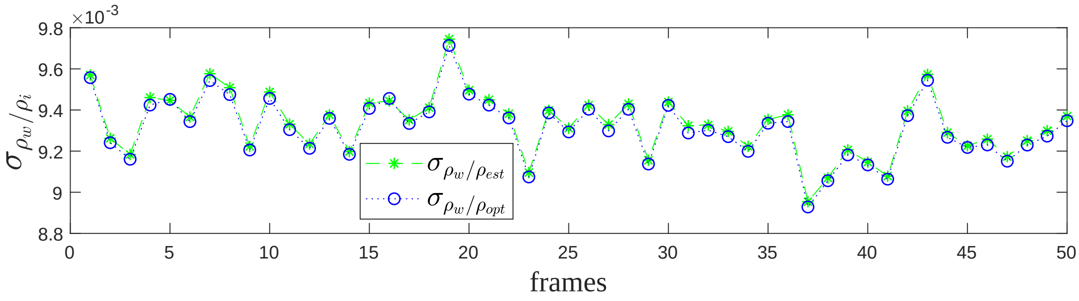

(a) Acquisition 1

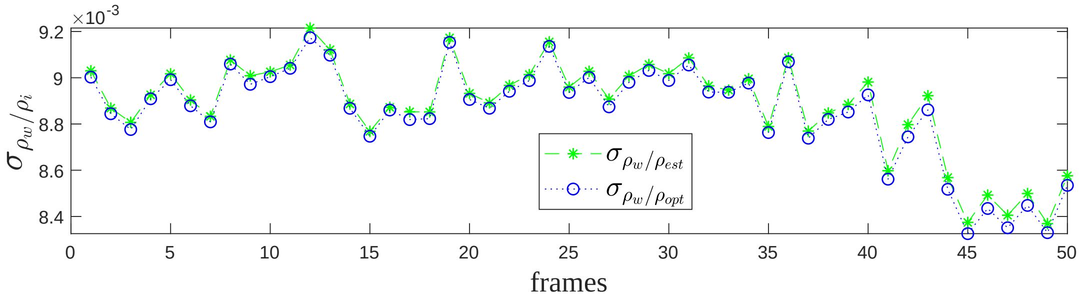

(b) Acquisition 2

FIGURE 4.12: The variation of σ_{ρ_w/ρ_i} with respect to LiDAR frame

4.4.3 Results Discussion

In general, the results turn out to prove the efficiency of the optimization algorithm which is represented by the optimized plane (P_{opt}), versus the estimated plane (P_{est}), compared with the real plane (P_{re}), in terms of precision and robustness. On other hand, the convergence of the optimization algorithm is granted automatically by the suitable initialization parameters: the estimated Euler's angles $\hat{\psi}_z, \hat{\theta}_y, \hat{\phi}_x$ and the estimated height $\hat{h}$ that are computed in stage one (LGCM) to obtain the estimated plane (P_{est}), then optimized by Levenberg-Marquardt optimization algorithm (opt-LGCM) in stage two to get the optimized Euler's angles $\hat{\psi}''_z, \hat{\theta}''_y, \hat{\phi}''_x$ and the optimized height $\hat{h}_{opt}$ in order to obtain the optimized plane (P_{opt}). Finally, the results show the strength and the method performance in terms of precision and robustness against the variation of pitch angle ϕ_x and LiDAR range accuracy $\sigma_{\rho_w/\rho_{re}}$ respectively, in order to achieve the application's aim as shown in Figure 4.13.

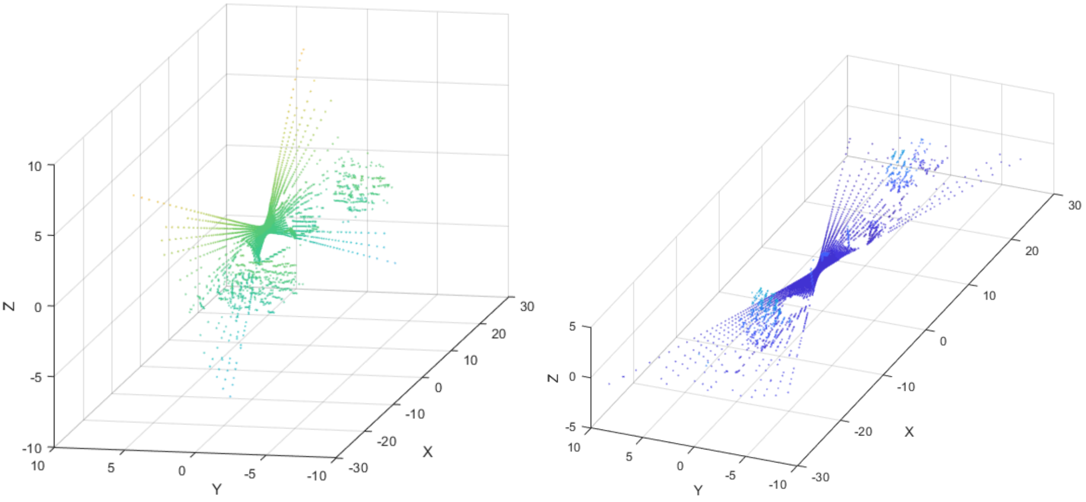

(a) uncalibrated frame (b) calibrated frame

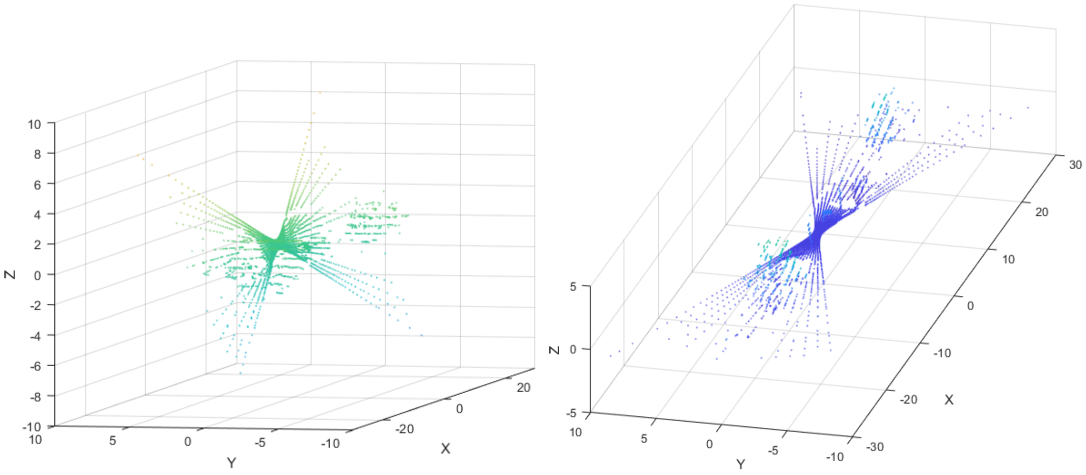

(c) uncalibrated frame (d) calibrated frame

FIGURE 4.13: uncalibrated and calibrated LiDAR frames from acquisitions 1 and 2

4.5 Conclusion

A new global extrinsic LiDAR/Ground calibration method for 3D cylindrical LiDARs is modeled on 4-DOF unlike the previous 6-DOF calibration method, to fit the problematic case study due to the high orientation of LiDAR sensor. Due to the modeling difference concept between 4-DOF and 6-DOF, it is impractical to compare our proposed calibration method with other methods. The solution relies on plane-based modeling of the ground which allows the estimation of the LiDAR's orientation and altitude using Rodrigues formula, Least Squares Conic Algorithm for yaw angle estimation and height estimation. The proposed method LGCM is extended to an optimized derivation opt-LGCM using the Levenberg-Marquardt algorithm and is shown to be a suitable solution to LiDAR/Ground calibration problem. It is implemented on LiDAR's synthetic and real telemetric data. The results show the performance in terms of precision and robustness against the variation of LiDAR's orientation and range accuracy respectively, proving the stability and the accuracy of the proposed calibration method.

Chapter 5

Road Defect Detection Methods

5.1 Introduction

In this chapter, we present the kernel objective of this thesis, that aims to detect, identify, visualize and localize the road defects in each LiDAR frame. In fact, a prior procedure is applied to the LiDAR frame after the extrinsic calibration process as shown in Figure 5.1, in order to obtain a better results by the detection methods, because the road's defect affects the extrinsic calibration process results, due to the ground consideration as a flat plane.

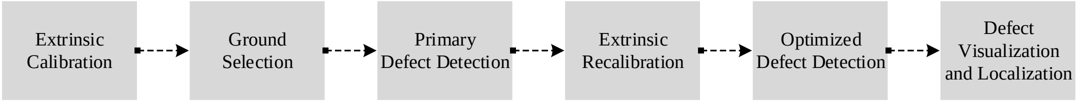

FIGURE 5.1: Prior defect detection process

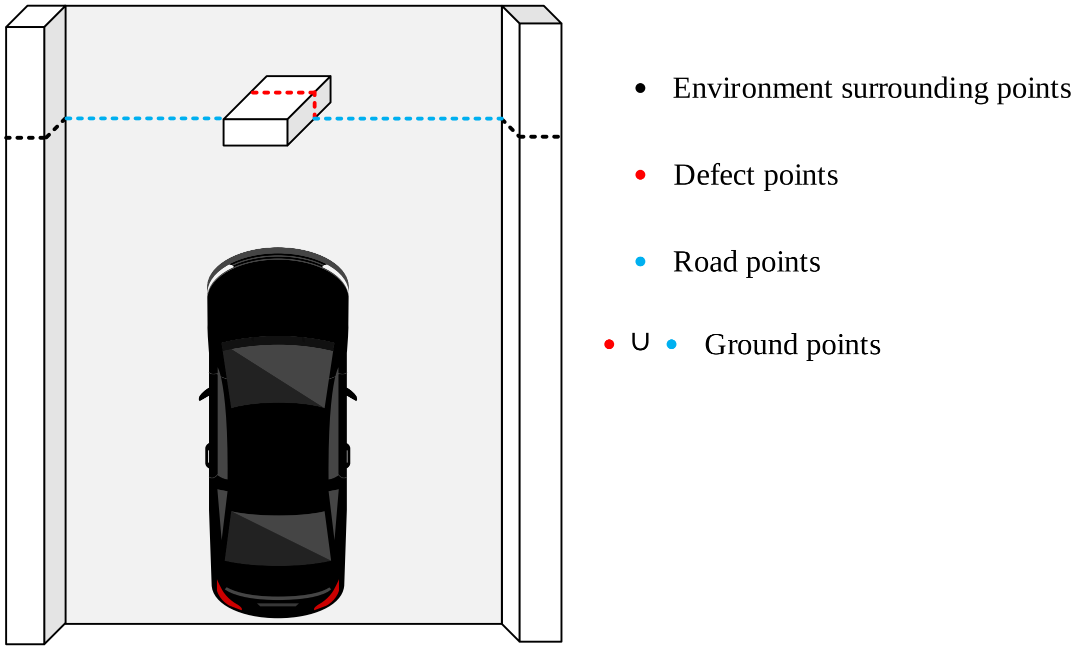

FIGURE 5.2: Different PointCloud labels

Therefore, the procedure starts with ground points selection to remove the environment surrounding points that are outside the road zone as shown in Figure 5.2. Then, a primary feature-based defect detection method is initially applied to extract and separate the defects points from the road points, followed by the same previous extrinsic calibration method just on the road points avoiding the defects points, which clearly enhances the extrinsic recalibration results. Finally, two defect detection methods are executed successfully on the calibrated ground points, to ensure and increase the detection precision in a perfect calibrated frame. The first method is an optimized feature-based method that depends on the altitude concavity feature to **detect and identify** the defects. While, the second method is a grid-based method that transforms the calibrated ground points from 3D point cloud frame into 2D image, depending on the altitude distribution feature in each spatial grid, in order to **detect, visualize and localize** the defects.

In the next section, the view scene results are implemented directly on real data acquisition as shown in Figure 5.3. The recorded acquisition scenario takes in consideration the existence of two edges on both sides of the ground, where the first right edge is characterized by one corner and the second left edge by two corners. In addition, the acquisition includes two types of defects: hump and hole defects, in other words positive and negative defects respectively [107].

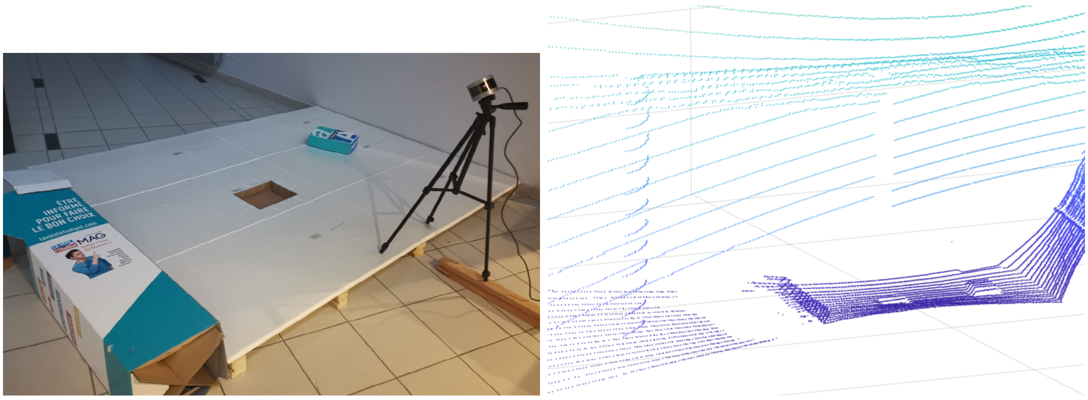

(a) View scene photo

(b) 3D PointCloud zoom in frame

FIGURE 5.3: Acquisition of hump and pothole defects

5.2 Ground Selection

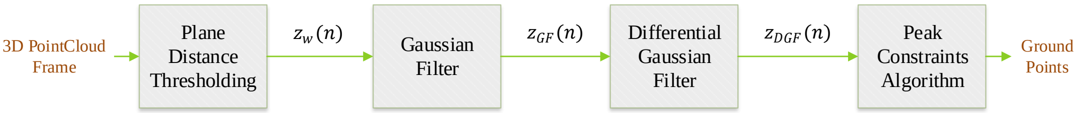

FIGURE 5.4: Ground points selection procedure

As mentioned before, the ground selection procedure aims to extract the ground points from full points of the LiDAR frame, making it easier to study and analyze the defect existence just on the road zone. Referring to Figure 5.4, the ground points selection procedure includes four main steps: plane distance thresholding to bound the interest study region, Gaussian filter to smooth the signal, differential Gaussian filter to detect the road edges center and Peak Constraints Algorithm to detect the inner corner of the road edges. Each step is explained in details with its role in the next subsections.

5.2.1 Plane Distance Thresholding

Initially, the role of plane distance thresholding step is to bound the interest study zone of the 3D point cloud full frame to an environment points (road, defects and road edges), which eliminates all unnecessary outer points from the study zone as shown in Figure 5.5. This step depends on the orthogonal Euclidean distance threshold constraint $d_{th} = 30cm$ from the LiDAR noisy point $c_w(x_w, y_w, z_w)$ to the optimized plane (P_{opt}) as expressed in Equations 5.1 and 5.2, since the most representative plane of the ground is the optimized plane (P_{opt}) after the extrinsic calibration process. Where the orthogonal Euclidean distance threshold d_{th} must be high enough to cover the height of the road edges, that consist of two corners.

$$d_{w/opt} = \frac{|A_{opt}x_w + B_{opt}y_w + C_{opt}z_w + D_{opt}|}{\sqrt{A_{opt}^2 + B_{opt}^2 + C_{opt}^2}} \tag{5.1}$$

$$d_{w/opt} \leq d_{th} \tag{5.2}$$

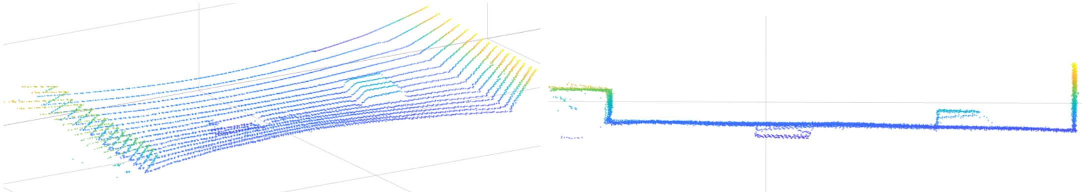

(a) Top left view (b) Forward side view

FIGURE 5.5: Acquisition of hump and hole defects

5.2.2 Gaussian Filter

Gaussian filter is one of average filters in time domain to mitigate the noise effect, where the Fourier transform of Gaussian impulse response in frequency domain is also Gaussian distribution centered at zero. This is what clarifies that Gaussian filter is a type of low-pass filter. Referring to Figure 5.6, which represents the convolution relationship in the output signal $z_{GF}(n)$ between the input altitude signal $z_w(n)$ and the impulse response system $h_{GF}(n)$, as expressed in Equations 5.3 and 5.4.

$$z_{GF}(n) = z_w(n) * h_{GF}(n) \tag{5.3}$$

$$h_{GF}(n) = \frac{G}{\sqrt{2\pi\sigma^2}} \exp\left(\frac{-n^2}{2\sigma^2}\right) \quad \text{for } -3\sigma \leq n \leq 3\sigma \tag{5.4}$$

Where G is a gain parameter for signal amplification, σ is the standard deviation of the Gaussian distribution, and n is the points' index number of the signals z_w, z_{GF} and the impulse response system h_{GF}.

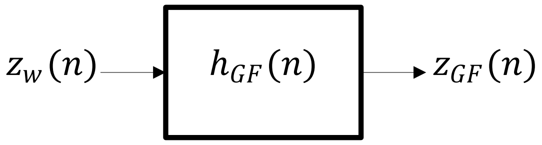

(a) System input & output

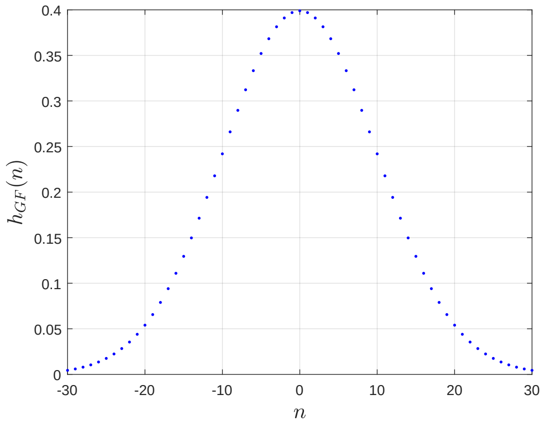

(b) Gaussian impulse response

FIGURE 5.6: Gaussian filter system

In this step, the Gaussian filter system $h_{GF}(n)$ deals with each elevation impact points as an individual noisy discrete signal $z_w(n)$ to mitigate the noise effect and especially for the high noisy impact points that exist on surface edges, in order to get a smoothed discrete signal $z_{GF}(n)$ as shown in Figure 5.7. In addition, the edge localization accuracy decreases when the Gaussian filter's spread increases in the index n domain, which imposes a trade-off between edge localization accuracy and noise filtering.

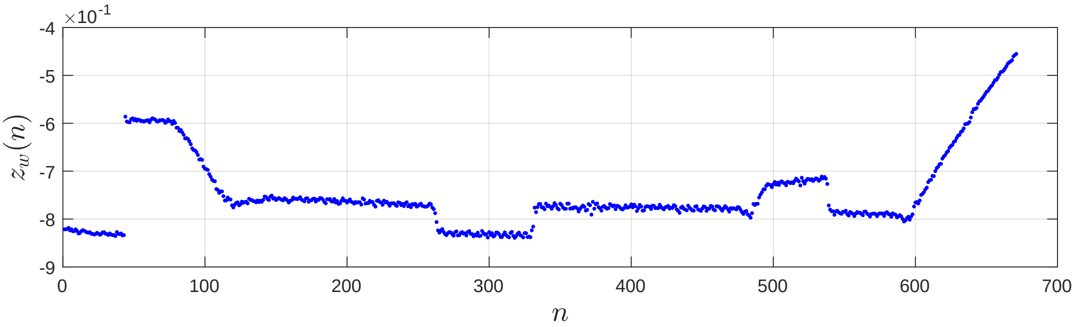

(a) Signal $z_w(n)$ at elevation $\beta = -3°$

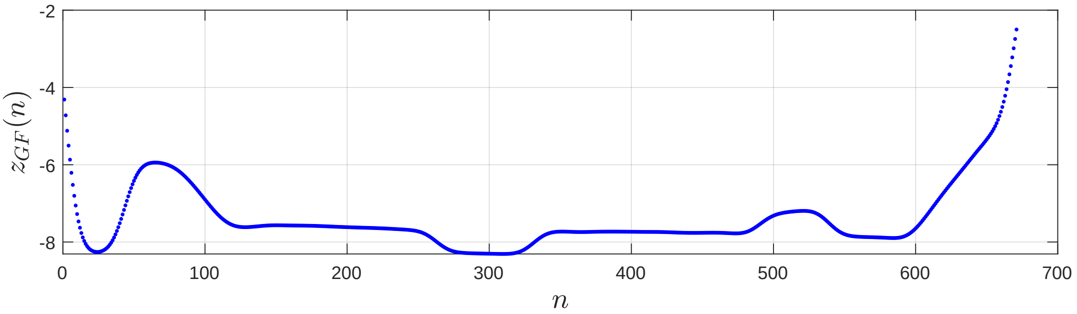

(b) Signal $z_{GF}(n)$ at elevation $\beta = -3°$

FIGURE 5.7: Input and output signals

5.2.3 Differential Gaussian Filter

Differential Gaussian filter is a system that represents the first derivative of an input signal, which indicates the slope or the instantaneous rate variation (increasing or decreasing) of the input signal. In addition, the differential Gaussian filter function is simply a subtraction between two shifted Gaussian functions in an opposite direction as expressed in Equation 5.6. Referring to Figure 5.8, which represents the convolution relationship in the output signal $z_{DGF}(n)$ between the input signal $z_{GF}(n)$ and the impulse response system $h_{DGF}(n)$, as expressed in Equation 5.5.

$$z_{DGF}(n) = z_{GF}(n) * h_{DGF}(n) \tag{5.5}$$

$$\begin{aligned} h_{DGF}(n) =& \frac{G}{\sqrt{2\pi\sigma^2}} \exp\left(\frac{-(n-\mu)^2}{2\sigma^2}\right) \\ &- \frac{G}{\sqrt{2\pi\sigma^2}} \exp\left(\frac{-(n+\mu)^2}{2\sigma^2}\right) \text{ for } \begin{cases} -\mu \le n \le \mu \\ \sigma = \mu/2 \end{cases} \end{aligned} \tag{5.6}$$

Where G is a gain parameter for signal amplification, σ is the standard deviation of the Gaussian distribution, and n is the points' index number of the signals z_{GF}, z_{DGF} and the impulse response system h_{DGF}.

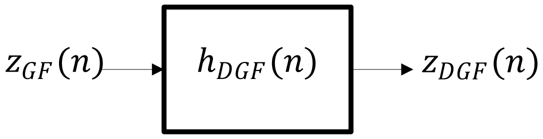

(a) System input & output

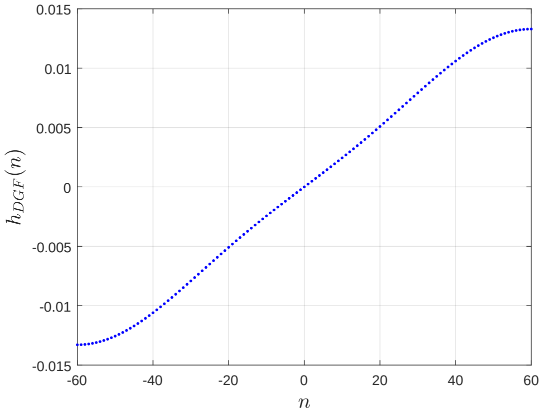

(b) Differential Gaussian impulse response

FIGURE 5.8: Differential Gaussian filter system

In this step, the differential Gaussian filter h_{DGF} deals with each smoothed discrete signal sample $z_{GF}(n)$ to indicate the transition sense in the $z_{DGF}(n)$ signal as shown in Figure 5.9.

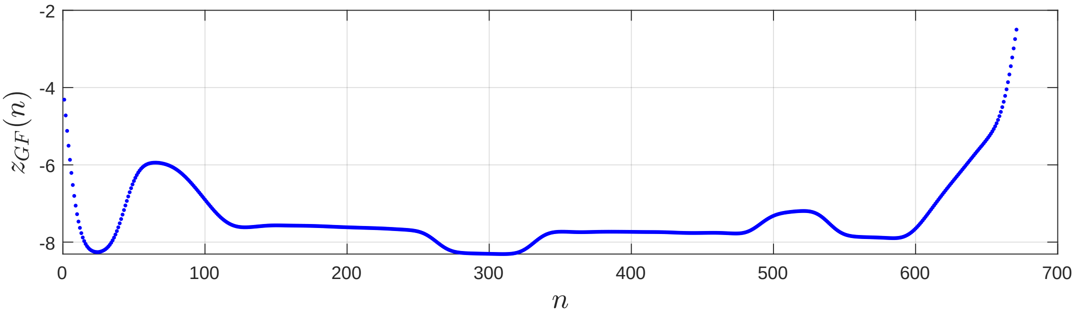

(a) Signal $z_{GF}(n)$ at elevation $\beta = -3^\circ$

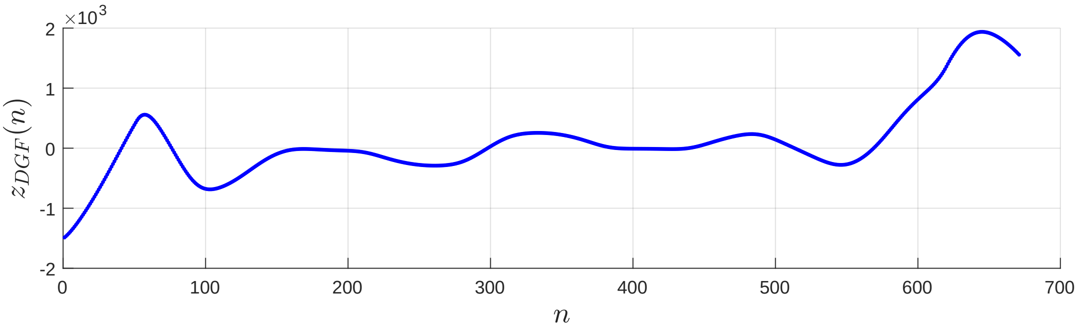

(b) Signal $z_{DGF}(n)$ at elevation $\beta = -3^\circ$

FIGURE 5.9: Input and output signals

5.2.4 Peak Constraints Algorithm PCA

The role of Peak Constraints Algorithm PCA is to extract both edges of the road as presented in Algorithm 2. The algorithm is based on several peak conditions, applied on the road's left and right side.

Algorithm 2: Peak Constraints Algorithm

```
Input: Signal $z_{DGF}(n)$
Output: Boundary indexes of the road edges $i_r, i_l$
Find the main first right and last left peaks $pk_{r1}, pk_{l1}$ of the $z_{DGF}(n)$
  signal on the road's right and left sides respectively as shown in Figure
  5.10a, provided that the peaks values $z_{DGF}(i_{r1}), z_{DGF}(i_{l1})$ must be
  higher than a constant threshold $pk_{th} = 450$ as expressed in the below
  inequalities, which identify a high transitions of the road edges in the
  signal $z_{GF}(n)$ that are higher than the transitions of the road defects.
  Where the indexes $i_{r1}, i_{l1}$ values of the main peaks indicate the
  midpoints of the edge width in $z_{GF}(n)$ signal.
  $|z_{DGF}(i_{r1})| \geq pk_{th}$
  $|z_{DGF}(i_{l1})| \geq pk_{th}$
Find the first side lobe peaks $pk_{r2}, pk_{l2}$ before and after the peaks
  $pk_{r1}, pk_{l1}$ respectively, as shown in Figure 5.10b. Where the side lobes
  indexes are noted as $i_{r2}, i_{l2}$.
Compute the indexes $i_r, i_l$ of the right and left boundary $b_r, b_l$ of the road
  edges, which represent the midpoint indexes of the main and side lobe
  peaks, as shown in Figure 5.10c and expressed in the below equations:
  $i_r = (i_{r1} + i_{r2}) / 2$
  $i_l = (i_{l1} + i_{l2}) / 2$
```

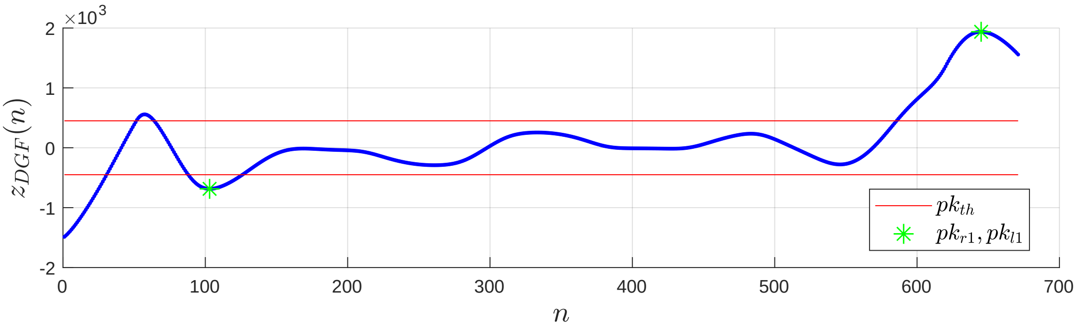

(a) First step of PCA on $z_{DGF}(n)$ signal at elevation $\beta = -3°$

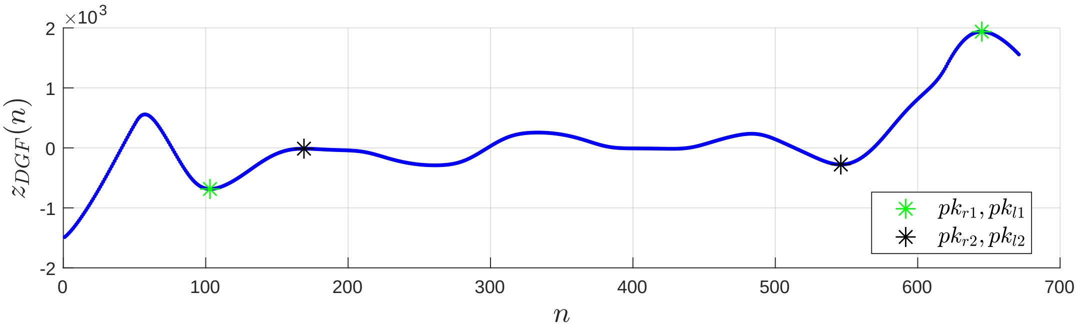

(b) Second step of PCA on $z_{DGF}(n)$ signal at elevation $\beta = -3°$

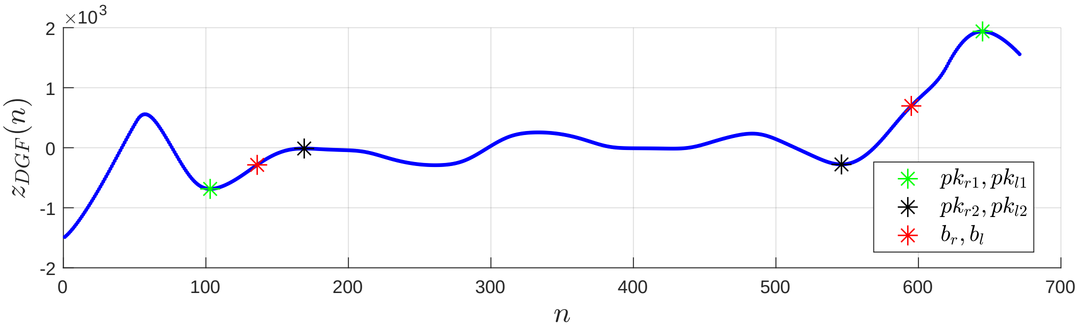

(c) Third step of PCA on $z_{DGF}(n)$ signal at elevation $\beta = -3°$

FIGURE 5.10: PCA input signal

After finding the right and left boundary b_r, b_l of the road, the original altitude signal $z_w(n)$ is clipped between both boundary indexes b_r, b_l in order to eliminate the road edges as shown in Figure 5.11.

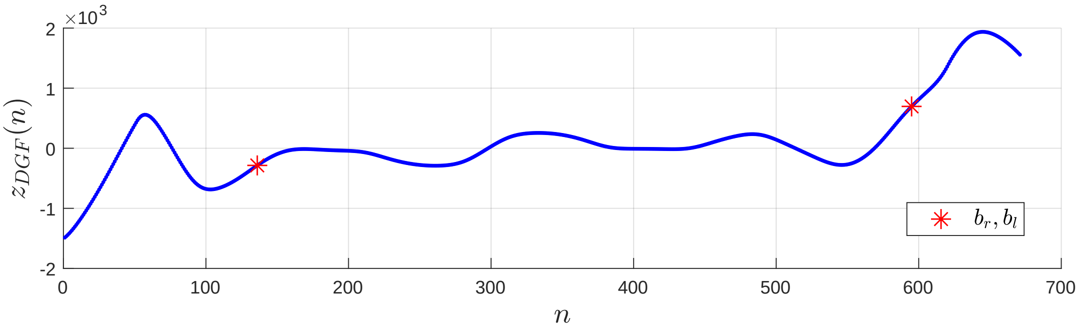

(a) Signal $z_{DGF}(n)$ at elevation $\beta = -3°$

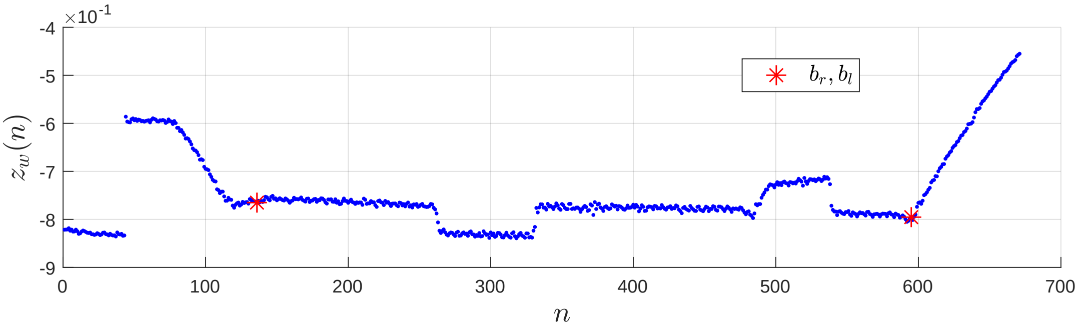

(b) Signal $z_w(n)$ before clipping at elevation $\beta = -3°$

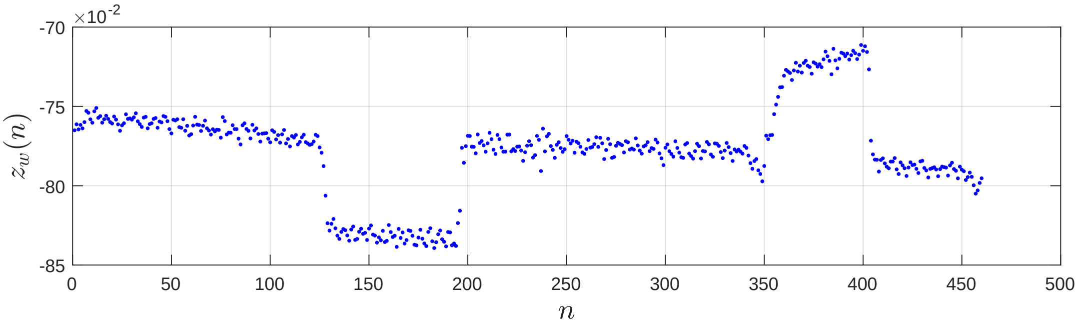

(c) Signal $z_w(n)$ after clipping at elevation $\beta = -3°$

FIGURE 5.11: Signal $z_w(n)$ clipping boundaries

This procedure is applied at each elevation laser impact in order to get a ground selection points, which means extracting the road and the defect points by eliminating the road edges points from the 3D point cloud frame as shown in Figure 5.12.

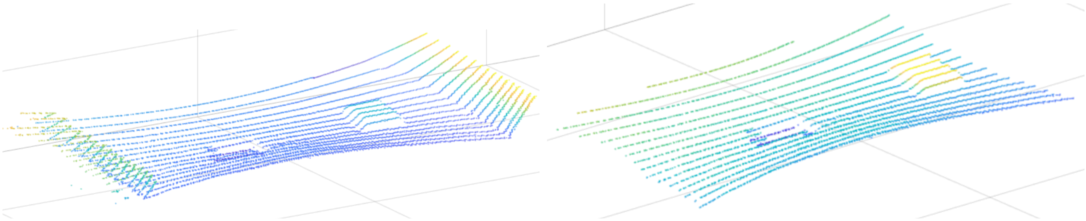

(a) Top left view with road edges (b) Top left view without road edges

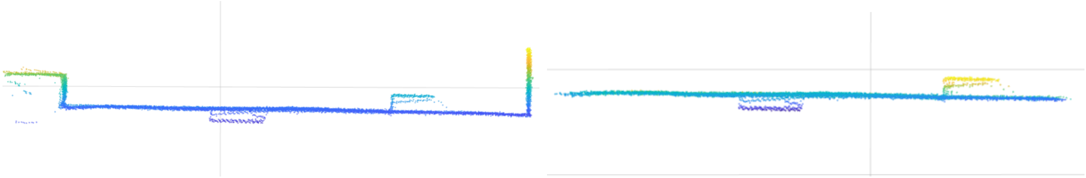

(c) Forward side view with road edges (d) Forward side view without road edges

FIGURE 5.12: Road edges filtering

5.3 Feature-Based Defect Detection Method FBDDM

Moving to the first detection approach, the Feature-Based Defect Detection Method FBDDM depends on the altitude concavity feature to extract the homogeneous defect patterns that exist below or above the road network. For this, the second order of differential Gaussian filter $h_{DGF2}(n)$ represents the second derivative of an input signal, which indicates the concavity feature in the output signal z_{DGF2} of the input signal $z_w(n)$ as shown in Figure 5.13. In addition, one advantage of second order differential Gaussian filter is being low sensitive to the noise effect because of its wide spread in the index n domain, which is doubled than the first order, since the second order differential Gaussian filter consists of two consecutive differential Gaussian impulse responses as expressed in Equation 5.7.

$$\begin{aligned} z_{DGF2}(n) &= z_w(n) * h_{DGF2}(n) \\ &= z_w(n) * h_{DGF}(n) * h_{DGF}(n) \end{aligned} \tag{5.7}$$

$$\begin{aligned} h_{DGF}(n) =& \frac{G}{\sqrt{2\pi\sigma^2}} \exp\left(\frac{-(n-\mu)^2}{2\sigma^2}\right) \\ &- \frac{G}{\sqrt{2\pi\sigma^2}} \exp\left(\frac{-(n+\mu)^2}{2\sigma^2}\right) \quad \text{for} \begin{cases} -\mu \leq n \leq \mu \\ \sigma = \mu/2 \end{cases} \end{aligned} \tag{5.8}$$

Where G is a gain parameter for signal amplification, σ is the standard deviation of the Gaussian distribution, and n is the points' index number of the signals z_w, z_{DGF}, z_{DGF2} and the system impulse responses h_{DGF}, h_{DGF2}.

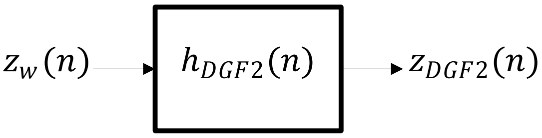

(a) System input and output

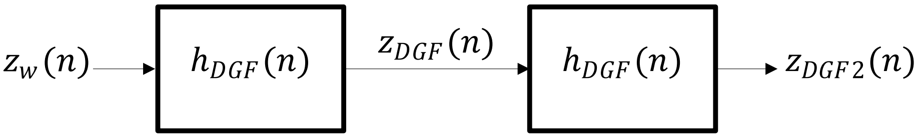

(b) System input and output

FIGURE 5.13: Second order differential Gaussian filter

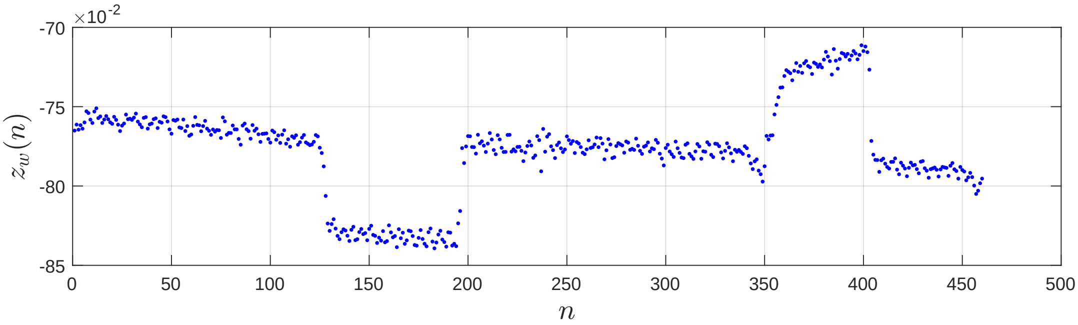

(a) Signal $z_w(n)$ at elevation $\beta = -3°$

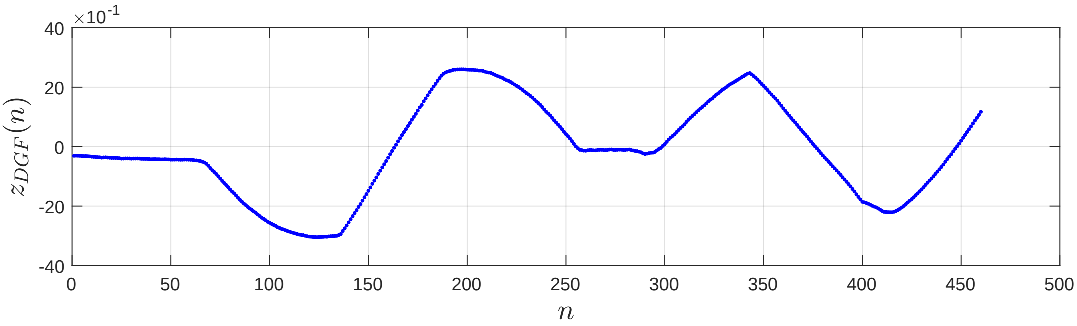

(b) Signal $z_{DGF}(n)$ at elevation $\beta = -3°$

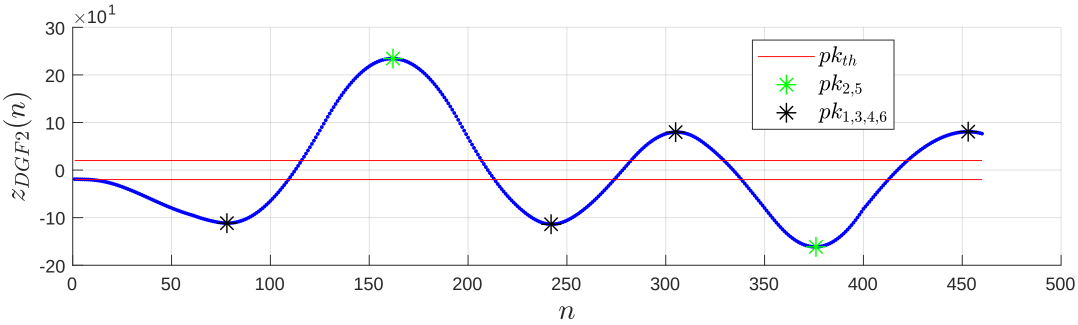

(c) Signal $z_{DGF2}(n)$ at elevation $\beta = -3°$

FIGURE 5.14: Second order differential Gaussian filter input and output

To start on, the altitude signal $z_w(n)$ is fed through a double differential Gaussian system, where the first output $z_{DGF}(n)$ identifies the transition sense feature of the input signal $z_w(n)$ as mentioned before in section 5.2.3, and the second output $z_{DGF2}(n)$ identifies the concavity feature of the input signal $z_w(n)$ as shown in Figure 5.14. Where the sign of the concavity feature, positive or negative, identify the type of the road defect whether its pothole or hump.

Referring to Figure 5.14c, the signal analysis indicates that the indexes of the primary peaks pk_2, pk_5 represent the midpoint or the center point of the pothole and the hump respectively, and the secondary peaks pk_1, pk_3, pk_4, pk_6 are the sides lobes of the main peaks. But, in order to distinguish the primary peaks that represent the existence of defects, the Instantaneous Differential Gaussian Algorithm IDGA is applied on each peak to mitigate the False alarm detection and to measure the defect width as explained in Algorithm 3. The principle of the Algorithm 3 is to compute the concavity magnitude of the altitude signal $z_w(n)$ at each instantaneous peak pk_i with various widths of the filter h_{DGF2}. The concavity magnitude will then reach the maximum value when the filter width covers the defect width.

```
Algorithm 3: Instantaneous Differential Gaussian Algorithm
Input: Signal $z_{DGF2}(n)$
Output: Defect midpoint index $n_i$ and defect width $2n_{IDGF2}$
1 Find all candidature peaks $pk_i$ with their indexes $n_i$ in the $z_{DGF2}(n)$
    signal as shown in Figure 5.14c, taking in account that the peaks values
    $z_{DGF2}(n_i)$ must be higher than a low constant threshold $pk_{th} = 20$ as
    expressed in the below inequality, which find and identify all the
    candidate defects existence in the signal $z_w(n)$. Where the indexes $n_i$
    values indicate the midpoints of the defect in $z_w(n)$ signal.
    $|z_{DGF}(n_i)| \geq pk_{th}$
2 Apply the second order differential Gaussian filter $h_{DGF2}(n)$ with
    increment sequential width $\mu$ at each instantaneous index $n_i$ on the
    altitude signal $z_w(n)$ as shown in the below sub algorithm, where
    $z_{IDGF2}(n)$ signal identify the concavity magnitude of the altitude signal
    $z_w(n)$ at each instantaneous index $n_i$.
      $\mu = 80$   defines the maximum filter width
      $for\ n = 1 : \mu$
          $z_{IDGF2}[n] = |z_w[n_i - 2n : n_i + 2n] .* h_{DGF2}[n]|$
      $end$
3 Find the maximum peak value $pk_{IDGF2}$ and its index $n_{IDGF2}$ for each
    instantaneous signal $z_{IDGF2}$ as shown in Figure 5.15.
4 Compute the ratio $r_{IDGF2}$ that defines the maximum concavity
    magnitude $pk_{IDGF2}$ divided by its index $n_{IDGF2}$ as expressed below.
    Finally, if the ratio $r_{IDGF2}$ is greater than a constant threshold $r_{th} = 3.5$,
    then the candidate peak $pk_i$ represents a primary peak (defect
    existence), characterized by a width $n_{IDGF2}$ points to the right and to
    left of the midpoint index $n_i$. Otherwise, the candidate peak $pk_i$
    represents a secondary peak (no defect existence).
    $r_{IDGF2} = \frac{pk_{IDGF2}}{n_{IDGF2}}$
    $r_{IDGF2} \geq r_{th}$
```

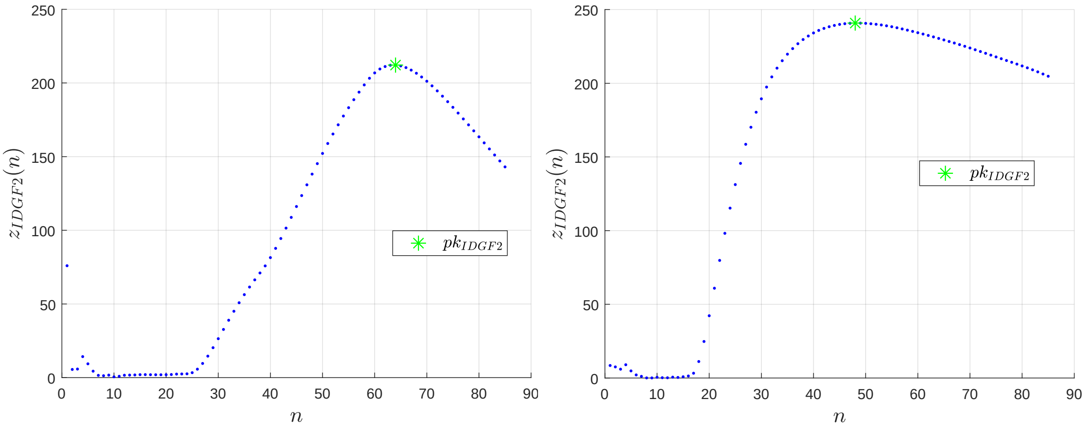

(a) Signal $z_{IDGF2}(n)$ at instantaneous index n_1 of signal $z_w(n)$ (b) Signal $z_{IDGF2}(n)$ at instantaneous index n_2 of signal $z_w(n)$

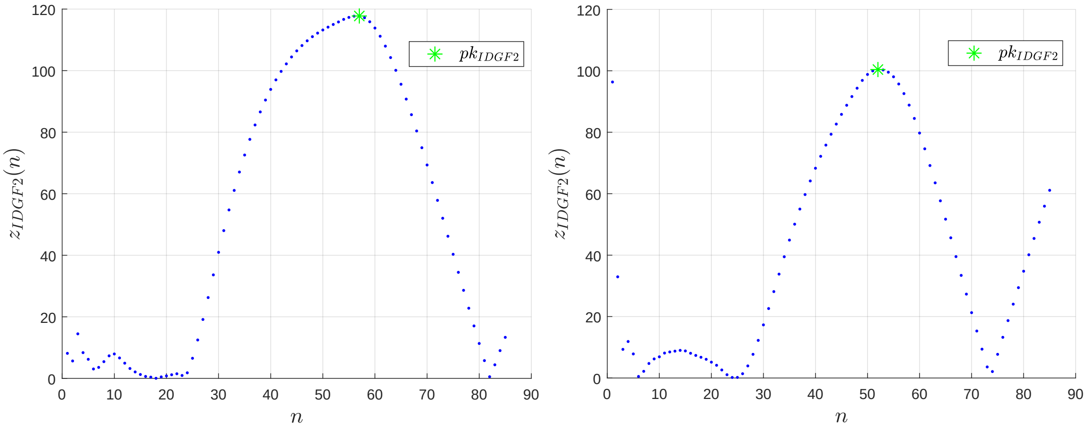

(c) Signal $z_{IDGF2}(n)$ at instantaneous index n_3 of signal $z_w(n)$ (d) Signal $z_{IDGF2}(n)$ at instantaneous index n_4 of signal $z_w(n)$

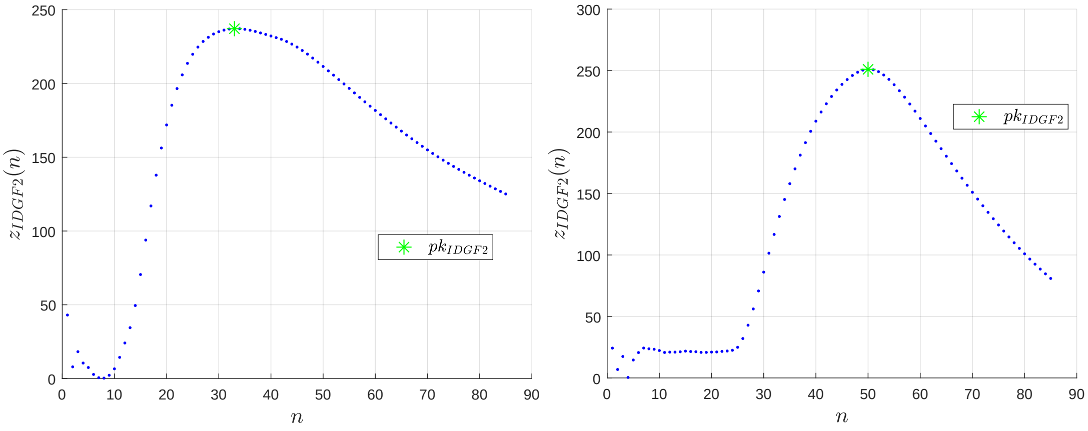

(e) Signal $z_{IDGF2}(n)$ at instantaneous index n_5 of signal $z_w(n)$ (f) Signal $z_{IDGF2}(n)$ at instantaneous index n_6 of signal $z_w(n)$

FIGURE 5.15: Signal $z_{IDGF2}(n)$ with the variation of filter width n at each instantaneous index n_i

Referring to Figure 5.15, the instantaneous differential Gaussian algorithm at peaks pk_3, pk_4 in Figures 5.15c and 5.15d respectively, are not confirm the constraint $r_{IDGF2} \geq r_{th}$, which are true. While, the instantaneous differential Gaussian algorithm at peaks pk_1, pk_2, pk_5, pk_6 in Figures 5.15a, 5.15b, 5.15e, 5.15f respectively, are confirm the constraint $r_{IDGF2} \geq r_{th}$, which are true for peaks pk_2, pk_5 and false for peaks pk_1, pk_6 (False Alarm).

In order to enhance the feature based defect detection results, the LiDAR frame is re-calibrated according to the new optimized extrinsic parameters $\hat{\psi}''_z, \hat{\theta}''_y, \hat{\phi}''_x, \hat{h}_{opt}$ that computed by the road points as shown in Figure 5.16c, which is almost road points, using the same calibration method opt-LGCM that was presented in Chapter 4. The re-calibration method provides better results because of the defect points absence that affects the plane model representation of the road points. Then, the feature based detection method is applied on the elevation lasers of the new recalibrated frame with additional constraint in the instantaneous differential Gaussian algorithm in step 4, in case:

- Positive defect (hump) $pk_i < 0$, then the altitude mean of the candidate point must be closer to the maximum altitude of the candidate points than the altitude mean of the elevation laser points $|\mu_{z_{candidates}} - \max(z_{candidates})| < |\mu_{z_{candidates}} - \mu_{z_{elevation}}|$.
- Negative defect (pothole) $pk_i > 0$, then the altitude mean of the candidate point must be closer to the minimum altitude of the candidate points than the altitude mean of the elevation laser points $|\mu_{z_{candidates}} - \min(z_{candidates})| < |\mu_{z_{candidates}} - \mu_{z_{elevation}}|$.

Finally, the feature based detection method shows an improvement of defect detection results after the re-calibration process. As mentioned before, the feature based defect detection method works on each elevation laser signal z_w that represents the altitude Z-axis with respect to the transverse variation X-axis. So, the feature based defect detection method process must be executed on each elevation laser points to obtain a full frame detection for each of defect and road points separately as shown in Figure 5.16.

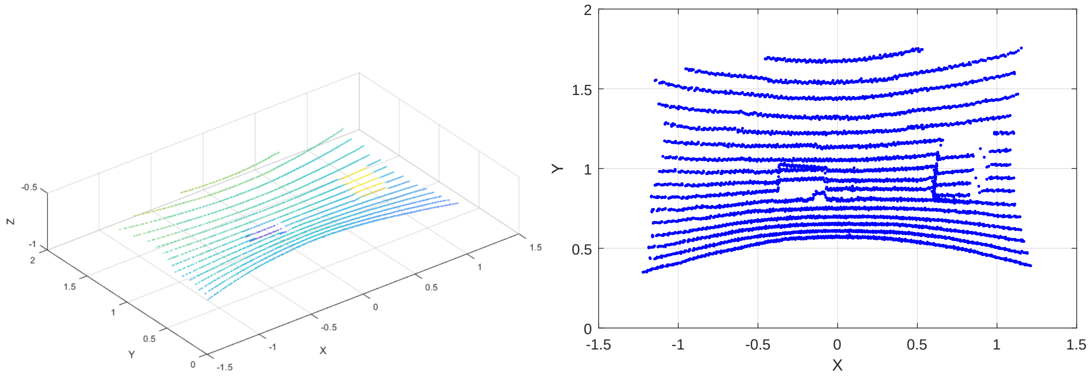

(a) 3D frame of ground points (b) 2D frame of ground points

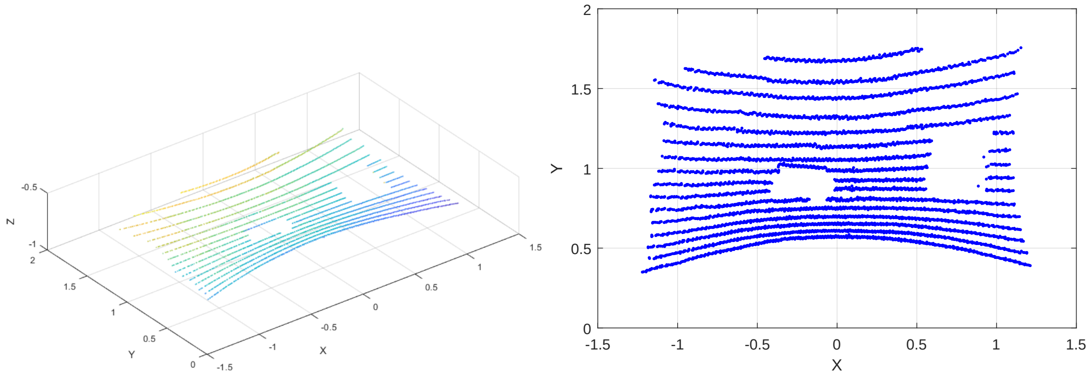

(c) 3D frame of road points (d) 2D frame of road points

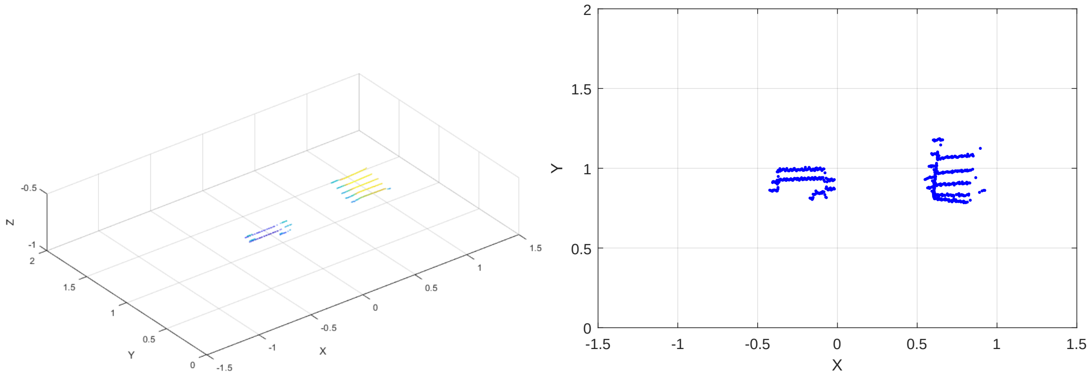

(e) 3D frame of defect points (f) 2D frame of defect points

FIGURE 5.16: 3D and 2D sample frames for ground, road and defect points

5.4 Grid-Based Defect Detection Method GBDDM

Moving to the second detection approach, the Grid-Based Defect Detection Method GBDDM, which is extended method after the Feature-Based Defect Detection Method FBDDM. The principal outlines of this method are: automated detection, high resolved visualization and localization for the road defects in each LiDAR frame. Where this method works directly on the recalibrated 3D ground points frame which includes both of road and defect points as shown in Figure 5.17.

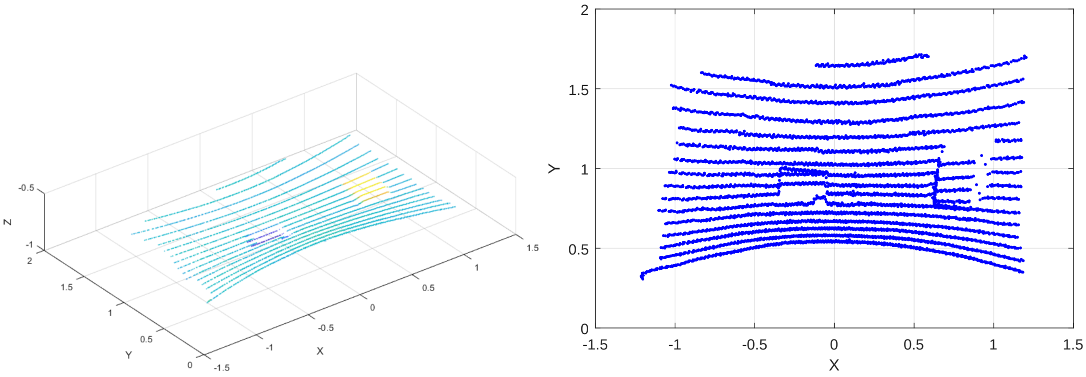

(a) 3D frame of ground points (b) 2D frame of ground points

FIGURE 5.17: 3D and 2D sample frames for ground points after recalibration

Therefore, instead of processing road surface point clouds in 3D space, the grid-based defect detection method projects the 3D points in to 2D plane XY-plane, in order to generate or rasterize a georeferenced gray level image, whose intensity pixels represent a non-linear interpolation based on the euclidean altitude distance $d_{w/opt}$ between the points' altitude z_w and the road altitude $-\hat{h}_{opt}$ of the optimized plane (P_{opt}) within a spatial grid as expressed in the similar Equations 5.9,5.10. A linear normalization is applied on the altitude distance $d_{w/opt}$, then transformation into numerical intensity gray levels I_d, as expressed in Equation 5.11.

$$d_{w/opt} = \frac{|A_{opt}x_w + B_{opt}y_w + C_{opt}z_w + D_{opt}|}{\sqrt{A_{opt}^2 + B_{opt}^2 + C_{opt}^2}} \tag{5.9}$$

$$d_{w/opt} = z_w + h \tag{5.10}$$

$$I_d = \frac{d_{w/opt} - d_{\min}}{d_{\max} - d_{\min}} \times L_{gray} \tag{5.11}$$

Where x_w, y_w, z_w are the Cartesian coordinates of the 3D recalibrated ground points, $A_{opt}, B_{opt}, C_{opt}, D_{opt}$ are the parameters of the optimized plane (P_{opt}), $d_{\min}$ and $d_{\max}$ are the minimum and maximum values of the altitude distance $d_{w/opt}$ respectively, and $L_{gray} = 255$ is the maximum intensity gray level.

An improvement strategy is developed using the Inverse Distance Weighted IDW interpolation method [148], [149], in order to generalize the process case by adopting a dynamic size of the spatial grids that split the XY-plane as shown in Figure 5.18. Therefore, the non-linear interpolation derivations based on rectangular grid pattern assumption gains an advantage point in case of low azimuth or elevation angular resolution for LiDAR beams coverage situation. Where the horizontal and the vertical grid lengths H, V variate according to the distance distribution $\sigma_{d_{w/opt}}$ to obtain a high resolution georeferenced intensity image.

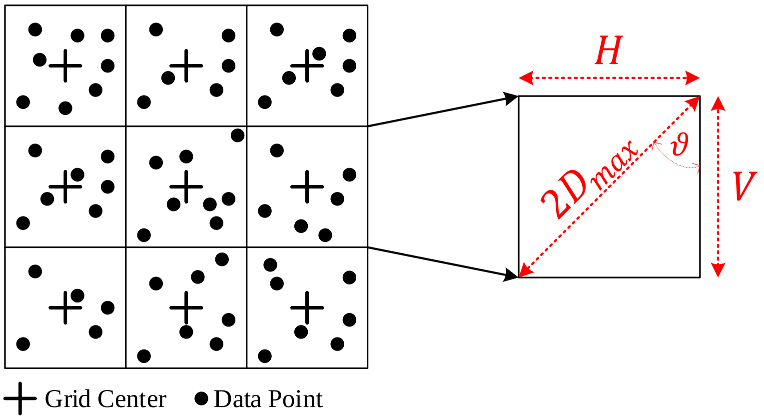

(a) Graphical grid model

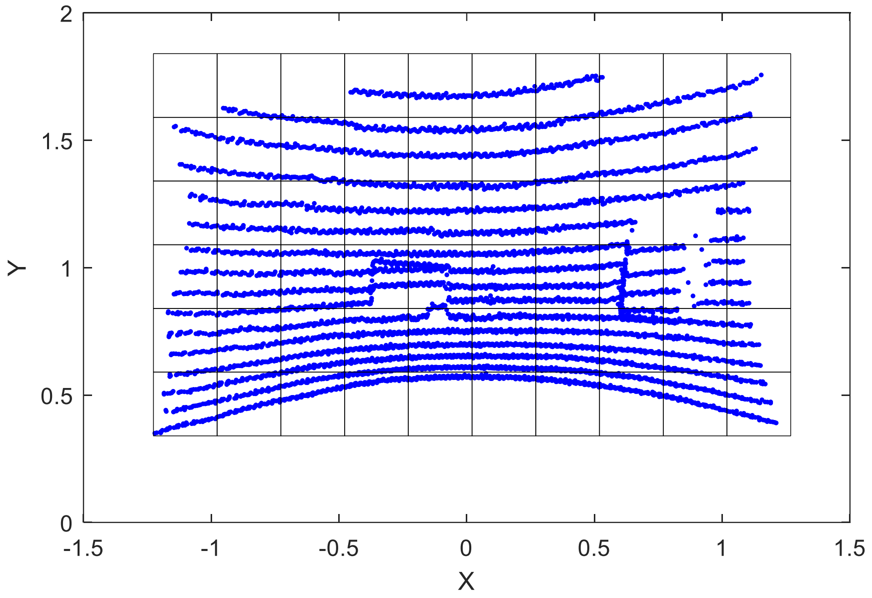

(b) Grid model of ground points for 2D frame

FIGURE 5.18: Grid model of ground surface point cloud

The intensity computation concept of georeferenced image pixels is based on two rules:

1. A point with a distance D farther away from the grid cell center gets a smaller weight.
2. A point with a larger altitude distance intensity I_d gets a greater weight.

According to the above rules, the intensity gray value of the grid cell (i, j), which is denoted by G_{ij} , is expressed as follows:

$$G^{ij} = \left(\sum_{k=1}^{n_{ij}} W^{k,ij} I_d^{k,ij}\right) \bigg/ \left(\sum_{k=1}^{n_{ij}} W^{k,ij}\right) \tag{5.12}$$

$$W^{k,ij} = aW_D^{k,ij} + bW_{I_d}^{k,ij} \tag{5.13}$$

$$a + b = 1 \tag{5.14}$$

Where n_{ij} is the number of data points within grid cell (i, j), $W^{k,ij}$ and $I_d^{k,ij}$ are the general weight and the altitude distance intensity of the k^{th} point within grid cell (i, j), respectively. a and b are the weight coefficients, $W_D^{k,ij}$ and $W_{I_d}^{k,ij}$ are the weight components calculated considering the planar Euclidean distance D from the grid cell center and the altitude distance intensity I_d within grid cell (i, j), respectively.

The planar Euclidean distance weight $W_D^{k,ij}$ is a non-linear normalized parameter, whose function within each grid cell (i, j) is to confirm the first interpolation rule: gain higher weights for the k^{th} points with a nearer planar Euclidean distance D to the grid cell center and vice versa as shown in Figure 5.19 and expressed in Equation 5.15. Where the initial assumption for grid's horizontal and vertical length parameters in Figure 5.19 are $H = 0.08m$ and $V = 0.08m$ respectively, then the maximum planar Euclidean distance $D_{\max}$ is expressed in Equation 5.17, where ϑ is the acute angle between the grid's vertical length V and the grid's diagonal $2D_{max}$. The grid cell size $H \times V$ must be large enough to cover the maximum Euclidean distance between each two elevation lasers, in order to avoid the empty grid cells especially in the defect zone. The role of this non-linear normalized weight $W_D^{k,ij}$ is to take into consideration the far planar Euclidean distance D values from the grid cell center, in order to be a sensitive weight at the rising or dropping defect edges.

$$W_D^{k,ij} = \frac{H^2 - \left(2D^{k,ij} \sin\left(\arctan\left(H/V\right)\right)\right)^2}{H^2\left(\left(D^{k,ij}\right)^2 + 1\right)} \tag{5.15}$$

$$D^{k,ij} = \sqrt{\left(x_w^{k,ij} - x_0^{ij}\right)^2 + \left(y_w^{k,ij} - y_0^{ij}\right)^2} \tag{5.16}$$

$$D_{\max} = \frac{H}{2\sin\left(\vartheta\right)} = \frac{H}{2\sin\left(\arctan\left(H/V\right)\right)} \tag{5.17}$$

Where $D^{k,ij}$ is the planar Euclidean distance between the points $\left(x_w^{k,ij}, y_w^{k,ij}\right)$ and $\left(x_0^{ij}, y_0^{ij}\right)$, which are the Cartesian coordinates of the k^{th} points and the grid cell center within grid cell (i, j) on the XY-plane.

In addition, the altitude distance intensity weight $W_{I_d}^{k,ij}$ is also a non-linear

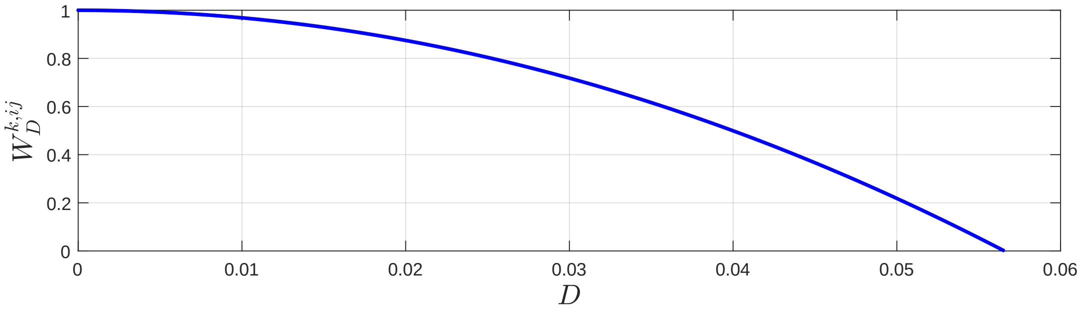

FIGURE 5.19: Planar Euclidean distance weight $W_D^{k,ij}$

normalized parameter, whose function within each grid cell (i, j) is to confirm the second interpolation rule: gain higher weights for the k^{th} points with a greater altitude distance intensity $I_d^{k,ij}$ and vice versa as shown in Figure 5.20 and expressed in Equations 5.18,5.19,5.20. Where the role of this non-linear normalization weight $W_{I_d}^{k,ij}$ is to mitigate the low altitude distance intensity $I_d^{k,ij}$ values.

$$W_{I_d}^{k,ij} = W_{I_1}^{k,ij} \cdot W_{I_2}^{k,ij} \tag{5.18}$$

$$W_{I_1}^{k,ij} = \frac{2\left(I_d^{k,ij} - g_{\min}^{ij}\right)^2}{\left(I_d^{k,ij} - g_{\min}^{ij}\right)^2 + \left(g_{\max}^{ij} - g_{\min}^{ij}\right)^2} \tag{5.19}$$

$$W_{I_2}^{k,ij} = \frac{2\left(I_d^{k,ij} - I_{\min}\right)^2}{\left(I_d^{k,ij} - I_{\min}\right)^2 + (I_{\max} - I_{\min})^2} \tag{5.20}$$

where $W_{I_1}^{k,ij}$ and $W_{I_2}^{k,ij}$ are the weight components calculated based on the local and the global altitude distance intensity information respectively, $g_{\max}$ and $g_{\min}$ are the local maximal and minimal altitude distance intensities values within grid cell (i, j), and $I_{\max}$ and $I_{\min}$ are the global maximal and minimal altitude distance intensities values of the point cloud frame.

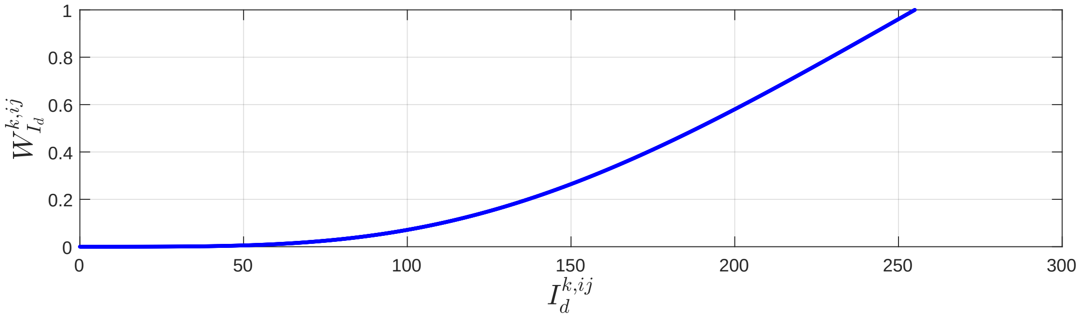

FIGURE 5.20: Altitude distance intensity weight $W_{I_d}^{k,ij}$

In order to attain a high resolution georeferenced image, a Grid Splitting Algorithm GSA is developed based on the standard deviation of the distance distribution $\sigma_{d_{w/opt}}$ constraint for each grid cell (i,j), as explained in Algorithm 4 that performed on Figure 5.21.

Algorithm 4: Grid Splitting Algorithm

```
Input: Altitude distance $d_{w/opt}$, initial horizontal and vertical lengths
       values $H, V$ respectively, and the Cartesian coordinates $x_w, y_w, z_w$
       of the $k^{th}$ points within a grid cell $(i,j)$
Output: Georeferenced gray image $G^{ij}$
1 If the grid cell is empty, associate the intensity gray value $G^{ij}$ to zero.
    Else, compute the distance distribution $\sigma_{d_{w/opt}}$ of the $k^{th}$ points within a
    grid cell $(i,j)$ as expressed below:
    $\sigma_{d_{w/opt}} = \sqrt{\frac{1}{N}\sum_{k=1}^{n_{ij}}(d_{w/opt} - \overline{d_{w/opt}})^2}$
2 If the standard deviation of the distance distribution $\sigma_{d_{w/opt}} \geq \sigma_{th}$, split
    the grid cell into four sub-grids in case if all of the sub-grids are not
    empty, by dividing the horizontal and vertical lengths by two $H/2, V/2$
    respectively as shown in Figure 5.22a. Where $\sigma_{th} \simeq 1.5cm$ is a constant
    threshold that defines the maximum distance accuracy for the lasers
    impact of the LiDAR sensor on a flat plane. Then, go to step 1.
    Else, compute the intensity gray value $G^{ij}$ using the above proposed
    inverse distance weighted interpolation method.
3 Split the grid cells into sub-grid cells according to the smallest grid cell
    size, and associate the intensity gray values of the sub-grid cells equal
    to the original grid cell's intensity gray value as shown in Figure 5.22b.
```

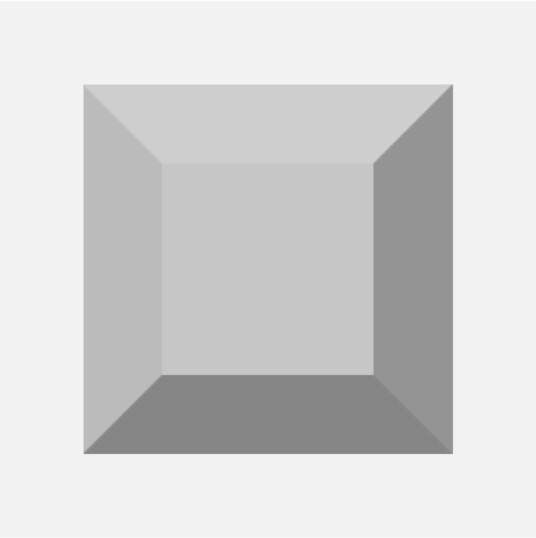

FIGURE 5.21: Graphical sample for road defect

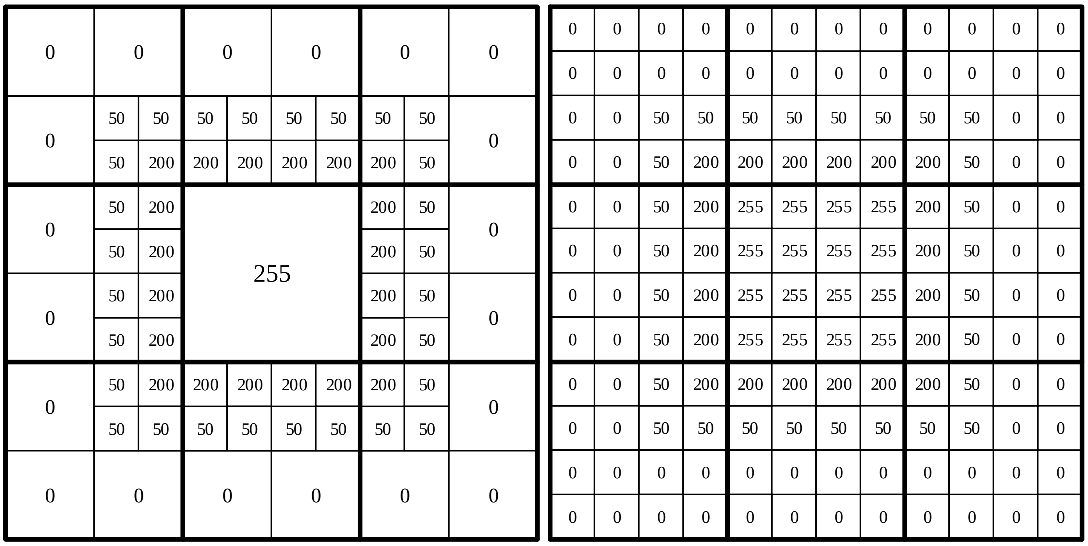

0		0		0		0		0		0	
0		50	50	50	50	50	50	50	50	0	
		50	200	200	200	200	200	200	50		
0		50	200	255				200	50	0	
		50	200					200	50		
0		50	200					200	50	0	
		50	200					200	50		
0		50	200	200	200	200	200	200	50	0	
		50	50	50	50	50	50	50	50		
0		0		0		0		0		0	

(a) 1st and 2nd steps of GSA result

0	0	0	0	0	0	0	0	0	0	0	0
0	0	0	0	0	0	0	0	0	0	0	0
0	0	50	50	50	50	50	50	50	50	0	0
0	0	50	200	200	200	200	200	200	50	0	0
0	0	50	200	255	255	255	255	200	50	0	0
0	0	50	200	255	255	255	255	200	50	0	0
0	0	50	200	255	255	255	255	200	50	0	0
0	0	50	200	255	255	255	255	200	50	0	0
0	0	50	200	200	200	200	200	200	50	0	0
0	0	50	50	50	50	50	50	50	50	0	0
0	0	0	0	0	0	0	0	0	0	0	0
0	0	0	0	0	0	0	0	0	0	0	0

(b) 3rd step of GSA result

FIGURE 5.22: High resolution gray image using GSA

A high resolution generated georeferenced gray image is shown in Figure 5.23a, using the proposed improved inverse distance weighted interpolation method with grid splitting algorithm. Then, Otsu segmentation method [115] is performed on the georeferenced gray image, in order to transform it to a binary image as shown in Figure 5.23b.

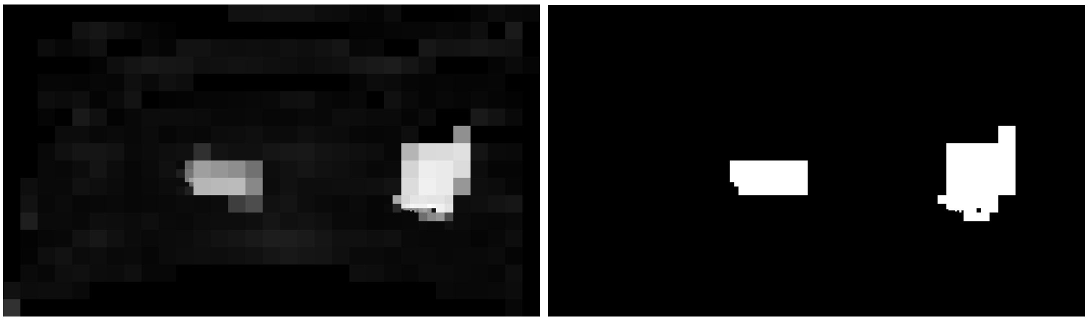

(a) High resolution gray image (b) High resolution binary image

FIGURE 5.23: High resolution georeferenced images

5.5 Experimental Results

In this section, the proposed feature-based and grid-based defect detection methods are applied on real data acquisition from the Velodyne VLP-16 LiDAR sensor as shown in Figure 5.24. The most important features of Velodyne VLP-16 LiDAR are shown in Table 5.1.

FIGURE 5.24: Acquisition of hump and pothole defects

TABLE 5.1: VLP-16 Features

Features	**VLP-16**
Laser beams	16
Horizontal FOV	360°
Vertical FOV	$-15^\circ \rightarrow +15^\circ$
Azimuth angular resolution	0.1° - 0.2° - 0.4°
Elevation angular resolution	2°
Range accuracy σ_ρ	$3cm$

5.5.1 Evaluation Parameters

There exist multiple performance evaluation metrics that are related to detection process. Four widely used metrics are *Accuracy*, *Precision*, *Recall*, and *F-measure* [108]. To clearly explain them, we consider having two classes, a presence class and a absence class to build the confusion matrix. It holds the four different combinations of predicted and actual values of these two classes as can be seen in Figure 5.25.

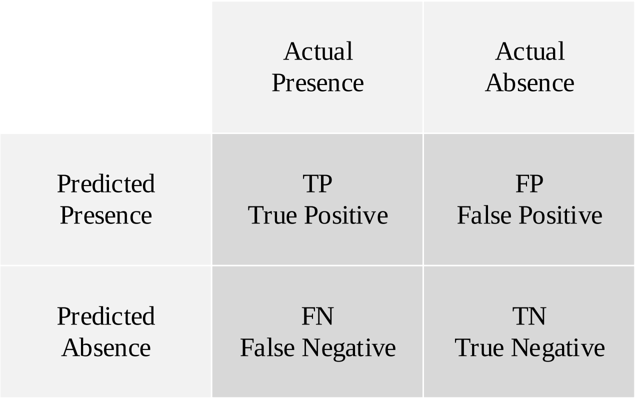

	Actual Presence	Actual Absence
Predicted Presence	TP True Positive	FP False Positive
Predicted Absence	FN False Negative	TN True Negative

FIGURE 5.25: The confusion matrix of four different combinations of predicted and actual class values

- True Positives TP: the total number of correct predictions that are presence, which means, were predicted to be presence knowing that they actually belong to the presence class.
- False Positives FP: the total number of incorrect predictions that are presence, which means, were predicted to be presence knowing that they actually belong to the absence class.
- True Negative TN: the total number of correct predictions that are absence, which means, were predicted to be absence knowing that they actually belong to the absence class.
- False Negative FN: the total number of incorrect predictions that are absence, which means, were predicted to be absence knowing that they really belong to the presence class.
- *Accuracy*: a well-known evaluation metric defined as a percentage of correct predictions as expressed in Equation 5.21. Thus, it evaluates how many defects and non-defects classes are correctly detected.

$$Accuracy = \frac{TP + TN}{TP + TN + FP + FN} \tag{5.21}$$

- *Precision* and *Recall*: another two well-known evaluation metrics usually used together and can be applied in the context of detection. *Precision*, also called Positive Predictive Value PPV, answers the question of what proportion of positive predictions was actually correct. Whereas, *Recall*, also called True Positive Rate TPR, answers the question of what proportion of actual positives was identified correctly.

$$Precision = \frac{TP}{TP + FP} \tag{5.22}$$

$$Recall = \frac{TP}{TP + FN} \tag{5.23}$$

- *F-measure*: another popular evaluation parameter used to compare between detection and classification methods. *F-measure*, also called *F-score*, is a single score that balances both the concerns of *Precision* and *Recall* in one number. In other words, *F-measure* defines the harmonic mean of the *Precision* and *Recall* metrics as expressed in Equation 5.24.

$$\begin{aligned} F\text{-}measure &= 2\frac{Precision \times Recall}{Precision + Recall} \\ &= \frac{2TP}{2TP + FP + FN} \end{aligned} \tag{5.24}$$

5.5.2 Experimental Setups

The detection methods FBDDM and GBDDM are performed on several real data acquisitions with various experimental scenarios. The experiments take place in the laboratory, which include a flat ground with size $2.5 \times 1.8m^2$ $(l \times w)$, the height of right edge is $> 1m$, the height of left edge is $\simeq 20cm$, the size of the hump defect is $7.5 \times 30.5 \times 22cm^3$ $(h \times l \times w)$ and the size of the pothole defect is $7.5 \times 30.5 \times 22cm^3$ $(h \times l \times w)$:

- Acquisition 1: provides a recording frames of empty defects.
- Acquisition 2: provides a recording frames of hump defect, moving in vertically direction at the middle of the road.
- Acquisition 3: provides a recording frames of hump defect, moving in obliquely direction from top right to bottom left, to cross the road from right to left side.
- Acquisition 4: provides a recording frames of fixed pothole defect at the middle of the road.
- Acquisition 5: provides a recording frames of fixed pothole defect at the bottom of the road.
- Acquisition 6 and 7: provides a recording frames of moving pothole defect in vertically direction at the middle of the road, with low LiDAR bounce, variation of orientation and altitude of pitch angle ϕ_x and height h respectively.
- Acquisition 8: provides a recording frames of multi-defects, fixed pothole defect at the middle of the road, and moving hump defect in vertically direction at the right side near to road edge.

- Acquisition 9: provides a recording frames of moving pothole defect in vertically direction at the middle of the road, with high LiDAR bounce, variation of orientation and altitude of pitch angle ϕ_x and height h respectively.

In some acquisitions, the hump defect is attached to a thin thread and pulled to achieve the defect movement. Where in other acquisitions, the motion of pothole defect is due to the movement of LiDAR sensor using a long stand tilt unit. The movement of the LiDAR sensor takes advantage to describe the bounce of the vehicle in a perfect realistic experiment, which performs a variation of LiDAR sensor height.

5.5.3 Confusion Metrics Results

The confusion metrics results take place on the above different acquisition scenarios as shown in Tables 5.2,5.3,5.4. Where the confusion matrix result of FBDDM in Table 5.2 is for the primary feature-based defect detection method results before the recalibration process, and the confusion matrix result of opt-FBDDM in Table 5.3 is for the optimized feature-based defect detection method after the recalibration process.

In FBDDM method, the TP, TN, FP, FN values are computed depending on the counted concavity peaks pk_i that confirm the constraints in the instantaneous differential Gaussian algorithm compared to the actual presence and absence defect number using VeloView software. However in GBDDM method, the TP, TN, FP, FN values are computed depending on the counted labels using 8-connected objects [150] compared to the actual presence and absence defect number using VeloView software. The FP, FN values exist because of the three reasons:

- Un-complete calibration for FBDDM method, then it is solved by recalibration process for opt-FBDDM method.
- The position of the defect when it is very close to the road edge, which leads to a low coverage resolution.
- The movement of the defect when it starts to cross the laser, which shows a low coverage altitude.

Referring to the confusion metrics total number of each table, the total numbers of FBDDM are greater than the total numbers of GBDDM. Because, the FBDDM detection process deals with each elevation laser per frame, where the method operations developed on a laser as a one input object, so in each frame there exists some lasers including defects and the rest of them are empty of defects. While, the GBDDM detection process deals with all lasers simultaneously, so the method operations developed on a frame as a one input object.

TABLE 5.2: Confusion matrix of FBDDM for each acquisition

FBDDM	TP	TN	FP	FN	Frames
Acquisition 1	0	1664	0	0	104
Acquisition 2	166	1407	8	10	99
Acquisition 3	211	1006	12	30	78
Acquisition 4	254	1778	0	0	127
Acquisition 5	376	1128	0	0	94
Acquisition 6	88	306	4	5	25
Acquisition 7	167	350	4	10	33
Acquisition 8	472	912	0	39	86
Acquisition 9	96	255	13	1	22
Total	**1830**	**8806**	**40**	**95**	**668**

TABLE 5.3: Confusion matrix of opt-FBDDM for each acquisition

opt-FBDDM	TP	TN	FP	FN	Frames
Acquisition 1	0	1664	0	0	104
Acquisition 2	167	1408	0	9	99
Acquisition 3	214	1005	6	27	78
Acquisition 4	254	1778	0	0	127
Acquisition 5	376	1128	0	0	94
Acquisition 6	88	306	1	5	25
Acquisition 7	167	350	1	10	33
Acquisition 8	481	912	0	30	86
Acquisition 9	96	255	0	1	22
Total	**1843**	**8806**	**8**	**82**	**668**

TABLE 5.4: Confusion matrix of GBDDM for each acquisition

GBDDM	TP	TN	FP	FN	Frames
Acquisition 1	0	104	0	0	104
Acquisition 2	33	66	0	0	99
Acquisition 3	41	36	2	0	78
Acquisition 4	127	0	3	0	127
Acquisition 5	94	0	4	0	94
Acquisition 6	25	0	1	0	25
Acquisition 7	33	0	3	0	33
Acquisition 8	144	0	3	0	86
Acquisition 9	22	0	1	0	22
Total	**519**	**206**	**17**	**0**	**668**

5.5.4 Evaluation Terms Results Analysis

The Table 5.5 shows the experimental comparative evaluation of FBDDM, opt-FBDDM and GBDDM methods. To analyze the FBDDM and opt-FBDDM results, the opt-FBDDM shows higher performance among FBDDM in terms of *Accuracy*, *Precision*, *Recall* and *F-measure*, which indicates that the recalibration process is important to enhance and improve the results of the feature-based defect detection method.

TABLE 5.5: Evaluation results of our proposed methods

Method	Accuracy	Precision	Recall	F-measure
FBDDM	98.74%	97.86%	95.06%	**96.44%**
opt-FBDDM	99.16%	99.56%	95.74%	**97.61%**
GBDDM	97.70%	96.82%	100%	**98.38%**

In addition, the opt-FBDDM shows higher *Accuracy* compared with GBDDM but *Accuracy* is not enough to compare between both methods, because it takes into consideration the true negative TN factor. However, the better valuable parameters are *Precision* and *Recall*, because they depend on false positive FP and false negative FN factors respectively, to describe the positive predictive value and the true positive rate respectively.

Moreover, the opt-FBDDM shows a higher *Precision* compared to the GBDDM, while the GBDDM shows a higher *Recall* compared to the opt-FBDDM. Therefore, the most valuable and popular evaluation term is *F-measure*, because it represents both *Precision* and *Recall* terms in one single term. So, the GBDDM shows a higher performance in term of *F-measure* compared to the opt-FBDDM. This indicates and proves that the grid-based defect detection method provides better efficiency and performance against the optimized feature-based defect detection method.

Both optimized feature-based defect detection method and grid-based defect detection method show high performance results, which indicate their importance for road defect detection. However, the feature-based method provides **detection and identification** of road defects, while grid-based method provides **detection, visualization and localization** of road defects.

5.5.5 Evaluation Methods Comparison Results

According to the mentioned methods in Table 5.6, our proposed methods is compared with two defect detection methods. The first method is LiDAR-Histogram [107] used the benchmark KITTI-ROAD data-set [108], which includes 3D high resolution LiDAR sensor Velodyne HDL-64E, cameras, GPS and IMU. The LiDAR-Histogram method detects huge size of positive and negative obstacles as like as vehicle and very large pothole respectively, as shown in Figure 5.26. The second method is Cascade System [111] used a personal acquisition recorded from 2D LiDAR sensor Lite v1 and camera ODROID-XU4. The Cascade System method detects normal size of pothole and speed hump. According to the quantitative results in Table 5.6, the *F-measure*, *Precision* and *Recall* evaluation performances of our method rank first among all the methods. In addition, the results are very promising considering that we use a single cylindrical 3D LiDAR sensor Velodyne VLP-16 without extra sensors, where Velodyne VLP-16 is a low resolution LiDAR compared with Velodyne HDL-64E (see Appendix A.1). In addition, our proposed methods gain an advantage to detect a very small size of potholes and humps compared with the large potholes, speed humps and obstacles sizes in [107], [111]. It can be regarded as the baseline for the feature and grid based methods.

Remark: Table 5.6 represents a first attempt to compare our proposed defect detection methods FBDDM and GBDDM that are developed for cylindrical LiDARs (Velodyne Puck, Ouster OS1) with other popular defect detection methods that are developed for non-cylindrical LiDARs (Velodyne HDL). We will work later on an extension of our proposed methods to deal with these kind of LiDARs (Velodyne HDL) in order to propose a more satisfactory comparison with KITTI-ROAD data-set.

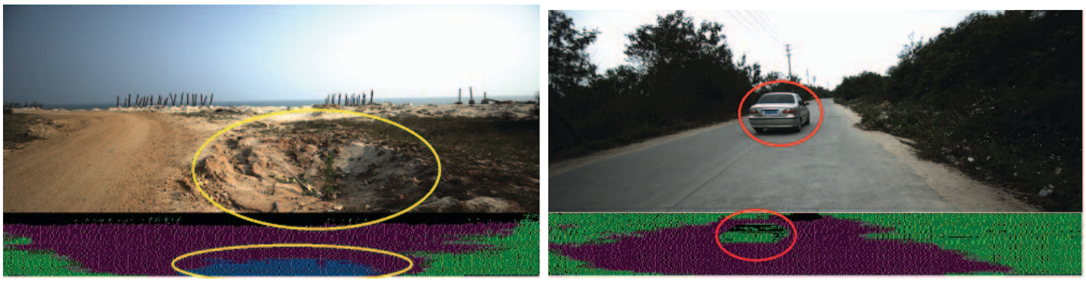

(a) Pothole detection (b) Vehicle detection

FIGURE 5.26: Positive and negative obstacle detection [107]

TABLE 5.6: Evaluation comparison results with other methods

Method	Precision	Recall	F-measure	Run-time	Environment
GBDDM	96.82%	100%	**98.38%**	0.09s	1 core @ 2.8Ghz (Matlab)
FBDDM	99.56%	95.74%	**97.61%**	0.48s	1 core @ 2.8Ghz (Matlab)
LiDAR-Histogram [107]	95.39%	91.34%	**93.32%**	0.1s	1 core @ 2.5Ghz (C/C++)
Cascaded System [111]	76.98%	76.33%	**76.66%**		

5.6 Conclusion

In this chapter, two defect detection methods are presented. The Feature-Based Defect Detection Method FBDDM, where the solution relies on calibration process, that provides a horizontal and understandable ground, in order to study the concavity feature by second order of Differential Gaussian Filter *DGF*2, to detect various homogeneous road defects. In addition, the Grid-Based Defect Detection Method GBDDM relies also on the calibration process, in order to study the altitude distance, using improved Inverse

Distance Weighted IDW interpolation method and Grid Splitting Algorithm GSA, to detect, visualize and localize the defects in a high resolution georeferenced image. The results show a compromised performance and impressive efficiency of our proposed defect detection methods, in terms of *Accuracy*, *Precision*, *Recall* and *F-measure* compared with other detection methods, proving the detection ability of potholes and humps defects using real data.

Conclusion and Perspectives

As a part of transportation and driver assistance systems framework, our contribution concerns multi-defect detection from distributed 3D telemetry measurements. We have developed and validated various global methods, that are compatible with any cylindrical 3D LiDAR sensors. These have been applied to of 3D LiDAR perception system mounted and centered on the vehicle backward. Indeed, the LiDAR sensor is rotated toward the ground in order to increase the road coverage resolution, which improves the road defect detection process. Therefore, the calibration process was adopted in order to transform the LiDAR frame into a global reference frame, thus modifying the LiDAR frame into an understandable view scene.

The development and improvement of a novel flexible extrinsic LiDAR/ Ground Calibration Method LGCM was the starting point of this thesis. The calibration method is relied on ground plane-based modeling, to estimate the 4-DOF extrinsic parameters: height and 3D orientation. Moreover, the calibration process is built on four main aspects: linear model Least Squares estimator, Rodrigues formula, Least Squares Conic Algorithm and Levenberg-Marquardt optimization algorithm. The results show a significant performance in terms of precision and robustness against the variation of LiDAR's orientation and range accuracy respectively, proving the stability and the accuracy of the proposed calibration method on synthetic and real data. This reflects the global good capability of this calibration method when applied on cylindrical LiDAR sensors under difficult experimental conditions.

In addition, we proposed and developed two novel road defect detection methods in the context of this thesis, where the solution of these two detection method relies on the calibration method, that provides a horizontal and understandable ground view. First, the Feature-Based Defect Detection Method FBDDM, that studies the concavity feature on each elevation laser using second order Differential Gaussian Filter, to detect multi homogeneous road defects. The recalibration process has imposed itself to enhance the false alarm, in order to improve the evaluation results of the Feature-Based Defect Detection Method. Second, the Grid-Based Defect Detection Method GBDDM that relies on two main aspects: improved Inverse Distance Weighted interpolation method and Grid Splitting Algorithm, to detect, visualize and localize the multi homogeneous road defects in a high resolution georeferenced image. The evaluation results show a compromised performance and impressive efficiency of our proposed defect detection methods, in terms of accuracy, precision and recall against other defect detection methods, proving the detection ability of potholes and humps defects using real data.

Based on the outcomes presented in this thesis, we highlight several interesting future research directions:

- In our work, the detection methods is applied on road defects (potholes and humps). It will be an interesting application to apply the same methods on vehicles, obstacles and pedestrians detection. More than that, modify the grid-based defect detection method to detect the water hazards using the reflectivity LiDAR feature.
- Using a high resolution LiDAR like OS1-128 LiDAR sensor will increase the performance of calibration and detection processes. But, it will also increase the chance of defect size estimation challenge.
- In road selection points process, the road looses a small spatial regions at the edge of the road. So, we suggest to develop a road detection method to study the defects that are aligned beside the road edges.
- We recommend a LiDAR and Camera fusion sensors to increase the performance of the proposed detection methods, especially the grid-based defect detection method.
- In addition, the fusion of LiDAR, Global Positioning System GPS and Inertial Measurement Unit IMU will support a defect tracking, localization and mapping system in a global world wide reference.
- Moreover, the proposed calibration and detection methods are compatible with cylindrical LiDARs. It will be interesting to find a way to modify the methods process to be compatible with non cylindrical LiDARs like Velodyne HDL-64 LiDAR sensor. So, the methods can be directly applied on the KITTI-ROAD data-set to compare perfectly with other methods.
- Finally, the most interesting challenge is to implement the methods on a Digital Signal Processor DSP as a real-time application.

Appendix A

Velodyne Product Sensors

A.1 Velodyne Products Features

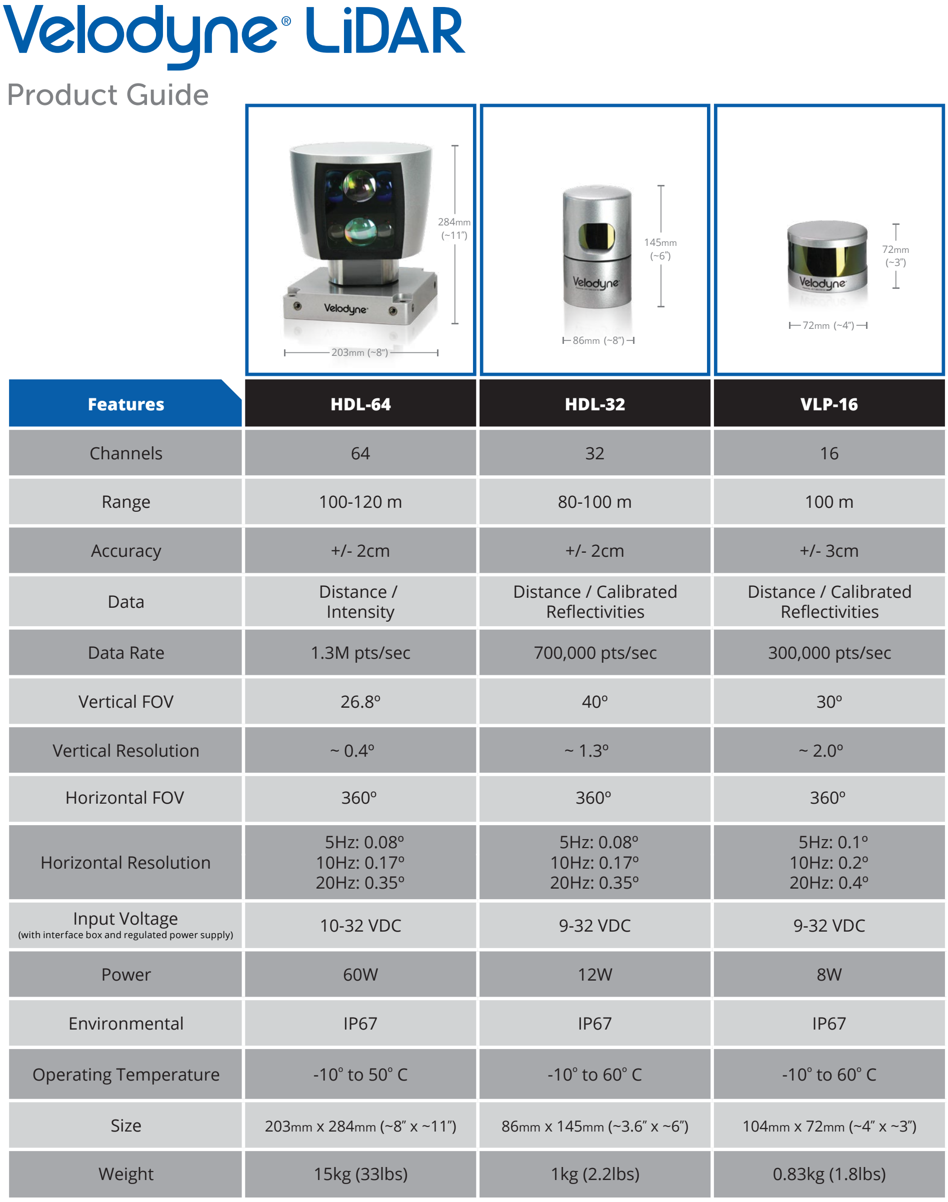
Velodyne® LiDAR
Product Guide

Features	HDL-64	HDL-32	VLP-16
Channels	64	32	16
Range	100-120 m	80-100 m	100 m
Accuracy	+/- 2cm	+/- 2cm	+/- 3cm
Data	Distance / Intensity	Distance / Calibrated Reflectivities	Distance / Calibrated Reflectivities
Data Rate	1.3M pts/sec	700,000 pts/sec	300,000 pts/sec
Vertical FOV	26.8º	40º	30º
Vertical Resolution	~ 0.4º	~ 1.3º	~ 2.0º
Horizontal FOV	360º	360º	360º
Horizontal Resolution	5Hz: 0.08º 10Hz: 0.17º 20Hz: 0.35º	5Hz: 0.08º 10Hz: 0.17º 20Hz: 0.35º	5Hz: 0.1º 10Hz: 0.2º 20Hz: 0.4º
Input Voltage (with interface box and regulated power supply)	10-32 VDC	9-32 VDC	9-32 VDC
Power	60W	12W	8W
Environmental	IP67	IP67	IP67
Operating Temperature	-10° to 50° C	-10° to 60° C	-10° to 60° C
Size	203mm x 284mm (~8″ x ~11″)	86mm x 145mm (~3.6″ x ~6″)	104mm x 72mm (~4″ x ~3″)
Weight	15kg (33lbs)	1kg (2.2lbs)	0.83kg (1.8lbs)

FIGURE A.1: Some of Velodyne Products Features [138]

A.2 VLP-16 Packet Structure

Every model of LiDAR sensor has its own packet structure in which the data is being sent to the user. For the Velodyne LiDARs, the information is effectively packed to save bandwidth of a communication line, as every point within a packet does not contain its full description and shares some parameters with other grouped points. According to the supplied packet's structure and timing information, we can retrieve every single record of a point without any loss of precision. Packet's structure is shown in Figure A.2.

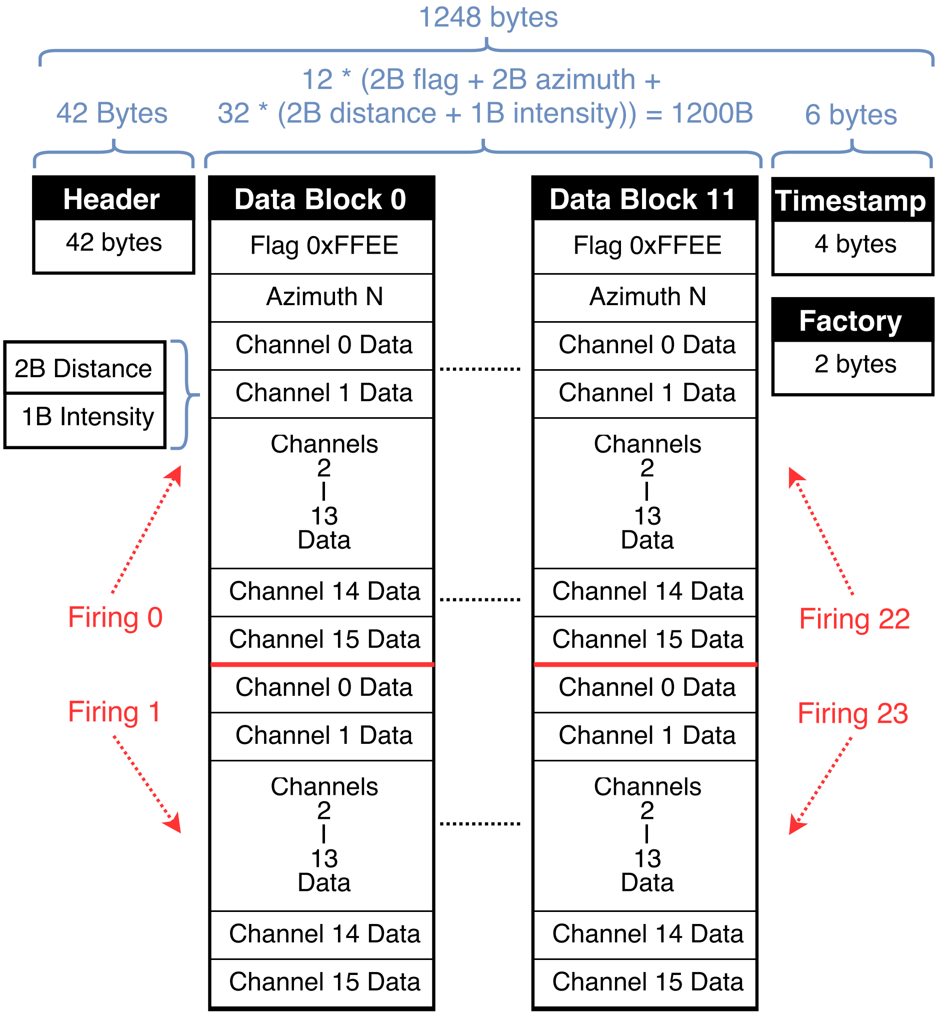

FIGURE A.2: VLP-16 Packet Structure [138]

- **Data Point**: 3 bytes from a single firing from a laser.
  - 2 bytes of distance.
  - 1 byte of calibrated reflectivity.
- **Data Block**: (100 bytes).
  - 2 bytes flag ($0 \times FFEE$).
  - 2 bytes azimuth.

  - 96 bytes for 32 Data Points.
- **Data Packet**:
  - 42 bytes of header.
  - 12 Data Blocks.
  - 4 bytes timestamp
  - 2 byte factory field.

Appendix B

Graphical Clarifications

B.1 Additive distinguish noise

The additive distinguish noise $w_\rho, w_\alpha, w_\beta$ to each of range, azimuth, and elevation ρ, α, β respectively are shown in the Figure B.1, and expressed in the below Equation B.1.

$$(c_w) : \begin{bmatrix} \rho_w \\ \alpha_w \\ \beta_w \end{bmatrix} = \begin{bmatrix} \rho + w_\rho \\ \alpha + w_\alpha \\ \beta + w_\beta \end{bmatrix} \tag{B.1}$$

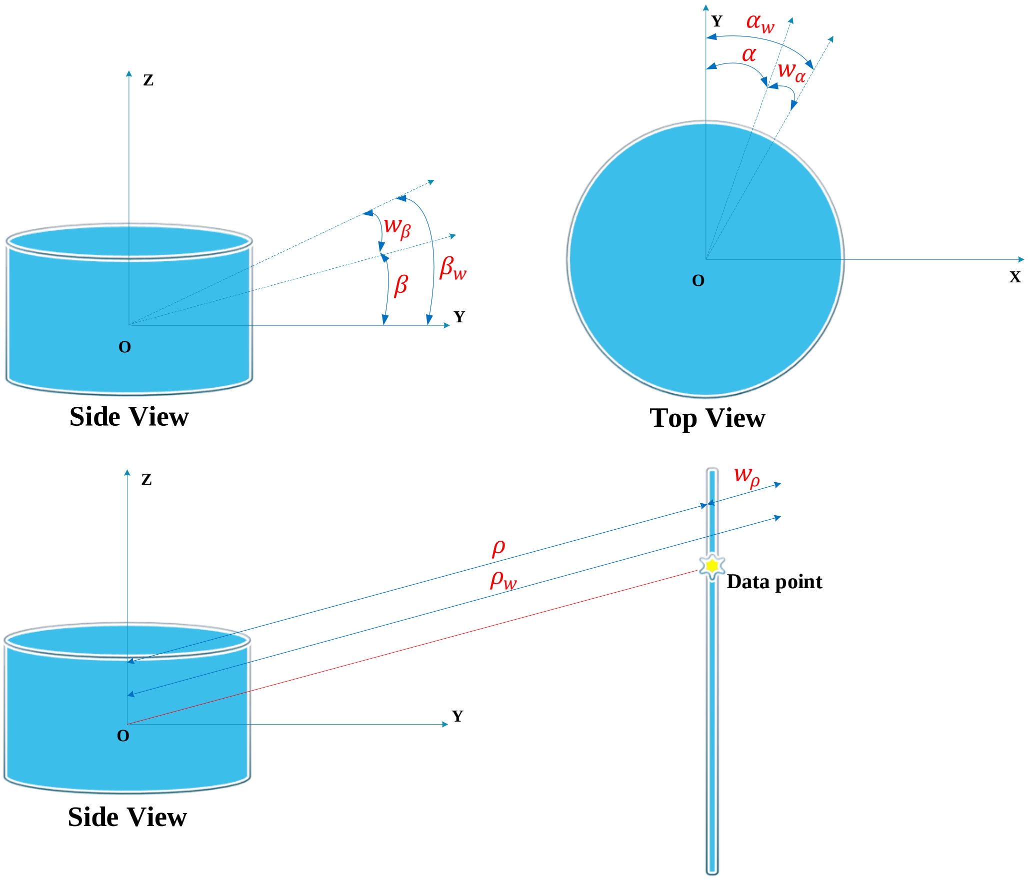

FIGURE B.1: Data PointCloud features with noise

B.2 Rotation and Translation Transformation for LiDAR Frame

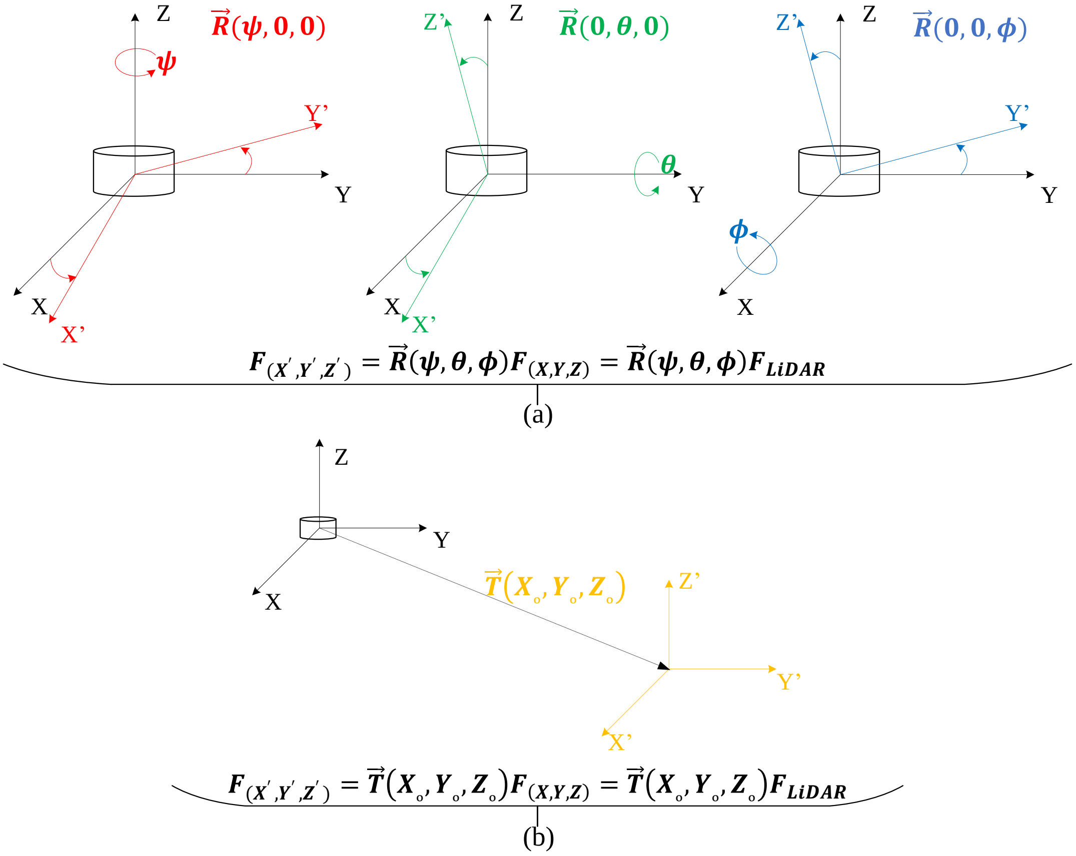

FIGURE B.2: Data PointCloud features with noise

Bibliography

[1] M. Chan, "Global status report on road safety 2015: Report," *Geneva: World Health Organization*, 2015. [Online]. Available: https://www.who.int/violence_injury_prevention/road_safety_status/2015/en/.

[2] E. Choueiri, G. Choueiri, and B. Choueiri, "Road safety in lebanon: Magnitude, cost and potential countermeasures," *Advances in transportation studies*, vol. 35, pp. 73–88, Jan. 2015.

[3] "Global status report on road safety 2018: Summary," *Geneva: World Health Organization*, 2018. [Online]. Available: https://www.who.int/publications-detail/global-status-report-on-road-safety-2018.

[4] *World Health Organization (WHO) Injuries, Traffic*, [Online]. Available: https://www.who.int/health-topics/road-safety#tab=tab_1.

[5] G. A. Roth, D. Abate, K. H. Abate, *et al.*, "Global, regional, and national age-sex-specific mortality for 282 causes of death in 195 countries and territories, 1980-2017: A systematic analysis for the global burden of disease study 2017," *The Lancet*, vol. 392, no. 10159, pp. 1736–1788, Nov. 2018, ISSN: 0140-6736. DOI: 10.1016/s0140-6736(18)32203-7. [Online]. Available: https://doi.org/10.1016/S0140-6736(18)32203-7.

[6] E. G. Krug, G. K. Sharma, and R. Lozano, "The global burden of injuries," *American Journal of Public Health*, vol. 90, no. 4, pp. 523–526, 2000, PMID: 10754963. DOI: 10.2105/AJPH.90.4.523. eprint: https://doi.org/10.2105/AJPH.90.4.523. [Online]. Available: https://doi.org/10.2105/AJPH.90.4.523.

[7] *World Health Organization (WHO) Road Traffic Injuries RTI*, [Online]. Available: https://www.who.int/news-room/fact-sheets/detail/road-traffic-injuries.

[8] *Global Plan for the Decade of Action for Road Safety 2011-2020*, [Online]. Available: https://www.who.int/roadsafety/decade_of_action/plan/en/.

[9] *Transforming our world: the 2030 Agenda for Sustainable Development*, [Online]. Available: https://sustainabledevelopment.un.org/post2015/transformingourworld.

[10] K. Bengler, K. Dietmayer, B. Farber, M. Maurer, C. Stiller, and H. Winner, "Three decades of driver assistance systems: Review and future perspectives," *IEEE Intelligent Transportation Systems Magazine*, vol. 6, no. 4, pp. 6–22, 2014.

[11] M. A. Zaiter, R. Lherbier, G. Faour, O. Bazzi, and J. C. Noyer, "3d lidar extrinsic calibration method using ground plane model estimation," in *2019 IEEE International Conference on Connected Vehicles and Expo (ICCVE)*, Nov. 2019, pp. 1–6. DOI: `10.1109/ICCVE45908.2019.8964949`.

[12] M. A. Zaiter, R. Lherbier, G. Faour, O. Bazzi, and J.-C. Noyer, "Extrinsic lidar/ground calibration method using 3d geometrical plane-based estimation," *Sensors*, vol. 20, no. 10, May 2020, ISSN: 1424-8220. DOI: `10.3390/s20102841`. [Online]. Available: `https://www.mdpi.com/1424-8220/20/10/2841`.

[13] J. Morales, J. L. Martínez, A. Mandow, A. J. Reina, A. Pequeño-Boter, and A. García-Cerezo, "Boresight calibration of construction misalignments for 3d scanners built with a 2d laser rangefinder rotating on its optical center," *Sensors*, vol. 14, no. 11, pp. 20 025–20 040, Oct. 2014, ISSN: 1424-8220. DOI: `10.3390/s141120025`. [Online]. Available: `https://www.mdpi.com/1424-8220/14/11/20025`.

[14] G. Zhe, H. Jun, Y. Xiaofei, and A. Ping, "Calibration of rotating 2d lidar based on simple plane measurement," *Sensor Review*, vol. 39, no. 2, pp. 190–198, Jan. 2019, ISSN: 0260-2288. DOI: `10.1108/SR-11-2017-0237`. [Online]. Available: `https://doi.org/10.1108/SR-11-2017-0237`.

[15] R. Thakur, "Scanning lidar in advanced driver assistance systems and beyond: Building a road map for next-generation lidar technology," *IEEE Consumer Electronics Magazine*, vol. 5, no. 3, pp. 48–54, 2016.

[16] X. Mosquet, M. Andersen, and A. Arora, "A roadmap to safer driving through advanced driver assistance systems," *Auto Tech Review*, vol. 5, no. 7, pp. 20–25, 2016, ISSN: 2347-9434. [Online]. Available: `https://doi.org/10.1365/s40112-016-1164-1`.

[17] S.-Y. Kim, J.-K. Kang, S.-Y. Oh, *et al.*, "An intelligent and integrated driver assistance system for increased safety and convenience based on all-around sensing," *Journal of Intelligent and Robotic Systems*, vol. 51, no. 3, pp. 261–287, 2008, ISSN: 1573-0409. [Online]. Available: `https://doi.org/10.1007/s10846-007-9187-0`.

[18] I. J. Xique, W. Buller, Z. B. Fard, E. Dennis, and B. Hart, "Evaluating complementary strengths and weaknesses of adas sensors," in *2018 IEEE 88th Vehicular Technology Conference (VTC-Fall)*, 2018, pp. 1–5.

[19] V. Hoang, D. C. Hernández, M. Le, and K. Jo, "3d motion estimation based on pitch and azimuth from respective camera and laser rangefinder sensing," in *2013 IEEE/RSJ International Conference on Intelligent Robots and Systems*, Nov. 2013, pp. 735–740. DOI: `10.1109/IROS.2013.6696433`.

[20] L. Wei, C. Cappelle, and Y. Ruichek, "Localization of intelligent ground vehicles in outdoor urban environments using stereovision and gps integration," in *2011 15th International Conference on Advanced Robotics (ICAR)*, Jun. 2011, pp. 192–197. DOI: `10.1109/ICAR.2011.6088617`.

[21] S. Yu, H. Huang, Y. Liu, Y. Hu, and H. Gu, "A low-complexity autonomous 3d localization method for unmanned aerial vehicles by

binocular stereovision technology," in *2018 10th International Conference on Intelligent Human-Machine Systems and Cybernetics (IHMSC)*, vol. 01, Aug. 2018, pp. 344–347. DOI: 10.1109/IHMSC.2018.00086.

[22] P. Xuan Hau and J. Jung, "Recommendation system based on multilingual entity matching on linked open data," *Journal of Intelligent and Fuzzy Systems*, vol. 27, pp. 589–599, Jan. 2014.

[23] A. Uckermann, R. Haschke, and H. Ritter, "Realtime 3d segmentation for human-robot interaction," in *2013 IEEE/RSJ International Conference on Intelligent Robots and Systems*, Nov. 2013, pp. 2136–2143. DOI: 10.1109/IROS.2013.6696655.

[24] C. Golban and S. Nedevschi, "Moving rigid objects segmentation in 3d dynamic traffic scenes using a stereovision system," in *2014 IEEE 10th International Conference on Intelligent Computer Communication and Processing (ICCP)*, Sep. 2014, pp. 165–170. DOI: 10.1109/ICCP.2014.6936969.

[25] S. Song and J. Xiao, "Deep sliding shapes for amodal 3d object detection in rgb-d images," in *2016 IEEE Conference on Computer Vision and Pattern Recognition (CVPR)*, Jun. 2016, pp. 808–816. DOI: 10.1109/CVPR.2016.94.

[26] F. Alqahtani, J. Banks, V. Chandran, and J. Zhang, "3d face tracking using stereo cameras: A review," *IEEE Access*, vol. 8, pp. 94 373–94 393, 2020, ISSN: 2169-3536. DOI: 10.1109/ACCESS.2020.2994283.

[27] W. Ben Soltana, D. Huang, M. Ardabilian, L. Chen, and C. Ben-Amar, "Comparison of 2D/3D Features and Their Adaptive Score Level Fusion for 3D Face Recognition," in *3D Data Processing, Visualization and Transmission (3DPVT)*, Paris, France, May 2010, pp. 1–8. [Online]. Available: https://hal.archives-ouvertes.fr/hal-01381522.

[28] S. Gargoum and K. El-Basyouny, "Automated extraction of road features using lidar data: A review of lidar applications in transportation," in *2017 4th International Conference on Transportation Information and Safety (ICTIS)*, Aug. 2017, pp. 563–574. DOI: 10.1109/ICTIS.2017.8047822.

[29] T. B. Coenen and A. Golroo, "A review on automated pavement distress detection methods," *Cogent Engineering*, vol. 4, no. 1, D. L. Presti, Ed., p. 1 374 822, 2017. DOI: 10.1080/23311916.2017.1374822. eprint: https://www.tandfonline.com/doi/pdf/10.1080/23311916.2017.1374822. [Online]. Available: https://www.tandfonline.com/doi/abs/10.1080/23311916.2017.1374822.

[30] A. Bar Hillel, R. Lerner, D. Levi, and G. Raz, "Recent progress in road and lane detection: A survey," *Machine Vision and Applications*, vol. 25, no. 3, pp. 727–745, 2014, ISSN: 1432-1769. [Online]. Available: https://doi.org/10.1007/s00138-011-0404-2.

[31] M. Antunes, J. P. Barreto, C. Premebida, and U. Nunes, "Can stereo vision replace a laser rangefinder?" In *2012 IEEE/RSJ International Conference on Intelligent Robots and Systems*, Oct. 2012, pp. 5183–5190. DOI: 10.1109/IROS.2012.6385844.

[32] J. Han, D. Kim, M. Lee, and M. Sunwoo, "Enhanced road boundary and obstacle detection using a downward-looking lidar sensor," *IEEE Transactions on Vehicular Technology*, vol. 61, no. 3, pp. 971–985, Mar. 2012, ISSN: 1939-9359. DOI: 10.1109/TVT.2012.2182785.

[33] S. Lakshmanan and D. Grimmer, "A deformable template approach to detecting straight edges in radar images," *IEEE Transactions on Pattern Analysis and Machine Intelligence*, vol. 18, no. 4, pp. 438–443, Apr. 1996, ISSN: 1939-3539. DOI: 10.1109/34.491625.

[34] T. Li, Z. Liu, L. Ran, R. Xie, and X. Mu, "Comparative study on targets detection in high-resolution sar images," in *2016 CIE International Conference on Radar (RADAR)*, Oct. 2016, pp. 1–5. DOI: 10.1109/RADAR.2016.8059478.

[35] W. S. Wijesoma, K. R. S. Kodagoda, and A. P. Balasuriya, "Road-boundary detection and tracking using ladar sensing," *IEEE Transactions on Robotics and Automation*, vol. 20, no. 3, pp. 456–464, Jun. 2004, ISSN: 2374-958X. DOI: 10.1109/TRA.2004.825269.

[36] M. E. Warren, "Automotive lidar technology," in *2019 Symposium on VLSI Circuits*, Jun. 2019, pp. C254–C255. DOI: 10.23919/VLSIC.2019.8777993.

[37] M. Montemerlo, S. Thrun, H. Dahlkamp, D. Stavens, and S. Strohband, "Winning the darpa grand challenge with an ai robot," in *Proceedings of the 21st National Conference on Artificial Intelligence - Volume 1*, ser. AAAI'06, Boston, Massachusetts: AAAI Press, 2006, 982–987, ISBN: 9781577352815.

[38] M. A. Markom, A. H. Adom, E. S. M. M. Tan, S. A. A. Shukor, N. A. Rahim, and A. Y. M. Shakaff, "A mapping mobile robot using rp lidar scanner," in *2015 IEEE International Symposium on Robotics and Intelligent Sensors (IRIS)*, Oct. 2015, pp. 87–92. DOI: 10.1109/IRIS.2015.7451592.

[39] A. Hervieu and B. Soheilian, "Semi-automatic road/pavement modeling using mobile laser scanning," *ISPRS Annals of Photogrammetry, Remote Sensing and Spatial Information Sciences*, vol. II-3/W3, pp. 31–36, Oct. 2013.

[40] J. Armesto, J. Roca-Pardiñas, H. Lorenzo, and P. Arias, "Modelling masonry arches shape using terrestrial laser scanning data and non-parametric methods," *Engineering Structures*, vol. 32, no. 2, pp. 607 –615, 2010, ISSN: 0141-0296. DOI: https://doi.org/10.1016/j.engstruct.2009.11.007. [Online]. Available: http://www.sciencedirect.com/science/article/pii/S0141029609003526.

[41] N. Skowronski, K. Clark, R. Nelson, J. Hom, and M. Patterson, "Remotely sensed measurements of forest structure and fuel loads in the pinelands of new jersey," *Remote Sensing of Environment*, vol. 108, no. 2, pp. 123 –129, 2007, The Application of Remote Sensing to Fire Research in the Eastern United States, ISSN: 0034-4257. DOI: https://doi.org/10.1016/j.rse.2006.09.032. [Online]. Available: http://www.sciencedirect.com/science/article/pii/S0034425706004548.

[42] A. Johnson, S. Roumeliotis, and L. Matthies, “The jet propulsion laboratory autonomous helicopter testbed: A platform for planetary exploration technology research and development,” *J. Field Robotics*, vol. 23, pp. 245–267, Mar. 2006.

[43] J. Levinson and S. Thrun, “Robust vehicle localization in urban environments using probabilistic maps,” in *2010 IEEE International Conference on Robotics and Automation*, May 2010, pp. 4372–4378. DOI: `10.1109/ROBOT.2010.5509700`.

[44] S. Lacroix, A. Mallet, D. Bonnafous, *et al.*, “Autonomous rover navigation on unknown terrains functions and integration,” in *Experimental Robotics VII*, D. Rus and S. Singh, Eds., Berlin, Heidelberg: Springer Berlin Heidelberg, 2001, pp. 501–510, ISBN: 978-3-540-45118-1.

[45] Y. Ye, L. Fu, and B. Li, “Object detection and tracking using multilayer laser for autonomous urban driving,” in *2016 IEEE 19th International Conference on Intelligent Transportation Systems (ITSC)*, Nov. 2016, pp. 259–264. DOI: `10.1109/ITSC.2016.7795564`.

[46] Q. Li, L. Zhang, Q. Mao, *et al.*, “Motion field estimation for a dynamic scene using a 3d lidar,” *Sensors*, vol. 14, no. 9, pp. 16 672–16 691, 2014, ISSN: 1424-8220. DOI: `10.3390/s140916672`. [Online]. Available: `https://www.mdpi.com/1424-8220/14/9/16672`.

[47] B. Douillard, A. Brooks, and F. Ramos, “A 3d laser and vision based classifier,” in *2009 International Conference on Intelligent Sensors, Sensor Networks and Information Processing (ISSNIP)*, Dec. 2009, pp. 295–300. DOI: `10.1109/ISSNIP.2009.5416828`.

[48] M. Cho, “A study on the obstacle recognition for autonomous driving rc car using lidar and thermal infrared camera,” in *2019 Eleventh International Conference on Ubiquitous and Future Networks (ICUFN)*, Jul. 2019, pp. 544–546. DOI: `10.1109/ICUFN.2019.8806152`.

[49] T. Nagashima, T. Nagasaki, and H. Matsubara, “Object recognition method commonly usable for lidars with different vertical resolution,” in *2018 IEEE 7th Global Conference on Consumer Electronics (GCCE)*, Oct. 2018, pp. 751–753. DOI: `10.1109/GCCE.2018.8574830`.

[50] D. Steinhauser, O. Ruepp, and D. Burschka, “Motion segmentation and scene classification from 3d lidar data,” in *2008 IEEE Intelligent Vehicles Symposium*, Jun. 2008, pp. 398–403. DOI: `10.1109/IVS.2008.4621281`.

[51] A. Segal, D. Hähnel, and S. Thrun, “Generalized-icp,” *Proc. of Robotics: Science and Systems*, Jan. 2009. DOI: `10.15607/RSS.2009.V.021`.

[52] D. M. Cole and P. M. Newman, “Using laser range data for 3d slam in outdoor environments,” in *Proceedings 2006 IEEE International Conference on Robotics and Automation, 2006. ICRA 2006.*, May 2006, pp. 1556–1563. DOI: `10.1109/ROBOT.2006.1641929`.

[53] K. Lenac, A. Kitanov, R. Cupec, and I. Petrovic, “Fast planar surface 3d slam using lidar,” *Robotics and Autonomous Systems*, vol. 92, pp. 197–220, Jun. 2017.

[54] W. Lin, J. Hu, H. Xu, C. Ye, X. Ye, and Z. Li, “Graph-based slam in indoor environment using corner feature from laser sensor,” in *2017*

32nd Youth Academic Annual Conference of Chinese Association of Automation (YAC), May 2017, pp. 1211–1216. DOI: `10.1109/YAC.2017.7967597`.

[55] X. Liang, H. Chen, Y. Li, and Y. Liu, "Visual laser-slam in large-scale indoor environments," in *2016 IEEE International Conference on Robotics and Biomimetics (ROBIO)*, Dec. 2016, pp. 19–24. DOI: `10.1109/ROBIO.2016.7866271`.

[56] T. Zhang, X. Zhang, L. Wang, *et al.*, "Asipp remotely operated vehicle design (rov) and feasibility study," *IOP Conference Series: Earth and Environmental Science*, vol. 69, p. 012 133, Jun. 2017.

[57] S. Chi, Z. Xie, and W. Chen, "A laser line auto-scanning system for underwater 3d reconstruction," *Sensors*, vol. 16, no. 9, 2016, ISSN: 1424-8220. DOI: `10.3390/s16091534`. [Online]. Available: `https://www.mdpi.com/1424-8220/16/9/1534`.

[58] C. Wen, S. Pan, C. Wang, and J. Li, "An indoor backpack system for 2-d and 3-d mapping of building interiors," *IEEE Geoscience and Remote Sensing Letters*, vol. 13, no. 7, pp. 992–996, Jul. 2016, ISSN: 1558-0571. DOI: `10.1109/LGRS.2016.2558486`.

[59] S. Yang and Y. Fan, "3d building scene reconstruction based on 3d lidar point cloud," in *2017 IEEE International Conference on Consumer Electronics - Taiwan (ICCE-TW)*, Jun. 2017, pp. 127–128. DOI: `10.1109/ICCE-China.2017.7991028`.

[60] J. Qi, J. P. Gastellu-Etchegorry, and T. Yin, "Reconstruction of 3d forest mock-ups from airborne lidar data for multispectral image simulation using dart model," in *IGARSS 2018 - 2018 IEEE International Geoscience and Remote Sensing Symposium*, Jul. 2018, pp. 3975–3978. DOI: `10.1109/IGARSS.2018.8517627`.

[61] D. Borrmann, J. Elseberg, K. Lingemann, A. Nüchter, and J. Hertzberg, "Globally consistent 3d mapping with scan matching," *Robotics and Autonomous Systems*, vol. 56, no. 2, pp. 130–142, 2008, ISSN: 0921-8890. [Online]. Available: `http://www.sciencedirect.com/science/article/pii/S0921889007000863`.

[62] P. Newman, G. Sibley, M. Smith, *et al.*, "Navigating, recognizing and describing urban spaces with vision and lasers," *International Journal of Robotic Research - IJRR*, vol. 28, pp. 1406–1433, Oct. 2009.

[63] D. Droeschel, M. Schwarz, and S. Behnke, "Continuous mapping and localization for autonomous navigation in rough terrain using a 3d laser scanner," *Robotics and Autonomous Systems*, vol. 88, pp. 104 –115, 2017, ISSN: 0921-8890. DOI: `https://doi.org/10.1016/j.robot.2016.10.017`. [Online]. Available: `http://www.sciencedirect.com/science/article/pii/S0921889015303110`.

[64] O. Real-Moreno, J. C. Rodriguez-Quiñonez, O. Sergiyenko, *et al.*, "Accuracy improvement in 3d laser scanner based on dynamic triangulation for autonomous navigation system," in *2017 IEEE 26th International Symposium on Industrial Electronics (ISIE)*, Jun. 2017, pp. 1602–1608. DOI: `10.1109/ISIE.2017.8001486`.

[65] W. E. Clifton, B. Steele, G. Nelson, A. Truscott, M. Itzler, and M. Entwistle, "Medium altitude airborne Geiger-mode mapping LIDAR system," in *Laser Radar Technology and Applications XX; and Atmospheric Propagation XII*, M. D. Turner, G. W. Kamerman, L. M. W. Thomas, and E. J. Spillar, Eds., International Society for Optics and Photonics, vol. 9465, SPIE, 2015, pp. 39 –46. DOI: `10.1117/12.2193827`. [Online]. Available: `https://doi.org/10.1117/12.2193827`.

[66] R. Behringer, S. Sundareswaran, B. Gregory, *et al.*, "The darpa grand challenge - development of an autonomous vehicle," in *IEEE Intelligent Vehicles Symposium, 2004*, Jan. 2004, pp. 226–231. DOI: `10.1109/IVS.2004.1336386`.

[67] Y. Owechko, S. Medasani, and T. Korah, "Automatic recognition of diverse 3-d objects and analysis of large urban scenes using ground and aerial lidar sensors," in *CLEO/QELS: 2010 Laser Science to Photonic Applications*, May 2010, pp. 1–2. DOI: `10.1364/CLEO.2010.JThJ1`.

[68] S. Thrun, "Winning the darpa grand challenge," in *Machine Learning: ECML 2006*, J. Fürnkranz, T. Scheffer, and M. Spiliopoulou, Eds., Berlin, Heidelberg: Springer Berlin Heidelberg, 2006, pp. 4–4, ISBN: 978-3-540-46056-5.

[69] M. Buehler, K. Iagnemma, and S. Singh, "Special issue on the 2007 darpa urban challenge, part ii," *Journal of Field Robotics*, vol. 25, pp. 567–568, Sep. 2008. DOI: `10.1002/rob.20259`.

[70] M. Montemerlo, J. Becker, S. Bhat, *et al.*, "Junior: The stanford entry in the urban challenge," in *The DARPA Urban Challenge: Autonomous Vehicles in City Traffic*, M. Buehler, K. Iagnemma, and S. Singh, Eds. Berlin, Heidelberg: Springer Berlin Heidelberg, 2009, pp. 91–123, ISBN: 978-3-642-03991-1. DOI: `10.1007/978-3-642-03991-1_3`. [Online]. Available: `https://doi.org/10.1007/978-3-642-03991-1_3`.

[71] F. Garcia, F. Alonso, J. E. Naranjo, *et al.*, "Analysis of lidar sensors for new adas applications. usability in moving obstacles detection.," Jan. 2009.

[72] R. Changalvala and H. Malik, "Lidar data integrity verification for autonomous vehicle using 3d data hiding," in *2019 IEEE Symposium Series on Computational Intelligence (SSCI)*, Dec. 2019, pp. 1219–1225. DOI: `10.1109/SSCI44817.2019.9002737`.

[73] T. Ogawa, H. Sakai, Y. Suzuki, K. Takagi, and K. Morikawa, "Pedestrian detection and tracking using in-vehicle lidar for automotive application," in *2011 IEEE Intelligent Vehicles Symposium (IV)*, Jun. 2011, pp. 734–739. DOI: `10.1109/IVS.2011.5940555`.

[74] F. Garcia, A. de la Escalera, and J. M. Armingol, "Enhanced obstacle detection based on data fusion for adas applications," in *16th International IEEE Conference on Intelligent Transportation Systems (ITSC 2013)*, Oct. 2013, pp. 1370–1375. DOI: `10.1109/ITSC.2013.6728422`.

[75] G. Petrie and C. Toth, "Introduction to laser ranging, profiling, and scanning," in Nov. 2008, pp. 1–28, ISBN: 978-1-4200-5142-1. DOI: `10.1201/9781420051438.ch1`.

[76] B. Jutzi and H. Gross, "Normalization of lidar intensity data based on range and surface incidence angle," *ISPRS Ann. Photogramm. Remote Sens. Spat. Inf. Sci.*, vol. 38, Jan. 2009.

[77] S. Kaasalainen, A. Jaakkola, M. Kaasalainen, A. Krooks, and A. Kukko, "Analysis of incidence angle and distance effects on terrestrial laser scanner intensity: Search for correction methods," *Remote Sensing*, vol. 3, no. 10, pp. 2207–2221, 2011, ISSN: 2072-4292. DOI: `10.3390/rs3102207`. [Online]. Available: `https://www.mdpi.com/2072-4292/3/10/2207`.

[78] P. Besesty, "Télémètre à laser puce," Techniques de l'ingénieur, Tech. Rep., Mar. 1999. [Online]. Available: `https://studylibfr.com/doc/2096490/principe-t%C3%A9l%C3%A9m%C3%A8tre-laser-211.2-ko`.

[79] J. C. Fernandez Diaz, W. E. Carter, R. L. Shrestha, and C. L. Glennie, "Lidar remote sensing," in *Handbook of Satellite Applications*, J. N. Pelton, S. Madry, and S. Camacho-Lara, Eds. New York, NY: Springer New York, 2016, pp. 1–52. DOI: `10.1007/978-1-4614-6423-5_44-3`. [Online]. Available: `https://doi.org/10.1007/978-1-4614-6423-5_44-3`.

[80] N. Muhammad and S. Lacroix, "Calibration of a rotating multi-beam lidar," in *2010 IEEE/RSJ International Conference on Intelligent Robots and Systems*, Oct. 2010, pp. 5648–5653. DOI: `10.1109/IROS.2010.5651382`.

[81] C. Glennie and D. D. Lichti, "Static calibration and analysis of the velodyne hdl-64e s2 for high accuracy mobile scanning," *Remote Sensing*, vol. 2, no. 6, pp. 1610–1624, 2010, ISSN: 2072-4292. DOI: `10.3390/rs2061610`. [Online]. Available: `https://www.mdpi.com/2072-4292/2/6/1610`.

[82] C. Glennie, A. Kusari, and A. Facchin, "Calibration and stability analysis of the vlp-16 laser scanner," *ISPRS - International Archives of the Photogrammetry, Remote Sensing and Spatial Information Sciences*, vol. XL-3/W4, pp. 55–60, Mar. 2016. DOI: `10.5194/isprsarchives-XL-3-W4-55-2016`.

[83] Y. Zeng, H. Yu, H. Dai, *et al.*, "An improved calibration method for a rotating 2d lidar system," *Sensors*, vol. 18, no. 2, 2018, ISSN: 1424-8220. DOI: `10.3390/s18020497`. [Online]. Available: `https://www.mdpi.com/1424-8220/18/2/497`.

[84] L. Kurnianggoro, H. V. Dung, and K.-H. Jo, "Calibration of a 2d laser scanner system and rotating platform using a point-plane constraint," *Computer Science and Information Systems*, vol. 12, pp. 307–322, Jan. 2015. DOI: `10.2298/CSIS141020093K`.

[85] G. Atanacio-Jiménez, J. González-Barbosa, J. Hurtado-Ramos, *et al.*, "Lidar velodyne hdl-64e calibration using pattern planes," American English, *International Journal of Advanced Robotic Systems*, pp. 70–82, Nov. 2011, ISSN: 1729-8806.

[86] J. Levinson and S. Thrun, "Unsupervised calibration for multi-beam lasers," in *Experimental Robotics*, Springer, 2014, pp. 179–193.

[87] O. Yalcin, A. Sayar, O. Arar, S. Akpinar, and S. Kosunalp, "Approaches of road boundary and obstacle detection using lidar," *IFAC Proceedings Volumes*, vol. 46, no. 25, pp. 211 –215, 2013, 1st IFAC Workshop on Advances in Control and Automation Theory for Transportation Applications, ISSN: 1474-6670. DOI: https://doi.org/10.3182/20130916-2-TR-4042.00025. [Online]. Available: http://www.sciencedirect.com/science/article/pii/S1474667015352356.

[88] Y. Kang, C. Roh, S. Suh, and B. Song, "A lidar-based decision-making method for road boundary detection using multiple kalman filters," *IEEE Transactions on Industrial Electronics*, vol. 59, no. 11, pp. 4360–4368, Nov. 2012, ISSN: 1557-9948. DOI: 10.1109/TIE.2012.2185013.

[89] R. Fernandes, C. Premebida, P. Peixoto, D. Wolf, and U. Nunes, "Road detection using high resolution lidar," in *IEEE Vehicle Power and Propulsion Conference (VPPC)*, Oct. 2014, pp. 1–6. DOI: 10.1109/VPPC.2014.7007125.

[90] R. Polikar, "Pattern recognition," in *Wiley Encyclopedia of Biomedical Engineering*. American Cancer Society, 2006, ISBN: 9780471740360. DOI: 10.1002/9780471740360.ebs0904. eprint: https://onlinelibrary.wiley.com/doi/pdf/10.1002/9780471740360.ebs0904. [Online]. Available: https://onlinelibrary.wiley.com/doi/abs/10.1002/9780471740360.ebs0904.

[91] W. Zhang, "Lidar-based road and road-edge detection," in *2010 IEEE Intelligent Vehicles Symposium*, Jun. 2010, pp. 845–848. DOI: 10.1109/IVS.2010.5548134.

[92] V. Nguyen, A. Martinelli, N. Tomatis, and R. Siegwart, "A comparison of line extraction algorithms using 2d laser rangefinder for indoor mobile robotics," in *2005 IEEE/RSJ International Conference on Intelligent Robots and Systems*, Aug. 2005, pp. 1929–1934. DOI: 10.1109/IROS.2005.1545234.

[93] T. Pavlidis and S. L. Horowitz, "Segmentation of plane curves," *IEEE Transactions on Computers*, vol. C-23, no. 8, pp. 860–870, Aug. 1974, ISSN: 1557-9956. DOI: 10.1109/T-C.1974.224041.

[94] K. O. Arras and R. Y. Siegwart, "Feature extraction and scene interpretation for map-based navigation and map building," in *Mobile Robots XII*, D. W. Gage, Ed., International Society for Optics and Photonics, vol. 3210, SPIE, Jan. 1998, pp. 42 –53. DOI: 10.1117/12.299565. [Online]. Available: https://doi.org/10.1117/12.299565.

[95] A. Siadat, A. Kaske, S. Klausmann, M. Dufaut, and R. Husson, "An optimized segmentation method for a 2d laser-scanner applied to mobile robot navigation," *IFAC Proceedings Volumes*, vol. 30, no. 7, pp. 149–154, 1997, ISSN: 1474-6670. DOI: 10.1016/S1474-6670(17)43255-1. [Online]. Available: http://www.sciencedirect.com/science/article/pii/S1474667017432551.

[96] M. A. Fischler and R. C. Bolles, "Random sample consensus: A paradigm for model fitting with applications to image analysis and automated cartography," *Commun. ACM*, vol. 24, no. 6, 381–395, Jan. 1981, ISSN:

0001-0782. DOI: 10.1145/358669.358692. [Online]. Available: https://doi.org/10.1145/358669.358692.

[97] D. Forsyth and J. Ponce, *Computer Vision: A Modern Approach. (Second edition)*. Prentice Hall, Nov. 2011, p. 792. [Online]. Available: https://hal.inria.fr/hal-01063327.

[98] S. T. Pfister, S. I. Roumeliotis, and J. W. Burdick, "Weighted line fitting algorithms for mobile robot map building and efficient data representation," in *2003 IEEE International Conference on Robotics and Automation (Cat. No.03CH37422)*, vol. 1, Sep. 2003, 1304–1311 vol.1. DOI: 10.1109/ROBOT.2003.1241772.

[99] J. C. Noyer, R. Lherbier, and B. Fortin, "Automatic feature extraction in laser rangefinder data using geometric invariance," in *2010 Conference Record of the Forty Fourth Asilomar Conference on Signals, Systems and Computers*, Nov. 2010, pp. 199–203. DOI: 10.1109/ACSSC.2010.5757498.

[100] B. Fortin, R. Lherbier, and J. Noyer, "Feature extraction in scanning laser range data using invariant parameters: Application to vehicle detection," *IEEE Transactions on Vehicular Technology*, vol. 61, no. 9, pp. 3838–3850, Nov. 2012, ISSN: 1939-9359. DOI: 10.1109/TVT.2012.2211630.

[101] K. O. Arras, "An introduction to error propagation: Derivation, meaning and examples of equation cy= fx cx fxt," en, ser. EPFL-ASL-TR-98-01 R3, Published online by ETH Zurich., Lausanne: École Polytechnique Fédérale de Lausanne, 1998. DOI: 10.3929/ethz-a-010113668. [Online]. Available: http://hdl.handle.net/20.500.11850/82620.

[102] B. Fortin, R. Lherbier, and J. Noyer, "A model-based joint detection and tracking approach for multi-vehicle tracking with lidar sensor," *IEEE Transactions on Intelligent Transportation Systems*, vol. 16, no. 4, pp. 1883–1895, Aug. 2015, ISSN: 1558-0016. DOI: 10.1109/TITS.2015.2391131.

[103] J. Laurent and J.-F. Hébert, "High performance 3d sensors for the characterization of road surface defects.," in *IAPR Workshop on Machine Vision Applications*. Jan. 2002, pp. 388–391.

[104] J Laurent, D Lefebvre, and E Samson, "Development of a new 3d transverse laser profiling system for the automatic measurement of road cracks," in *Symposium on Pavement Surface Characteristics, 6th, 2008, Portoroz, Slovenia*, Jan. 2008.

[105] J. Laurent, J. F. Hébert, D. Lefebvre, and Y. Savard, "Using 3d laser profiling sensors for the automated measurement of road surface conditions," in *7th RILEM International Conference on Cracking in Pavements*, A. Scarpas, N. Kringos, I. Al-Qadi, and A. Loizos, Eds., Dordrecht: Springer Netherlands, 2012, pp. 157–167.

[106] H. Bian, L. Bai, S.-E. Chen, and S.-G. Wang, "Lidar based edge-detection for bridge defect identification," in *Nondestructive Characterization for Composite Materials, Aerospace Engineering, Civil Infrastructure, and Homeland Security 2012*, A. L. Gyekenyesi, Ed., International Society for Optics and Photonics, vol. 8347, SPIE, Mar. 2012, pp. 214 –223. DOI:

10.1117/12.915264. [Online]. Available: https://doi.org/10.1117/12.915264.

[107] L. Chen, J. Yang, and H. Kong, "Lidar-histogram for fast road and obstacle detection," in *2017 IEEE International Conference on Robotics and Automation (ICRA)*, May 2017, pp. 1343–1348. DOI: 10.1109/ICRA.2017.7989159.

[108] J. Fritsch, T. Kühnl, and A. Geiger, "A new performance measure and evaluation benchmark for road detection algorithms," in *16th International IEEE Conference on Intelligent Transportation Systems (ITSC 2013)*, Oct. 2013, pp. 1693–1700. DOI: 10.1109/ITSC.2013.6728473.

[109] P. Y. Shinzato, D. F. Wolf, and C. Stiller, "Road terrain detection: Avoiding common obstacle detection assumptions using sensor fusion," in *2014 IEEE Intelligent Vehicles Symposium Proceedings*, Jun. 2014, pp. 687–692. DOI: 10.1109/IVS.2014.6856454.

[110] L. Xiao, B. Dai, D. Liu, T. Hu, and T. Wu, "Crf based road detection with multi-sensor fusion," in *2015 IEEE Intelligent Vehicles Symposium (IV)*, Jun. 2015, pp. 192–198. DOI: 10.1109/IVS.2015.7225685.

[111] N. J. Sucgang, M. Ramos Jr, and N. A. Arriola, "Road surface obstacle detection using vision and lidar for autonomous vehicle," in *Proceedings of the international multiconference of engineers computer scientists (IMECS), Hongkong, China*, 2017.

[112] J. Lin and Y. Liu, "Potholes detection based on svm in the pavement distress image," in *2010 Ninth International Symposium on Distributed Computing and Applications to Business, Engineering and Science*, Aug. 2010, pp. 544–547. DOI: 10.1109/DCABES.2010.115.

[113] E. Salari and X. Yu, "Pavement distress detection and classification using a genetic algorithm," in *2011 IEEE Applied Imagery Pattern Recognition Workshop (AIPR)*, Oct. 2011, pp. 1–5. DOI: 10.1109/AIPR.2011.6176378.

[114] J. H. Holland, "Genetic algorithms and the optimal allocation of trials," *SIAM Journal on Computing*, vol. 2, no. 2, pp. 88–105, 1973. DOI: 10.1137/0202009. eprint: https://doi.org/10.1137/0202009. [Online]. Available: https://doi.org/10.1137/0202009.

[115] N. Otsu, "A threshold selection method from gray-level histograms," *IEEE Transactions on Systems, Man, and Cybernetics*, vol. 9, no. 1, pp. 62–66, Jan. 1979, ISSN: 2168-2909. DOI: 10.1109/TSMC.1979.4310076.

[116] C. Koch and I. Brilakis, "Pothole detection in asphalt pavement images," *Advanced Engineering Informatics*, vol. 25, pp. 507–515, Aug. 2011. DOI: 10.1016/j.aei.2011.01.002.

[117] R. C. Gonzalez, R. E. Woods, and S. L. Eddins, *Digital Image Processing Using MATLAB*. Gatesmark Publishing, 2009.

[118] A. Fitzgibbon, M. Pilu, and R. B. Fisher, "Direct least square fitting of ellipses," *IEEE Transactions on Pattern Analysis and Machine Intelligence*, vol. 21, no. 5, pp. 476–480, May 1999, ISSN: 1939-3539. DOI: 10.1109/34.765658.

[119] C. Koch and I. Brilakis, "Improving pothole recognition through vision tracking for automated pavement assessment," *EG-ICE 2011, European Group for Intelligent Computing in Engineering*, Jan. 2011.

[120] A. Yilmaz, O. Javed, and M. Shah, "Object tracking: A survey. acm comput surv," *ACM Comput. Surv.*, vol. 38, Dec. 2006. DOI: 10.1145/1177352.1177355.

[121] A. Makhmalbaf, M.-W. Park, J. Yang, I. Brilakis, and P. A. Vela, "2d vision tracking methods' performance comparison for 3d tracking of construction resources," in *Construction Research Congress 2010*. May 2010, pp. 459–469. DOI: 10.1061/41109(373)46. eprint: https://ascelibrary.org/doi/pdf/10.1061/41109%28373%2946. [Online]. Available: https://ascelibrary.org/doi/abs/10.1061/41109%28373%2946.

[122] S. Venkatesh, E. Abhiram, S. Rajarajeswari, K. M. Sunil Kumar, S. Balakuntala, and N. Jagadish, "An intelligent system to detect, avoid and maintain potholes: A graph theoretic approach," in *2014 Seventh International Conference on Mobile Computing and Ubiquitous Networking (ICMU)*, Jan. 2014, pp. 80–80. DOI: 10.1109/ICMU.2014.6799066.

[123] C. Mertz, "Continuous road damage detection using regular service vehicles," in *Proceedings of the ITS World Congress*, Oct. 2011.

[124] Q. Xu, T. Mak, J. Ko, and R. Sengupta, "Vehicle-to-vehicle safety messaging in dsrc," in *Proceedings of the 1st ACM International Workshop on Vehicular Ad Hoc Networks*, ser. VANET '04, New York, NY, USA: Association for Computing Machinery, 2004, 19–28, ISBN: 1581139225. DOI: 10.1145/1023875.1023879. [Online]. Available: https://doi.org/10.1145/1023875.1023879.

[125] A. Danti, J. Kulkarni, and P. Hiremath, "An image processing approach to detect lanes, pot holes and recognize road signs in indian roads," *International Journal of Modeling and Optimization*, vol. 2, pp. 658–662, Jan. 2012. DOI: 10.7763/IJMO.2012.V2.204.

[126] R. O. Duda and P. E. Hart, "Use of the hough transformation to detect lines and curves in pictures," *Commun. ACM*, vol. 15, no. 1, 11–15, Jan. 1972, ISSN: 0001-0782. DOI: 10.1145/361237.361242. [Online]. Available: https://doi.org/10.1145/361237.361242.

[127] L. Huidrom, L. K. Das, and S. K. Sud, "Method for automated assessment of potholes, cracks and patches from road surface video clips," *Procedia - Social and Behavioral Sciences*, vol. 104, pp. 312–321, 2013, ISSN: 1877-0428. DOI: 10.1016/j.sbspro.2013.11.124. [Online]. Available: http://www.sciencedirect.com/science/article/pii/S1877042813045151.

[128] L. Huidrom, L. Das, and S. Goel, "Robust method for automated segmentation of frames with/without distress from road surface video clips," *Journal of Transportation Engineering*, vol. 140, pp. 31–41, Jan. 2014. DOI: 10.1061/(ASCE)TE.1943-5436.0000564.

[129] R. C. Gonzalez and R. E. Woods, *Digital Image Processing (3rd Edition)*. USA: Prentice-Hall, Inc., 2006, ISBN: 013168728X.

[130] D. G. R. Bradski and A. Kaehler, *Learning Opencv, 1st Edition*, First. O'Reilly Media, Inc., 2008, ISBN: 9780596516130.

[131] F. Chang, C.-J. Chen, and C.-J. Lu, "A linear-time component-labeling algorithm using contour tracing technique," *Computer Vision and Image Understanding*, vol. 93, no. 2, pp. 206–220, 2004, ISSN: 1077-3142. DOI: `10.1016/j.cviu.2003.09.002`. [Online]. Available: `http://www.sciencedirect.com/science/article/pii/S1077314203001401`.

[132] L. Yang, F. Albregtsen, T. Lønnestad, and P. Grøttum, "Methods to estimate areas and perimeters of blob-like objects: A comparison.," *Proceedings of the IAPR workshop on machine vision applications*, pp. 272–276, Jan. 1994.

[133] X. Yu and E. Salari, "Pavement pothole detection and severity measurement using laser imaging," in *2011 IEEE INTERNATIONAL CONFERENCE ON ELECTRO/INFORMATION TECHNOLOGY*, May 2011, pp. 1–5. DOI: `10.1109/EIT.2011.5978573`.

[134] B. J. Lee and H. D. Lee, "Position-invariant neural network for digital pavement crack analysis," *Computer-Aided Civil and Infrastructure Engineering*, vol. 19, no. 2, pp. 105–118, 2004. DOI: `https://doi.org/10.1111/j.1467-8667.2004.00341.x`. eprint: `https://onlinelibrary.wiley.com/doi/pdf/10.1111/j.1467-8667.2004.00341.x`. [Online]. Available: `https://onlinelibrary.wiley.com/doi/abs/10.1111/j.1467-8667.2004.00341.x`.

[135] B. X. Yu and X. Yu, "Vibration-based system for pavement condition evaluation," in *Applications of Advanced Technology in Transportation*. 2006, pp. 183–189. DOI: `10.1061/40799(213)31`. eprint: `https://ascelibrary.org/doi/pdf/10.1061/40799%28213%2931`. [Online]. Available: `https://ascelibrary.org/doi/abs/10.1061/40799%28213%2931`.

[136] K. De Zoysa, C. Keppitiyagama, G. P. Seneviratne, and W. W. A. T. Shihan, "A public transport system based sensor network for road surface condition monitoring," in *Proceedings of the 2007 Workshop on Networked Systems for Developing Regions*, ser. NSDR '07, New York, NY, USA: Association for Computing Machinery, 2007, ISBN: 9781595937872. DOI: `10.1145/1326571.1326585`. [Online]. Available: `https://doi.org/10.1145/1326571.1326585`.

[137] J. Eriksson, L. Girod, B. Hull, R. Newton, S. Madden, and H. Balakrishnan, "The pothole patrol: Using a mobile sensor network for road surface monitoring," in *Proceedings of the 6th International Conference on Mobile Systems, Applications, and Services*, ser. MobiSys '08, New York, NY, USA: Association for Computing Machinery, Jan. 2008, 29–39, ISBN: 9781605581392. DOI: `10.1145/1378600.1378605`. [Online]. Available: `https://doi.org/10.1145/1378600.1378605`.

[138] "User manual and programming guide vlp-16," *Velodyne LiDAR*, [Online]. Available: `https://velodynelidar.com/products/puck/#downloads`.

[139] "Veloview software," *Velodyne LiDAR*, [Online]. Available: `https://www.paraview.org/veloview/`.

[140] "Wireshark software," *WireShark*, [Online]. Available: https://www.wireshark.org/.

[141] "Matlab software," *MathWorks*, [Online]. Available: https://www.mathworks.com/products/matlab.html.

[142] R. M. Brannon, "Rotation: A review of useful theorems involving proper orthogonal matrices referenced to three-dimensional physical space," *Computational Physics and Mechanics*, 2002.

[143] S. Filin, "Recovery of systematic biases in laser altimetry data using natural surfaces," *Photogrammetric Engineering and Remote Sensing*, vol. 69, pp. 1235–1242, Nov. 2003. DOI: 10.14358/PERS.69.11.1235.

[144] M. Magnusson, "The three-dimensional normal-distributions transform an efficient representation for registration, surface analysis, and loop detection," Ph.D. dissertation, OREBRO UNIVERSITY, Dec. 2009.

[145] S. M. Kay, *Fundamentals of Statistical Signal Processing: Estimation theory* (Fundamentals of Statistical Signal Processing). USA: PTR Prentice-Hall, 1993, ISBN: 9780133457117. [Online]. Available: https://books.google.fr/books?id=aFwESQAACAAJ.

[146] G. Taubin, "3d rotations," *IEEE Computer Graphics and Applications*, vol. 31, no. 6, pp. 84–89, Nov. 2011, ISSN: 0272-1716. DOI: 10.1109/MCG.2011.92.

[147] L. Duc-Hung, P. Cong-Kha, N. T. T. Trang, and B. T. Tu, "Parameter extraction and optimization using levenberg-marquardt algorithm," in *Fourth International Conference on Communications and Electronics (ICCE)*, Aug. 2012, pp. 434–437. DOI: 10.1109/CCE.2012.6315945.

[148] B. Yang, L. Fang, Q. Li, and J. Li, "Automated extraction of road markings from mobile lidar point clouds," *Photogrammetric Engineering and Remote Sensing*, vol. 78, pp. 331–338, Apr. 2012. DOI: 10.14358/PERS.78.4.331.

[149] Y. Yu, J. Li, H. Guan, C. Wang, and J. Yu, "Automated detection of road manhole and sewer well covers from mobile lidar point clouds," *IEEE Geoscience and Remote Sensing Letters*, vol. 11, no. 9, pp. 1549–1553, Sep. 2014, ISSN: 1558-0571. DOI: 10.1109/LGRS.2014.2301195.

[150] R. M. Haralick and L. G. Shapiro, *Computer and Robot Vision*, 1st. USA: Addison-Wesley Longman Publishing Co., Inc., 1992, pp. 28–48, ISBN: 0201569434.

Résumé Étendu de la Thèse

1. Le Contexte

La connaissance de l'état du réseau routier dans un pays est un enjeu important pour pouvoir déployer une politique rationnelle d'entretien, de réhabilitation et d'amélioration du trafic routier. Comme nous le savons, certains accidents de la circulation sont le résultat de la présence de défauts ou de petits obstacles sur les routes. Cependant, les accidents de la route représentent un problème de santé mondial majeur pour la sécurité humaine. Comme fait clé, le rapport de l'Organisation mondiale de la santé (OMS) sur l'état mondial de la sécurité routière indique que le nombre total de décès sur les routes a plafonné à 1.15 million de personnes en 2000. Ensuite, il augmente de 0.1 millions pour atteindre 1.25 millions de morts sur les routes en 2015 [1], [2], et 1.35 millions de morts en 2018 [3]. En particulier dans les pays à faibles revenus tels que l'Afrique et l'Asie du Sud-Est, un record de 95% des décès dans le monde se produisent sur la route [4], et plus de la moitié des décès dus aux accidents de la route concernent des usagers de la route vulnérables : motocyclistes, cyclistes et piétons, où la plupart des décès et des incapacités concernent des personnes âgées de 5 à 29 ans [5]–[7]. De plus, l'estimation du coût des accidents de la route atteint 3% du produit national brut des économies mondiales, ce qui a un impact sérieux sur les économies nationales [3], [4]. Par conséquent, la collaboration des Nations Unies (ONU) sur la sécurité routière a élaboré un plan mondial qui propose un programme de développement durable à l'horizon 2030 pour fixer un objectif ambitieux de réduction de moitié du nombre mondial de décès et de blessures dus aux accidents de la route [8], [9].

Cette thèse de doctorat s'inscrit dans ce cadre puisqu'elle se propose de fournir un modèle géométrique et topologique de routes et d'en extraire des informations sémantiques. De plus, ces travaux portent sur la caractérisation du revêtement routier et la présence de zones potentiellement dangereuses, d'abord par un **calibrage des informations géométriques d'environnement**, suivi d'une **détection et localisation des défauts de la route**. Il est également important de visualiser et de localiser les informations géométriques de chaque défaut obtenu sur la route.

Ce travail s'inscrit dans le cadre général des systèmes de perception multi-capteurs, portant plus particulièrement sur les différentes caractéristiques ci-dessus, qui seront obtenues à partir d'une information télémétrique d'un télémètre multi-lasers (Light Detection and Ranging LiDAR, Laser Range Finder LRF) monté sur un véhicule comme illustré à la Figure 1.

(a) VLP-16 LiDAR monté sur un véhicule (b) LiDAR VLP-16 monté sur un support fixe

FIGURE 1: Système VLP-16

Dans les applications de transport, le développement des Systèmes Avancés d'Aide à la Conduite (ADAS) fait l'objet de nombreux travaux depuis une vingtaine d'années [10]. Dans le contexte des systèmes de transport, l'objectif est de surveiller l'environnement du véhicule afin d'informer le conducteur, à chaque instant, des situations potentiellement dangereuses. Des méthodes de détection multi-objets dans les données d'un télémètre laser à balayage embarqué à bord d'un véhicule en mouvement ont été proposées. Même si ces méthodes conservent certaines limitations inhérentes à la nature physique du signal de mesure, ce capteur laser présente de nombreux avantages pour l'ADAS : vision jour/nuit, forte précision, fréquence de mesure élevée, tirs laser directifs, large champ de perception. L'inconvénient majeur d'un télémètre laser monocouche est sa sensibilité aux mouvements de tangage, liée à sa directivité : les distances mesurées peuvent être perturbées et donner lieu à des mesures indésirables de la scène, désignées par le terme plus général de " fouillis ". Le développement des télémètres multicouches, c'est-à-dire travaillant sur plusieurs plans de mesure, a permis de minimiser ces perturbations inhérentes à la nature physique de la mesure. Bien qu'ayant la particularité de délivrer des informations précises de positionnement relatif contrairement aux capteurs de type caméra vidéo, les télémètres laser se distinguent par la relative pauvreté des informations reçues sur la scène (directement liée à la résolution angulaire du capteur).

Il est donc nécessaire de développer des solutions informant le conducteur sur les défauts de route. Par ailleurs, ces informations sont importantes pour obtenir des données statistiques sur les défauts de route afin de limiter les zones à risque et de construire une aide à la décision pour l'amélioration du réseau routier. Notre hypothèse fonctionne précisément sur une méthode de calibration extrinsèque pour le capteur LiDAR basée sur l'estimation du modèle de plan géométrique, qui sert les deux méthodes de détection de défauts de route proposées : celle basée sur les caractéristiques de la route et celle basée sur une approche par grille.

2. Buts et Objectifs de la Thèse

Dans les applications de transport, de nombreux articles utilisent le LiDAR pour détecter et suivre des objets d'intérêt (piétons, véhicules, etc...) à partir de mesures 3D. Le capteur LiDAR est également utilisé pour détecter la route, souvent en complément des capteurs de la caméra. Dans ces applications, l'idée est d'avoir une vue complète de l'environnement du conducteur sur l'horizon le plus large possible. Par conséquent, l'objectif de cette thèse repose sur un capteur LiDAR à faible angle d'inclinaison (capteur orienté horizontalement) pour étudier et analyser les défauts de la route : trous, bosses ou toutes couches externes homogènes, ce qui aura un impact sur le problème d'accidentologie causée par les zones dangereuses du réseau routier. Cette étude comprend plusieurs objectifs scientifiques : détection, visualisation et localisation des défauts de la route.

3. Points Clés de la Thèse

Les points clés du problème étudié dans cette thèse sont illustrés dans la figure 2 et sont répertoriés ci-dessous :

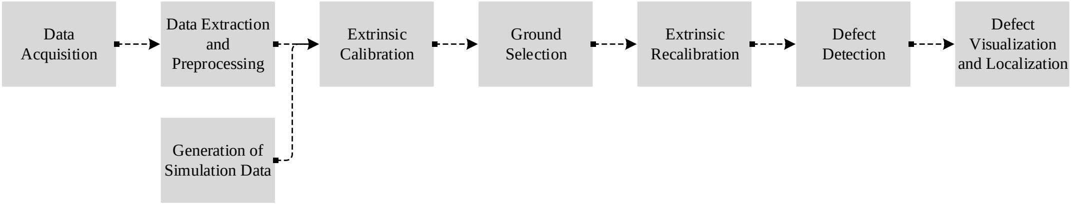

FIGURE 2: Schéma Fonctionnel de la Thèse

1. Génération de données de simulation sur des données de capteurs LiDAR pour différentes orientations et altitudes.
2. Optimisation de l'altitude et de l'orientation LiDAR à l'aide des données synthétiques, avant d'analyser la couverture des points de distribution LiDAR au sol, pour convenir à l'application pratique et assurer la possibilité de détection des défauts de la route.
3. Acquisition de données à l'aide d'un capteur LiDAR monté sur un véhicule en mouvement.
4. Extraction de données (portée, azimut, élévation, réflectivité et temps) à partir du fichier au format .pcap. Puis prétraitement des données et présentation du player PointCloud.
5. Méthode d'étalonnage LiDAR/Sol extrinsèque 3D utilisant une estimation basée sur le plan géométrique 3D.
6. Sélection au sol Méthode PointCloud utilisant un filtre gaussien différentiel, pour éliminer : les obstacles qui existent sur la route, et les objets qui entourent la route.
7. Re-calibrage extrinsèque pour le PointCloud routier pour améliorer le processus de calibrage.
8. Méthode basée sur les fonctionnalités de détection des défauts.
9. Visualisation et localisation des défauts à l'aide de la méthode basée sur la grille.

4. Contributions Proposées

Dans le cadre de cette étude (détection des défauts de la route), le capteur LiDAR est vers le sol afin d'augmenter la densité de points couvrant les défauts par le laser multi-élévation comme le montre la Figure 3. Cela entraîne une modification complexe de la scène 3D au sol perçue par le LiDAR. Par conséquent, un étalonnage extrinsèque a été adopté afin de transformer le référentiel du LiDAR en un référentiel global, transformation ainsi les points d'impact au sol en une scène exploitable.

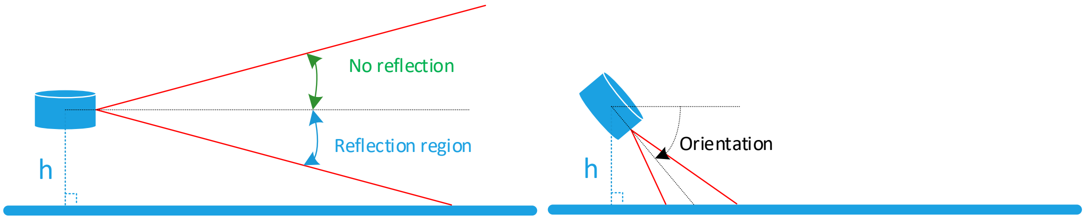

(a) Pas d'orientation (b) Orientation LiDAR

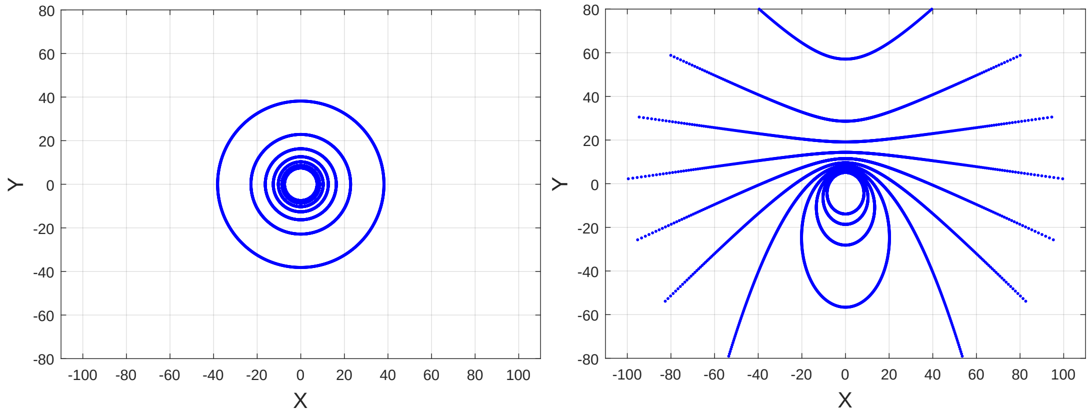

(c) Pas de rotation $\phi_x = 0^\circ$ (d) $\phi_x < \frac{1}{2}vFOV$

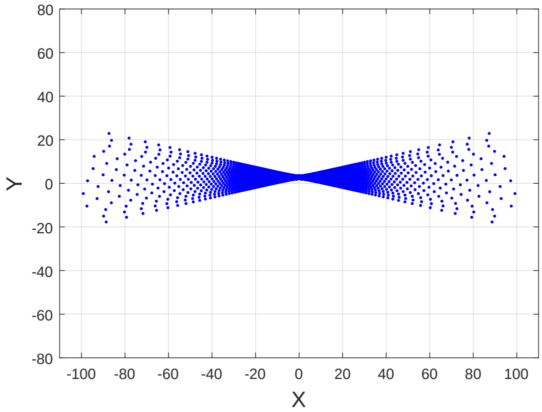

(e) $\phi_x > \frac{1}{2}vFOV$

FIGURE 3: Grande zone clairsemée par rapport aux points à haute densité

4.1. Nouvelle Méthode d'Etalonnage

Notre objectif est de proposer une méthode de calibration (et d'estimation du plan de route) qui fonctionne dans des conditions expérimentales difficiles (grand angle d'inclinaison). En effet, nous visons à développer une méthode de calibrage qui permette de déterminer précisément le plan de route dans un voisinage très proche du véhicule. L'idée à terme est de détecter les défauts de la route lors de la conduite sur le réseau routier. Bien que développée dans cet esprit (c'est-à-dire avec un haut degré de précision dans la détermination du plan de route), notre méthode est suffisamment générale pour être applicable dans tout contexte opérationnel plus large.

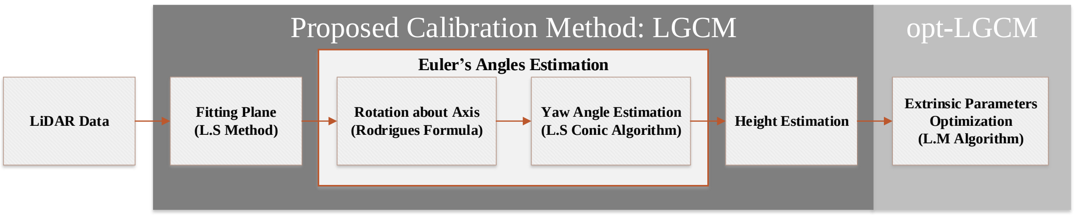

FIGURE 4: Le schéma fonctionnel de la méthode d'étalonnage extrinsèque proposée

Afin d'atteindre l'objectif clé ci-dessus, cette thèse aborde une nouvelle méthode de calibration extrinsèque flexible, publiée dans [11], [12]. La méthode d'étalonnage proposée peut être résumée par les deux contributions suivantes : (1) estimation du modèle de plan au sol et (2) estimation de la matrice de transformation de rotation de la référence mondiale au sol au cadre du capteur LiDAR, comme indiqué sur la figure 4. Les angles d'Euler 3D (orientation du capteur) et la hauteur (altitude du capteur au-dessus du sol) sont deux paramètres extrinsèques essentiels nécessaires pour calibrer les capteurs LiDAR 3D complets comme indiqué sur la figure 5, afin d'améliorer la capacité de défaut de la route détection comme cela sera expliqué dans la section 4.2.1. De plus, le problème est modélisé par une transformation 4-DOF (degré de liberté) : rotation 3-DOF et hauteur 1-DOF, au lieu d'une transformation 6-DOF : rotation 3-DOF et translation 3-DOF. Cet avantage de modélisation offre la simplicité dans le processus d'optimisation des paramètres extrinsèques.

Par rapport à une précédente méthode basée sur le plan [13], [14], l'approche développée peut être généralisée à tous les types de télémètres laser à balayage et présente une estimation optimisée de tous les paramètres de calibration extrinsèques (angles, hauteur). Cette méthode globale peut être mise

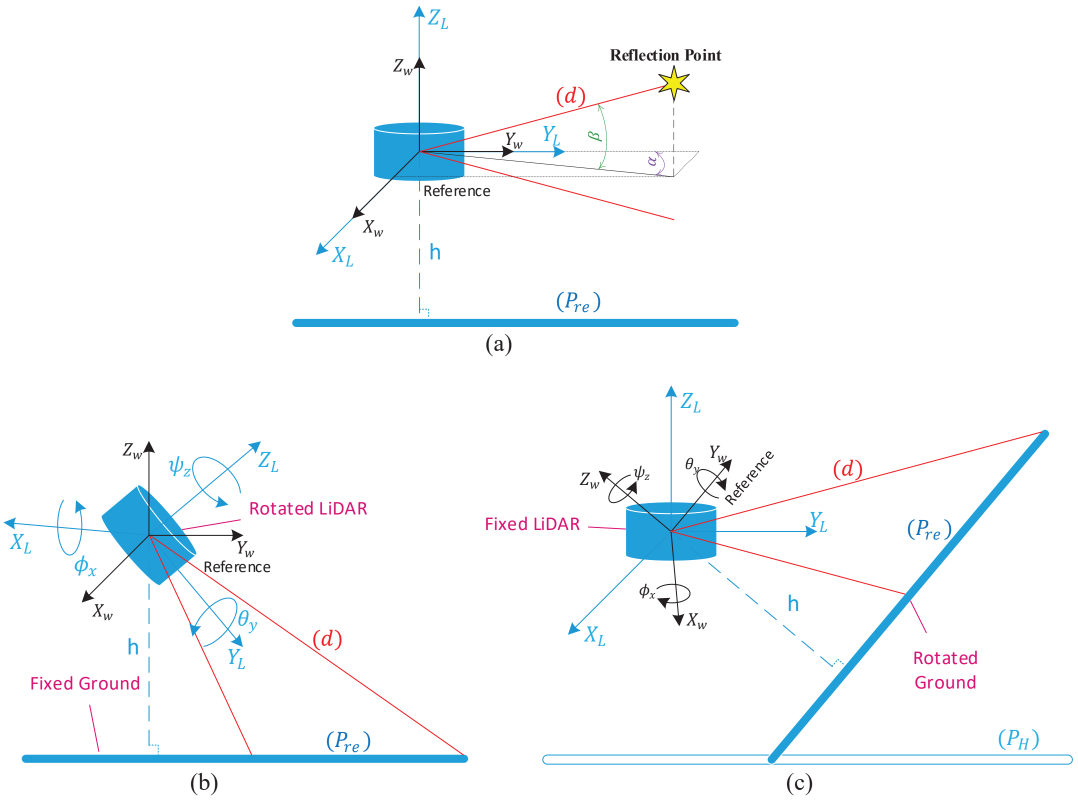

FIGURE 5: (a) Pas d'orientation, (b) Concept d'orientation pratique, (c) Concept d'orientation scientifique

en œuvre sur différents capteurs LiDAR cylindriques (3D low-cost et full 3D) avec différentes précisions de portée. De plus, la technique proposée est plus performante dans les scénarios à haute orientation, ce qui est une tâche très intéressante et stimulante qui vise à augmenter la densité de couverture des points.

4.2. Nouveauté sur les Méthodes de Détection des Défauts de la Route

Passant au sujet principal de la thèse, deux nouvelles méthodes de détection des défauts routiers sont proposées, appelées méthode de détection des défauts basée sur les fonctionnalités et méthode de détection des défauts basée sur la grille. La méthode de détection de défauts basée sur la fonction de concavité fournie par le filtre gaussien différentiel du second ordre. Ce filtre $h_{DGF2}(n)$ calcule la dérivée seconde du signal d'entrée et dont la sortie z_{DGF2} indique la caractéristique de concavité du signal d'entrée $z_w(n)$ telle qu'exprimée dans les équations 2 et 3. Tout d'abord, cette méthode fonctionne individuellement sur chaque laser d'élévation, pour détecter plusieurs défauts routiers de petite taille (nids de poule, bosses) avec des motifs homogènes et des propriétés. Cette méthode est très sensible à la fonction de concavité, mais elle nécessite une résolution LiDAR suffisante sur la cible.

$$\begin{aligned} z_{DGF2}(n) &= z_w(n) * h_{DGF2}(n) \\ &= z_w(n) * h_{DGF}(n) * h_{DGF}(n) \end{aligned} \tag{2}$$

$$\begin{aligned} h_{DGF}(n) =& \frac{G}{\sqrt{2\pi\sigma^2}} \exp\left(\frac{-(n-\mu)^2}{2\sigma^2}\right) \\ &- \frac{G}{\sqrt{2\pi\sigma^2}} \exp\left(\frac{-(n+\mu)^2}{2\sigma^2}\right) \text{ for } \begin{cases} -\mu \leq n \leq \mu \\ \sigma = \mu/2 \end{cases} \end{aligned} \tag{3}$$

où G est un paramètre de gain pour l'amplification du signal, σ est l'écart type de la distribution gaussienne et n est le numéro d'index des points des signaux z_w, z_{DGF}, z_{DGF2} et les réponses impulsionnelles du système h_{DGF}, h_{DGF2}.

D'autre part, la méthode de détection de défauts basée sur la grille comprend deux contributions :

- Méthode d'interpolation pondérée par l'inverse de la distance améliorée, basée sur la distribution en altitude dans une grille spatiale pour générer une image géoréférencée en altitude comme exprimé dans les équations 4,5,6,7 ,8 et 9.

$$d_{w/opt} = \frac{|A_{opt}x_w + B_{opt}y_w + C_{opt}z_w + D_{opt}|}{\sqrt{A_{opt}^2 + B_{opt}^2 + C_{opt}^2}} \tag{4}$$

$$d_{w/opt} = z_w + h \tag{5}$$

$$I_d = \frac{d_{w/opt} - d_{\min}}{d_{\max} - d_{\min}} \times L_{gray} \tag{6}$$

où x_w, y_w, z_w sont les coordonnées cartésiennes des points au sol recalibrés 3D, $A_{opt}, B_{opt}, C_{opt}, D_{opt}$ sont les paramètres du plan optimisé (P_{opt}), $d_{\min}$ et $d_{\max}$ sont respectivement les valeurs minimale et maximale de la distance en altitude $d_{w/opt}$, et $L_{gray} = 255$ est le niveau de gris d'intensité maximale.

La valeur de gris d'intensité de la cellule de la grille (i, j), notée G_{ij} , s'exprime comme suit :

$$G^{ij} = \left(\sum_{k=1}^{n_{ij}} W^{k,ij} I_d^{k,ij} \right) \Bigg/ \left(\sum_{k=1}^{n_{ij}} W^{k,ij} \right) \tag{7}$$

$$W^{k,ij} = aW_D^{k,ij} + bW_{I_d}^{k,ij} \tag{8}$$

$$a + b = 1 \tag{9}$$

où n_{ij} est le nombre de points dans la cellule (i, j), $W^{k,ij}$ et $I_d^{k,ij}$ sont le poids général et l'intensité de la distance en altitude du point k^{th} dans la cellule (i, j), respectivement. a et b sont les coefficients de poids, $W_D^{k,ij}$ et $W_{I_d}^{k,ij}$ sont les composantes de poids calculées en tenant compte de la distance euclidienne plane D à partir de la grille le centre de cellule et l'intensité de distance d'altitude I_d dans la cellule de grille (i, j), respectivement.

- Algorithme de Fractionnement de Grille , fournit une taille de grille dynamique pour augmenter la résolution de l'image géoréférencée, comme expliqué dans Algorithm 5.

Algorithm 5: Algorithme de Fractionnement de Grille

```
Input: Distance en altitude $d_{w/opt}$, valeurs initiales des longueurs
       horizontale et verticale $H, V$ respectivement, et coordonnées
       cartésiennes $x_w, y_w, z_w$ des points $k^{th}$ dans une cellule de grille
       $(i, j)$
Output: Image grise géoréférencée $G^{ij}$
1 Si la cellule de la grille est vide, associez la valeur de gris d'intensité $G^{ij}$ à
    zéro.
    Sinon, calculez la distribution de distance $\sigma_{d_{w/opt}}$ des points $k^{th}$ dans une
    cellule de grille $(i, j)$ comme indiqué ci-dessous :
    $\sigma_{d_{w/opt}} = \sqrt{\frac{1}{N} \sum_{k=1}^{n_{ij}} (d_{w/opt} - \overline{d_{w/opt}})^2}$
2 Si l'écart type de la distribution de distance $\sigma_{d_{w/opt}} \geq \sigma_{th}$, divisez la
    cellule de la grille en quatre sous-grilles au cas où toutes les sous-grilles
    ne seraient pas vides, en divisant les longueurs horizontale et verticale
    par deux $H/2, V/2$ respectivement. Où $\sigma_{th} \simeq 1.5cm$ est un seuil
    constant qui définit la précision de distance maximale pour l'impact
    laser du capteur LiDAR sur un plan plat. Ensuite, passez à l'étape 1.
    Sinon, calculez la valeur de niveau de gris $G^{ij}$ en utilisant la méthode
    d'interpolation pondérée par l'inverse de la distance proposée
    ci-dessus.
3 Divisez les cellules de la grille en cellules de sous-grille en fonction de la
    plus petite taille de cellule et associez les valeurs de niveau de gris des
    cellules de sous-grille à égalité avec la valeur de niveau de gris de la
    cellule de la grille d'origine.
```

Cette méthode fonctionne simultanément sur tous les lasers d'élévation. Elle est sensible à la distribution d'altitude et nécessite une résolution LiDAR élevée pour détecter, visualiser et localiser les défauts routiers multi-homogènes dans une image géoréférencée à haute résolution. Les résultats de l'évaluation montrent une performance compromise et une efficacité impressionnante de nos méthodes de détection de défauts proposées, en termes d'exactitude, de précision et de rappel par rapport à d'autres méthodes de détection de défauts, prouvant la capacité de détection des défauts de nids-de-poule et de bosses à l'aide de données réelles.

5. Conclusion et Perspectives

Dans le cadre des systèmes de transport et d'aide à la conduite, notre contribution concerne la détection multi-défauts à partir de mesures de télémétrie 3D laser distribuée. Nous avons développé et validé différentes méthodes, compatibles avec tous les capteurs LiDAR 3D cylindriques. Celles-ci ont été appliquées à un système de perception LiDAR 3D, monté et centré sur le véhicule, et orienté vers l'arrière. Par ailleurs, le capteur LiDAR est tourné vers le sol afin d'augmenter la résolution pour la caractérisation de la route, ce qui améliore le processus de détection de défauts de route. Par conséquent, le processus d'étalonnage a été adopté afin de transformer le référentiel LiDAR en un référentiel global, modifiant ainsi le référentiel LiDAR en une scène 3D interprétable.

Le développement et l'amélioration d'une nouvelle méthode d'étalonnage extrinsèque flexible LiDAR/sol LGCM a été le point de départ de cette thèse. La méthode d'étalonnage s'appuie sur une modélisation basée sur le plan du sol pour estimer les paramètres extrinsèques 4-DOF : hauteur et orientation 3D. De plus, le processus de calibrage repose sur quatre aspects principaux : estimateur des moindres carrés du modèle linéaire, formule de Rodrigues, algorithme conique des moindres carrés et algorithme d'optimisation de Levenberg-Marquardt. Les résultats montrent une performance significative en termes de précision et de robustesse vis-à-vis de la variation de l'orientation et de la précision de distance du LiDAR respectivement, prouvant la stabilité et la précision de la méthode d'étalonnage proposée sur des données synthétiques et réelles. Cela reflète la bonne capacité globale de cette méthode d'étalonnage lorsqu'elle est appliquée sur des capteurs LiDAR cylindriques dans des conditions expérimentales difficiles.

De plus, nous avons proposé et développé deux nouvelles méthodes de détection de défauts routiers dans le cadre de cette thèse, où la solution de ces deux méthodes de détection repose sur la méthode d'étalonnage, qui fournit une vue horizontale et exploitable du sol. Tout d'abord, la méthode de détection de défauts basée sur les fonctionnalités FBDDM, qui étudie la caractéristique de concavité sur chaque laser d'élévation à l'aide d'un filtre gaussien différentiel de second ordre, pour détecter plusieurs défauts de route homogènes. Le processus de recalibrage s'est imposé pour améliorer la fausse alarme, afin d'améliorer les résultats d'évaluation de la méthode de détection des défauts basée sur les fonctionnalités. Deuxièmement, la méthode de détection de défauts basée sur la grille GBDDM qui repose sur deux aspects principaux : la méthode d'interpolation pondérée par la distance inverse améliorée et l'algorithme de fractionnement de grille, pour détecter, visualiser et localiser les défauts routiers multi-homogènes dans une image géoréférencée à haute résolution. L'évaluation de ces méthodes montrent l'efficacité de nos méthodes de détection de défauts, en termes d'exactitude, de précision par rapport à d'autres méthodes de détection de défauts, prouvant la capacité de notre méthode à fournir une solution efficace de détection de défauts tels que les nids-de-poule et les bosses sur données réelles.

Sur la base des résultats présentés dans cette thèse, nous mettons en évidence plusieurs directions de recherche futures intéressantes :

- Dans notre travail, les méthodes de détection sont appliquées sur les défauts de route (nids de poule et bosses). il serait intéressant d'exploiter ce type de méthodes sur la détection de véhicules, d'obstacles ou de piétons. Au delà, on pourrait s'intérsser à adapter notre méthode de détection de défauts basée sur une approche par grille pour détecter les risques liés à la présence d'eau sur la route, à l'aide de la réflectivité LiDAR.

- L'utilisation d'un LiDAR haute résolution comme le capteur LiDAR OS1-128 augmentera les performances des processus de calibrage et de détection. Mais l'enjeu sera également lié à la taille des défauts pour la problématique de détection.

- Dans le processus de détection des points de route, nous perdons une petite région spatiale en périphérie de la route. Ainsi, nous proposons de développer une méthode de détection de route pour étudier les défauts qui sont situés le long des bords de route.

- Nous proposons de travailler sur les problématiques de fusion LiDAR/caméra pour augmenter les performances des méthodes de détection proposées, en particulier la méthode de détection de défauts basée sur l'approche par grille.

- En outre, la fusion du LiDAR, avec un système de positionnement global de type GPS et une centrale inertielle (IMU) permettra de prendre en charge le suivi, la localisation et la cartographie des défauts dans une système de référence mondial.

- De plus, les méthodes de calibrage et de détection proposées sont compatibles avec les LiDAR cylindriques. Il sera intéressant d'étudier l'évolution des méthodes proposées pour assurer la compatibilité avec les LiDAR non cylindriques comme le capteur LiDAR Velodyne HDL-64. Ainsi, les méthodes peuvent être directement appliquées sur le jeu de données KITTI-ROAD pour se comparer parfaitement avec d'autres méthodes.

- Enfin, le défi le plus intéressant est d'implémenter les méthodes sur un processeur de signal numérique DSP en tant qu'application temps réel.

6. Structure du manuscrit

Plus loin, ce manuscrit de thèse introduit les chapitres suivants :

- **Chapitre** 2 présente l'état de l'art de la thèse, qui comprend l'étude de la différence entre les capteurs 2D et 3D, la définition du LiDAR 3D, la comparaison entre le LiDAR 3D et d'autres capteurs 3D, la définition du calibrage du LiDAR et les travaux de la communauté liés à cette problématique. En outre, il présente également une revue des méthodes de détection de défauts de route basées sur les capteurs LiDAR, Caméra et Accéléromètre.

- **Chapitre** 3 présente les caractéristiques du capteur LiDAR Velodyne VLP-16, les opérations d'extraction et de prétraitement des données.

- **Chapitre** 4 présente la modélisation géométrique des impacts laser du capteur LiDAR sur le sol, et la méthode de calibrage extrinsèque LiDAR/sol proposée. En outre, il montre des résultats expérimentaux de calibrage extrinsèque en simulation et sur des données réelles.

- **Chapitre** 5 présente le processus de sélection au sol, la méthode de détection des défauts basée sur les fonctionnalités proposée et la méthode de détection des défauts basée sur une approche par grille. En outre, il montre les résultats d'évaluation sur données réelles des méthodes de détection de défauts routiers proposées en comparaison avec d'autres méthodes.

Thesis Extended Summary

1. Context

The state of road network knowledge in a country is an important issue in order to be able to deploy a rational policy of road maintenance, rehabilitation and traffic improvement. As we know, some traffic accidents are the result of the presence of disabilities or small obstacles on the roads, and one of the major problems that the population suffers from on a daily lives. Although, road traffic injuries represents a major global health problem of human safety. As a key facts, the World Health Organization (WHO) report on the Global status of road traffic safety, reflecting information from worldwide countries, indicates that the total number of road traffic deaths has plateaued at 1.15 million person in 2000. Then it increases 0.1 million to reach 1.25 million road traffic deaths in 2015 [1], [2], and 1.35 million deaths in 2018 [3]. Especially in low-middle-income countries as Africa and South-East Asia, record 95% of the world's fatalities occur on the road [4], and more than half road traffic deaths are among vulnerable road users: motorcyclists, cyclists, and pedestrians, where most of deaths and disabilities are for individuals aged 5-29 years [5]–[7]. In addition, the estimation of road traffic injuries consumption reach 3% of the gross national products of world governments, which have a serious impact on national economies [3], [4]. Therefore, the United Nations (UN) road safety collaboration has developed a global plan that proposes an 2030 agenda for sustainable development to set an ambitious target of halving the global number of deaths and injuries from road traffic crashes by 2020 [8], [9].

This thesis topic falls within this framework since it proposes to provide a geometrical and topological model of the route and to extract semantic information about the roads. In addition, these works will focus on the characterization of road surface and the presence of potentially dangerous areas, first, through a **calibration of the geometrical environment information**, followed by **detection and localization of the road defects**. It will also be important to visualize and locate the geometrical information of each defect obtained on the road.

This work is a part of the general framework of multi-sensor perception systems, more particularly focusing on the above different characteristics, that will be obtained from a telemetric information of a multi-lasers rangefinder

(Light Detection and Ranging LiDAR, Laser Range Finder LRF) mounted on a vehicle as shown in Figure 1.

(a) VLP-16 LiDAR mounted on a vehicle (b) VLP-16 LiDAR mounted on a fixed stand

FIGURE 1: VLP-16 system

In transport applications, the development of Advanced Driver Assistance Systems (ADAS) has been the subject of much work for the past twenty years [10]. In transportation systems context, the objective is to monitor the vehicle environment in order to inform the driver, at each moment, about the potentially hazardous situations. Multi-object detection methods in data from a scanning laser rangefinder on board a moving vehicle have been proposed. Even though, these methods retain some limitations inherent in the physical nature of the measurement signal, this laser sensor has many advantages for ADAS: day/night vision, low accuracy, high frequency of measurement, directive laser shots, wide field of perception. The major drawback of a single-layer laser rangefinder is its sensitivity to pitching movements, linked to its directivity: the distances measured can be disturbed and give rise to undesirable measurements of the scene, designated by the more general term of " clutter ". The development of multi-layer rangefinders, that is to say working on several measurement planes, has made it possible to minimize these disturbances inherent in the physical nature of the measurement. Although, having the particularity of delivering precise relative positioning information unlike sensors of the video camera type, laser rangefinders are distinguished by the relative poverty of the information received on the scene (directly linked to the angular resolution of the sensor).

Therefore, it is necessary to develop solutions informing the driver by a prior information about the road defects. This information is important to obtain a statistical road defects data in order to avoid the risky accidents and to take a right decision for road enhancement in a spatial road network. Our hypothesis precisely works on an extrinsic calibration method for the LiDAR sensor based on the geometrical plane model estimation, which serves the two methods of road defects detection: feature-based and grid-based.

2. Thesis Aims and Objectives

In transportation applications, many articles use LiDAR to detect and track objects of interest (pedestrians, vehicles, etc...) from 3D measurements. The LiDAR sensor is also used to detect the road, often in addition to camera sensors. In these applications, the idea is to have a thorough view of the driver's environment over the widest possible horizon. Therefore, the aim of this thesis involves a LiDAR sensor with a low angle of inclination (horizontally oriented sensor) to study and analyze the road defects: holes, humps or any homogeneous out-layers. Which contribute in solving the car accidents problem that are caused by spatial dangerous areas in the road network. This study includes several scientific objectives: road defects' detection, visualization and localization.

3. Thesis Key Points

The key points of the thesis problem are shown in Figure 2, and are listed below:

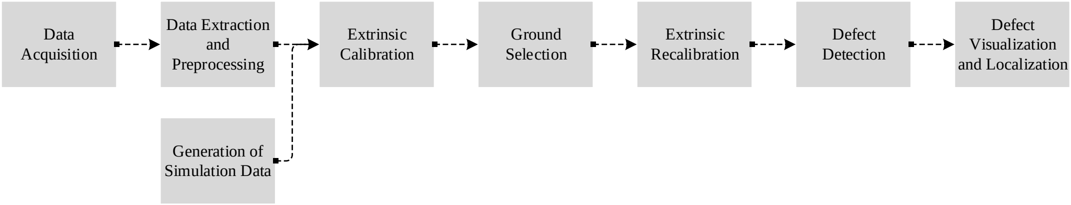

FIGURE 2: Thesis Block Diagram

1. Generation of simulation data on LiDAR sensor data for different orientations and altitudes.
2. Optimization of the LiDAR altitude and orientation using the synthetic data, before analyzing the coverage of LiDAR distribution points over the ground, to be suitable for the practical application and to ensure the possibility of road defect detection.
3. Data acquisition using LiDAR sensor mounted on a moving vehicle.
4. Data extraction (Range, Azimuth, Elevation, Reflectivity, and Time) from the .pcap format file. Then data preprocessing and PointCloud player presentation.
5. 3D Extrinsic LiDAR/Ground calibration method using 3D geometrical plane-based estimation.
6. Ground selection PointCloud method using differential Gaussian filter, to eliminate: the obstacles that exist on the road, and the objects that surround the road.
7. Extrinsic re-calibration for the road PointCloud to enhance the calibration process.
8. Defect Detection feature-based method.
9. Defect visualization and localization using grid-based method.

4. Proposed Contributions

In the context of this study (road defects detection), the LiDAR sensor is rotated toward the ground in order to increase the points' density covering the defects by the multi elevation laser as shown in Figure 3. This causes a complicated modification in the ground 3D view scene with respect to the LiDAR frame. Therefore, extrinsic calibration was adopted in order to transform the LiDAR frame into a global reference frame, thus modifying the ground impact points transformation into an understandable view scene.

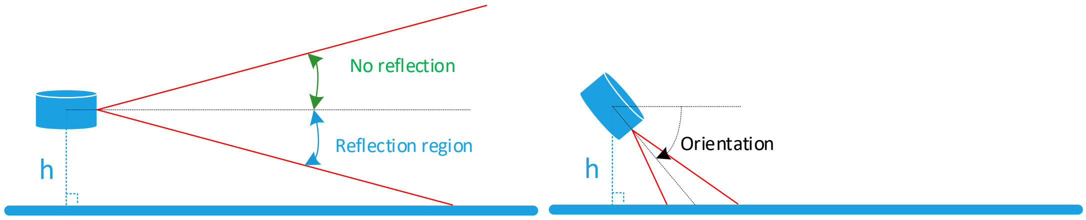

(a) No orientation (b) LiDAR orientation

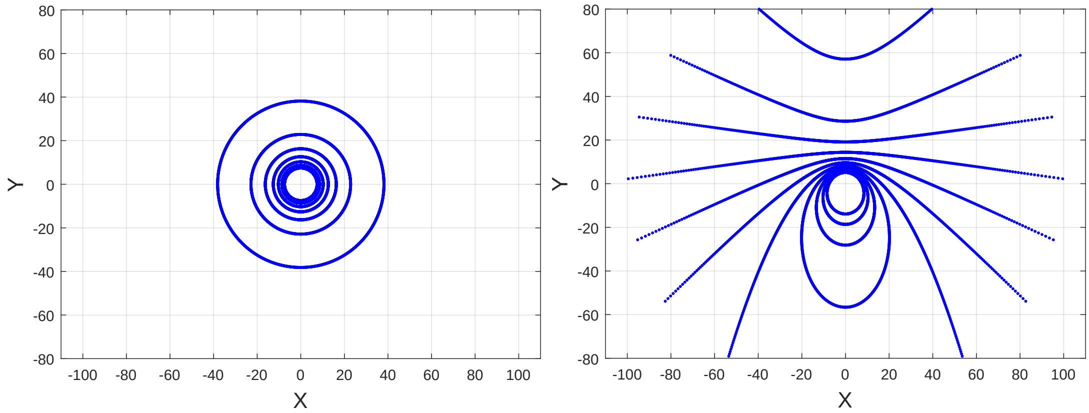

(c) No rotation $\phi_x = 0°$ (d) $\phi_x < \frac{1}{2}vFOV$

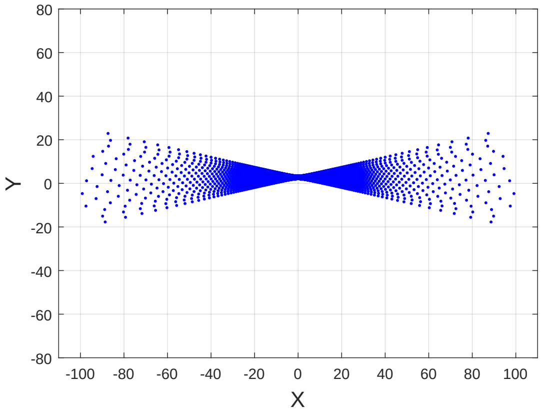

(e) $\phi_x > \frac{1}{2}vFOV$

FIGURE 3: Large sparsity area vs high density points

4.1. Calibration Method Novelty

The perspective of our framework is to propose a calibration method (and road plane estimation) that works under difficult experimental conditions (high angle of inclination). Indeed, we aim at developing a calibration method that allows to determine precisely the road plane in a very close vicinity of the vehicle. The idea in the long term is to detect road defects when driving on the road network. Although developed with this in mind (i.e. with a high degree of accuracy in determining the road plane), our method is general enough to be applicable in any wider operational context.

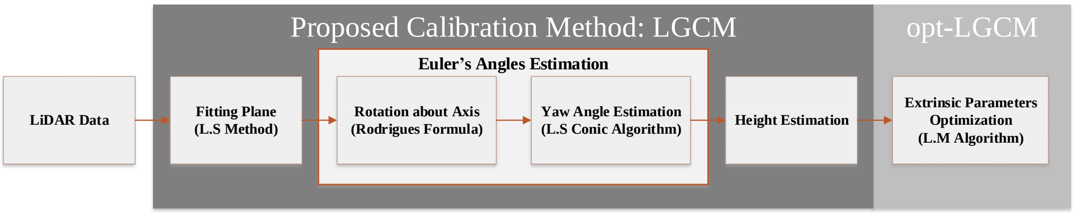

FIGURE 4: The proposed extrinsic calibration method block diagram

In order to attain the above key objective, this thesis addresses a new flexible extrinsic calibration method, published in [11], [12]. The proposed calibration method can be summarized by the following two-fold contributions: (1) ground plane model estimation and (2) rotation transformation matrix estimation from world ground reference to LiDAR sensor frame as shown in Figure 4. The 3D Euler's angles (sensor orientation) and the height (sensor altitude above the ground) are two essential extrinsic parameters required to calibrate the full 3D LiDAR sensors as shown in Figure 5, in order to improve the capability of road defect detection as will be explained in section 4.2.1. In addition, the problem is modeled by 4-DOF (degree of freedom) transformation: 3-DOF rotation and 1-DOF height, instead of 6-DOF transformation: 3-DOF rotation and 3-DOF translation. This modeling advantage provides the simplicity in the optimization process of the extrinsic parameters.

As compared to a previous plane-based methods [13], [14], the developed approach can be generalized to all types of scanning laser rangefinders and presents an optimized estimation of all extrinsic calibration parameters (angles, height). This global method can be implemented on different cylindrical LiDAR sensors (low-cost 3D and full 3D) with various range accuracy.

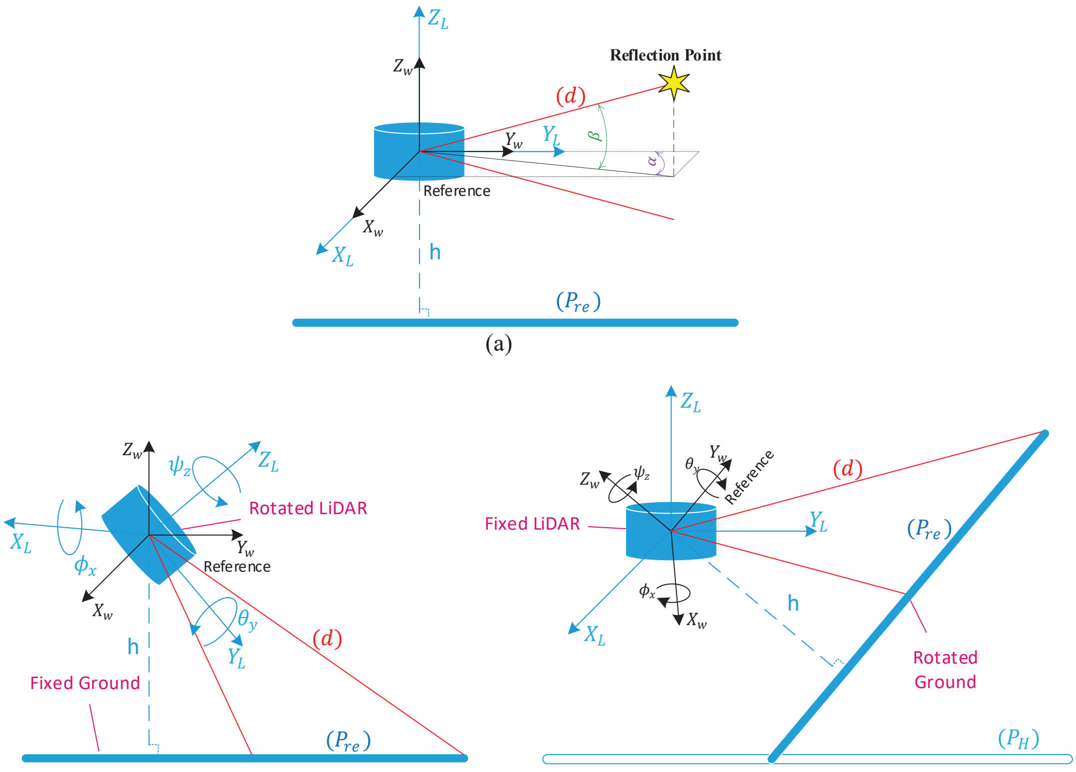

(a)

(b)

(c)

FIGURE 5: (a) No orientation, (b) Practical orientation concept, (c) Scientific orientation concept

In addition, the proposed technique outperforms in high orientation scenarios, which is a very interesting and challenging task that aims to increase the points' density coverage.

4.2. Road Defect Detection Methods Novelty

Moving to main thesis subject, two novel road defect detection methods are proposed, called Feature-Based Defect Detection Method and Grid-Based Defect Detection Method. The Feature-Based Defect Detection Method, based on the concavity feature delivered by second order of Differential Gaussian Filter. For this, the second order of differential Gaussian filter $h_{DGF2}(n)$ represents the second derivative of an input signal, which indicates the concavity feature in the output signal z_{DGF2} of the input signal $z_w(n)$ as expressed in Equations 10 and 11. First, this method works on each single elevation laser individually, to detect multi road defects (pothole,hump) with homogeneous patterns and small sizes properties. This method is very sensitive to concavity feature, but it requires enough LiDAR coverage resolution on the target.

$$\begin{aligned} z_{DGF2}(n) &= z_w(n) * h_{DGF2}(n) \\ &= z_w(n) * h_{DGF}(n) * h_{DGF}(n) \end{aligned} \tag{10}$$

$$\begin{aligned} h_{DGF}(n) =& \frac{G}{\sqrt{2\pi\sigma^2}} \exp\left(\frac{-(n-\mu)^2}{2\sigma^2}\right) \\ & - \frac{G}{\sqrt{2\pi\sigma^2}} \exp\left(\frac{-(n+\mu)^2}{2\sigma^2}\right) \text{ for } \begin{cases} -\mu \le n \le \mu \\ \sigma = \mu/2 \end{cases} \end{aligned} \tag{11}$$

Where G is a gain parameter for signal amplification, σ is the standard deviation of the Gaussian distribution, and n is the points' index number of the signals z_w, z_{DGF}, z_{DGF2} and the system impulse responses h_{DGF}, h_{DGF2}.

On the other hand, the Grid-Based Defect Detection Method includes twofold contributions:

- Improved Inverse Distance Weighted interpolation method, based on the altitude distribution in a spatial grid to generate altitude georeferenced image as expressed in Equations 12,13,14,15,16 and 17.

$$d_{w/opt} = \frac{|A_{opt}x_w + B_{opt}y_w + C_{opt}z_w + D_{opt}|}{\sqrt{A_{opt}^2 + B_{opt}^2 + C_{opt}^2}} \tag{12}$$

$$d_{w/opt} = z_w + h \tag{13}$$

$$I_d = \frac{d_{w/opt} - d_{\min}}{d_{\max} - d_{\min}} \times L_{gray} \tag{14}$$

Where x_w, y_w, z_w are the Cartesian coordinates of the 3D recalibrated ground points, $A_{opt}, B_{opt}, C_{opt}, D_{opt}$ are the parameters of the optimized plane (P_{opt}), $d_{\min}$ and $d_{\max}$ are the minimum and maximum values of the altitude distance $d_{w/opt}$ respectively, and $L_{gray} = 255$ is the maximum intensity gray level.

The intensity gray value of the grid cell (i, j), which is denoted by G_{ij} , is expressed as follows:

$$G^{ij} = \left(\sum_{k=1}^{n_{ij}} W^{k,ij} I_d^{k,ij} \right) \Bigg/ \left(\sum_{k=1}^{n_{ij}} W^{k,ij} \right) \tag{15}$$

$$W^{k,ij} = aW_D^{k,ij} + bW_{I_d}^{k,ij} \tag{16}$$

$$a + b = 1 \tag{17}$$

Where n_{ij} is the number of data points within grid cell (i, j), $W^{k,ij}$ and $I_d^{k,ij}$ are the general weight and the altitude distance intensity of the k^{th} point within grid cell (i, j), respectively. a and b are the weight coefficients, $W_D^{k,ij}$ and $W_{I_d}^{k,ij}$ are the weight components calculated considering the planar Euclidean distance D from the grid cell center and the altitude distance intensity I_d within grid cell (i, j), respectively.

- Grid Splitting Algorithm, provides dynamic grid size to increase the georeferenced image resolution as explained in Algorithm 6.

```
Algorithm 6: Grid Splitting Algorithm
Input: Altitude distance $d_{w/opt}$, initial horizontal and vertical lengths
       values $H, V$ respectively, and the Cartesian coordinates $x_w, y_w, z_w$
       of the $k^{th}$ points within a grid cell $(i, j)$
Output: Georeferenced gray image $G^{ij}$
1 If the grid cell is empty, associate the intensity gray value $G^{ij}$ to zero.
  Else, compute the distance distribution $\sigma_{d_{w/opt}}$ of the $k^{th}$ points within a
  grid cell $(i, j)$ as expressed below:
  $\sigma_{d_{w/opt}} = \sqrt{\frac{1}{N} \sum_{k=1}^{n_{ij}} (d_{w/opt} - \overline{d_{w/opt}})^2}$
2 If the standard deviation of the distance distribution $\sigma_{d_{w/opt}} \geq \sigma_{th}$, split
  the grid cell into four sub-grids in case if all of the sub-grids are not
  empty, by dividing the horizontal and vertical lengths by two $H/2, V/2$
  respectively. Where $\sigma_{th} \simeq 1.5cm$ is a constant threshold that defines the
  maximum distance accuracy for the lasers impact of the LiDAR sensor
  on a flat plane. Then, go to step 1.
  Else, compute the intensity gray value $G^{ij}$ using the above proposed
  inverse distance weighted interpolation method.
3 Split the grid cells into sub-grid cells according to the smallest grid cell
  size, and associate the intensity gray values of the sub-grid cells equal
  to the original grid cell's intensity gray value.
```

This method works simultaneously on all elevation lasers, it is sensitive to altitude distribution feature, and it requires high LiDAR coverage resolution to detect, visualize and localize the multi homogeneous road defects in a high resolution georeferenced image. The evaluation results show a compromised performance and impressive efficiency of our proposed defect detection methods, in terms of accuracy, precision and recall against other defect detection methods, proving the detection ability of potholes and humps defects using real data.

5. Conclusion and Perspectives

As a part of transportation and driver assistance systems framework, our contribution concerns multi-defect detection from distributed 3D telemetry measurements. We have developed and validated various global methods, that are compatible with any cylindrical 3D LiDAR sensors. These have been applied to of 3D LiDAR perception system mounted and centered on the vehicle backward. Indeed, the LiDAR sensor is rotated toward the ground in order to increase the road coverage resolution, which improves the road defect detection process. Therefore, the calibration process was adopted in order to transform the LiDAR frame into a global reference frame, thus modifying the LiDAR frame into an understandable view scene.

The development and improvement of a novel flexible extrinsic LiDAR/Ground Calibration Method LGCM was the starting point of this thesis. The calibration method is relied on ground plane-based modeling, to estimate the 4-DOF extrinsic parameters: height and 3D orientation. Moreover, the calibration process is built on four main aspects: linear model Least Squares estimator, Rodrigues formula, Least Squares Conic Algorithm and Levenberg-Marquardt optimization algorithm. The results show a significant performance in terms of precision and robustness against the variation of LiDAR's orientation and range accuracy respectively, proving the stability and the accuracy of the proposed calibration method on synthetic and real data. This reflects the global good capability of this calibration method when applied on cylindrical LiDAR sensors under difficult experimental conditions.

In addition, we proposed and developed two novel road defect detection methods in the context of this thesis, where the solution of these two detection method relies on the calibration method, that provides a horizontal and understandable ground view. First, the Feature-Based Defect Detection Method FBDDM, that studies the concavity feature on each elevation laser using second order Differential Gaussian Filter, to detect multi homogeneous road defects. The recalibration process has imposed itself to enhance the false alarm, in order to improve the evaluation results of the Feature-Based Defect

Detection Method. Second, the Grid-Based Defect Detection Method GB-DDM that relies on two main aspects: improved Inverse Distance Weighted interpolation method and Grid Splitting Algorithm, to detect, visualize and localize the multi homogeneous road defects in a high resolution georeferenced image. The evaluation results show a compromised performance and impressive efficiency of our proposed defect detection methods, in terms of accuracy, precision and recall against other defect detection methods, proving the detection ability of potholes and humps defects using real data.

Based on the outcomes presented in this thesis, we highlight several interesting future research directions:

- In our work, the detection methods is applied on road defects (potholes and humps). It will be an interesting application to apply the same methods on vehicles, obstacles and pedestrians detection. More than that, modify the grid-based defect detection method to detect the water hazards using the reflectivity LiDAR feature.
- Using a high resolution LiDAR like OS1-128 LiDAR sensor will increase the performance of calibration and detection processes. But, it will also increase the chance of defect size estimation challenge.
- In road selection points process, the road looses a small spatial regions at the edge of the road. So, we suggest to develop a road detection method to study the defects that are aligned beside the road edges.
- We recommend a LiDAR and Camera fusion sensors to increase the performance of the proposed detection methods, especially the grid-based defect detection method.
- In addition, the fusion of LiDAR, Global Positioning System GPS and Inertial Measurement Unit IMU will support a defect tracking, localization and mapping system in a global world wide reference.
- Moreover, the proposed calibration and detection methods are compatible with cylindrical LiDARs. It will be interesting to find a way to modify the methods process to be compatible with non cylindrical LiDARs like Velodyne HDL-64 LiDAR sensor. So, the methods can be directly applied on the KITTI-ROAD data-set to compare perfectly with other methods.
- Finally, the most interesting challenge is to implement the methods on a Digital Signal Processor DSP as a real-time application.

6. Report Structure

Later, this report introduces the following chapters:

- **Chapter** 2 presents the state of the art of the thesis, which includes the difference between 2D and 3D sensors, 3D LiDAR definition, comparison between 3D LiDAR with other 3D sensors, LiDAR calibration definition and LiDAR calibration related work. In addition, it presents also the literature review of road defect detection methods based on LiDAR, Camera and Accelerometer sensors.
- **Chapter** 3 presents the characteristics of Velodyne VLP-16 LiDAR sensor features, the data extraction and preprocessing operations.
- **Chapter** 4 presents the geometrical impact modeling of the LiDAR sensor on the ground, and the proposed extrinsic LiDAR/Ground Calibration Method. In addition, it shows the extrinsic calibration experimental results using simulation and real data.
- **Chapter** 5 presents the ground selection process, the proposed Feature-Based Defect Detection Method and Grid-Based Defect Detection Method. In addition, it shows the evaluation results of the proposed road defect detection methods, compared against other methods using real data.